THE UNIVERSITY
of ADELAIDE

School of Physical Sciences
Department of Physics

A Study of the $\Lambda(1405)$ in Lattice QCD

Benjamin J. Menadue

Supervisors
Prof. Derek Leinweber
Dr. Waseem Kamleh

November 2018

Table of Contents

Abstract

The lowest-lying odd-parity state of the Λ baryon lies surprisingly low in mass. Even though it contains a heavier valence strange quark and has odd parity, with an energy of 1405 MeV it lies lower than any other excited spin-1/2 baryon. In the almost 50 years since its discovery there has been significant effort expended to describe the structure of the $\Lambda(1405)$, however there has been no convincing resolution. It is very difficult to reconcile this low mass with the quark model interpretation for this state, and lattice QCD studies have consistently failed to reproduce it.

In this work, we use the PACS-CS $(2+1)$-flavour full-QCD ensembles together with a variational analysis using source and sink smearing in an attempt to isolate this otherwise-elusive state using lattice QCD. For the first time, we report masses for the lowest-lying states consistent with those in nature – including the $\Lambda(1405)$. We then build on this result by investigating their electromagnetic properties, and show that the strange quark contribution to the magnetic form factor for the $\Lambda(1405)$ near-vanishes in the physical limit.

Together with a Hamiltonian effective field theory model analysis of the lattice QCD energy levels, this strongly suggests that the structure of the $\Lambda(1405)$ is dominated by a molecule-like, bound antikaon-nucleon component. That is, we report evidence for the existence of molecular meson-baryon bound states in QCD.

Statement of Originality

I certify that this work contains no material which has been accepted for the award of any other degree or diploma in my name, in any university or other tertiary institution and, to the best of my knowledge and belief, contains no material previously published or written by another person, except where due reference has been made in the text. In addition, I certify that no part of this work will, in the future, be used in a submission in my name, for any other degree or diploma in any university or other tertiary institution without the prior approval of the University of Adelaide and where applicable, any partner institution responsible for the joint-award of this degree.

I give permission for the digital version of my thesis to be made available on the web, via the University's digital research repository, the Library Search and also through web search engines, unless permission has been granted by the University to restrict access for a period of time.

I acknowledge the support I have received for my research through the provision of an Australian Government Research Training Program Scholarship.

Benjamin J. Menadue

Acknowledgements

"It's done!" That was the subject line of perhaps the most satisfying e-mail I've ever sent, with my completed thesis draft attached. It's been an amazing—and long—journey, and wouldn't have been possible without the help of many of my colleagues, friends, and family. To list everyone would likely be longer than this body of this thesis, so instead I'll just mention a few. To the rest, know that you have my gratitude, and that I couldn't have done it without you!

Firstly, I must acknowledge my supervisors, Derek Leinweber and Waseem Kamleh. Over the years, you've always been there for discussions—physics related or otherwise—when needed. Without your direction and suggestions, it's unlikely this research would have got off the ground, much less have produced the remarkable results it has.

Next, I must give a special thanks to my office mates from when I was in Adelaide: Adrian Kiratidis, Dale Roberts, Phiala Shanahan, Daniel Trewartha, and in particular Ben Owen. I imagine putting up with me talking to myself when writing a particularly difficult section or code, or using all the whiteboards in the room to solve a stubborn equation would have been trying at times.

Similarly, thanks to my friends and colleagues at NCI: Andrey Bliznyuk, Roger Edberg, Leaf Lin, Dale Roberts (yes, the same one as above), Andrew Wellington, Yuanyuan Zhang, and especially Muhammad Atif and Allan Williams – not only for your continuous probes into the status of my thesis, but for also giving me the time to complete it amongst our already-overfull daily schedules.

To my close friends Justin and Jenni Nash, thank you for not only the encouragement over the years, and reminding me that I still needed to complete my thesis (especially once Justin had submitted his thesis – congratulations, again, by the way), but also the dinner and/or board games evenings that provide a nice break from routine and keep me sane!

To my family, and particularly Mum and Dad: thank you for your encouragement and support, both personally and financially, over the years.

Finally, to Silvie. You've always stood beside me – even when I've been ignoring you with my head buried in my laptop, working. I look forward to our wedding in August—next month!—and to the many years still ahead of us.

✣ One ✣
An Introduction

Originally predicted in 1959 by Dahlitz and Yuan [1, 2] from an analysis of the unitarity condition relating the $\pi\Sigma$ and $\overline{\mathrm{K}}\mathrm{N}$ amplitudes, the $\Lambda(1405)$ resonance presents as a negative-parity baryon resonance with spin $J = 1/2$, isospin $I = 0$, and strangeness $S = -1$. Sitting just below the $\overline{\mathrm{K}}\mathrm{N}$ threshold, experimental evidence of this resonance was reported from 1960 [3–5]. The latest Particle Data Group report [6] lists the $\Lambda(1405)$ as a four-star resonance with a mass of $1405.1^{+1.3}_{-1.0}$ MeV/c^2 and a width of 50.5 ± 2.0 MeV/c^2.

The introduction of the quark model revolutionised the field of particle physics, where the $\Lambda(1405)$ was interpreted as a three-quark state consisting of an up, a down, and a strange quark [7–9]. However, it is very difficult to reconcile such a state with the unexpectedly low mass that is observed experimentally. Since strange quarks are heavier than both up and down quarks, a naïve constituent quark model would naturally place the $\Lambda(1405)$ above its strangeness-0 nucleon counterpart, the $\mathrm{N}(1535)$ – completely counter to experimental results, where the $\mathrm{N}(1535)$ lies over 100 MeV/c^2 *above* the $\Lambda(1405)$! Moreover, the splitting between the $J^P = 1/2^-$ $\Lambda(1405)$ and its spin-orbit partner, the $J^P = 3/2^-$ $\Lambda(1520)$, is substantially larger than the equivalent splitting in the nucleon sector.

Alternatively, one can describe the $\Lambda(1405)$ resonance as a molecule-like state of an antikaon bound to a nucleon. This interpretation has been explored through various theoretical and phenomenological formalisms, including reaction matrix analysis [1, 2], vector meson exchange [10], the SU(3) cloudy bag model [11, 12], and chiral dynamics [13, 14]. Many of these studies find that the $\Lambda(1405)$ resonance overlaps with both the three-quark and molecular bound-state pictures, and indeed one would expect all possibilities with the correct quantum numbers to contribute to some degree in nature. The question then becomes – which of these provides the dominant contribution?

With this in mind, in this manuscript we investigate the $\Lambda(1405)$ using lattice quantum chromodynamics (lattice QCD), a non-perturbative, first-principles method for probing the strong interaction. While previous lattice QCD studies of the $\Lambda(1405)$ have failed to conclusively identify and describe this unusual state [15–17], here we extend the variational analysis techniques developed by the CSSM Lattice collaboration. Since these techniques proved successful in identifying the low-lying, odd-parity nucleon resonances $\mathrm{N}^*(1535)$ and $\mathrm{N}^*(1650)$ [18], it is only natural to consider their extension to resolving

the structure of the $\Lambda(1405)$ resonance.

In Chapter 2, we provide some historical notes surrounding this field of particle physics along with an introduction to quantum chromodynamics, the theory describing the strong interaction. In Chapters 3 and 4, we provide the necessary formalism addressing the lattice QCD methods needed for this investigation, and then in Chapters 5 and 6 we present our calculations, their results, and an analysis. Finally, in Chapter 7 we summarise our conclusions from this study – that of evidence for the existence of molecular meson-baryon bound states in QCD.

✣ Two ✣

Ἄτομος: A Brief History of Particle Physics

Ἄτομον. Derived from *ἄτομος*, meaning "indivisible", this was the name given to the fundamental units of matter by the ancient Greek philosophers. The concept of atomism, that all matter is composed of fundamental, indivisible particles, has existed for over two thousand years. References to this concept date as far back as the times of ancient India (with the Jain, Ājīvika, and Cārvāka philosophical schools) and ancient Greece (with the work of Leucippus and Democritus), and although these ideas were mostly philosophical or religious rather than empirical, modern science has retained the ancient Greek name for these particles: atoms.

Of course, we now know that the atoms are not indivisible – instead, they are composed of a nucleus and electrons. Moreover, the nucleus is itself composed of smaller protons and neutrons, and these are composed of even smaller quarks. Particle physics is the study of these objects, and how they interact to form matter as we observe it.

2.1 History

The stoichiometric work of John Dalton in the late 18th and early 19th centuries led him to conclude that each element was composed of a single, unique type of particle. Believing these to be the fundamental units of matter, he named them atoms, but by the end of the 19th century J. J. Thompson had discovered the electron, overturning this belief by concluding that they were a component of every atom. Rutherford's discovery of the atomic nucleus in 1909 further demonstrated the composite nature of the atom.

Rutherford and his students went on to show that the positive charge associated with any nucleus was always an integer multiple of the hydrogen nucleus. Together with the knowledge that the atomic masses of many elements were also approximately integer multiples of the hydrogen mass, this led him to propose that the hydrogen nucleus was a fundamental particle, of which all other atomic nuclei were composed; he named these particles "protons".

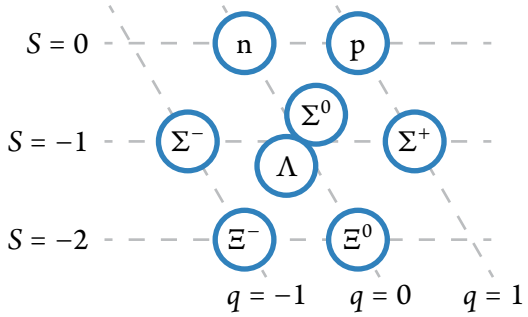

Figure 2.1: The baryon octet. Particles lying on the same horizontal line have the same strangeness quantum number, while those on the same diagonal have the same electric charge. If we were to draw vertical lines, then particles sharing these would have the same third isospin quantum number.

In 1932, James Chadwick discovered the neutron [19], originally predicted by Rutherford to explain the disparity between the atomic number of an atom and its atomic mass. In 1947, the pion and kaon were found, the first of the mesons to be discovered, and in 1950 the Λ baryon was discovered by Hopper and Biswas of the University of Melbourne [20]. Both the Λ and the kaon were found to have lifetimes orders of magnitude longer than expected, and so this was explained by a new quantum number, "strangeness", conserved by strong interactions but not weak.

By the late 1960s, an enormous number of these particles had been discovered, all believed to be elementary particles. This situation was dubbed the "particle zoo" – surely, not all of these hundreds of particles could be elementary? Significant effort was dedicated to classifying these particles, and in 1961 both Murray Gell-Mann [21, 22] and Yuval Ne'eman [23] independently proposed the so-called "Eightfold Way". This classification scheme works by arranging the particles based on their isospin and strangeness quantum numbers; we then recognise the resulting spin-1/2 baryon "octet" (shown in Figure 2.1) as the adjoint representation of $\mathrm{SU}(3)$, the Lie group of 3×3 unitary matrices with unit determinant.

The same principles could also be applied to the spin-3/2 baryons, organising them into a decuplet (as in Figure 2.2) but in order for this to make sense it required a then-undiscovered particle [24–26]. The model, however, did make predictions for this particle, and such a particle—the Ω^-—was found in 1964 [27].

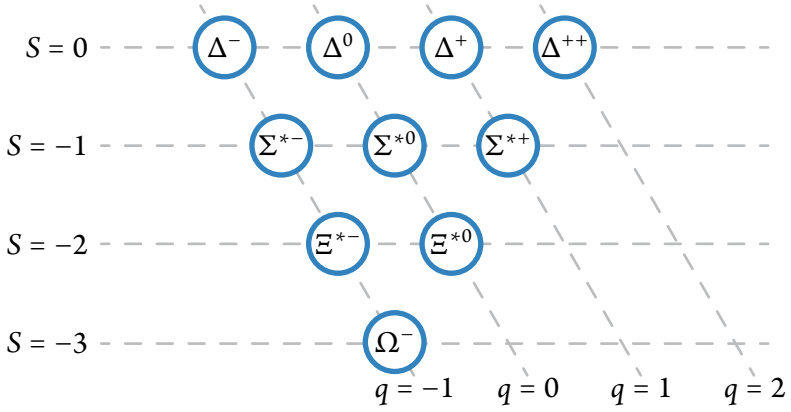

Figure 2.2: The baryon decuplet. Particles are arranged in the same fashion as in Figure 2.1.

2.2 The Quark Model

Shortly after the postulation of the Eightfold Way, both Gell-Mann [28] and George Zweig [29] independently posited a new model to explain its success: the quark model. In it, the known baryons and mesons are not the elementary particles as previously thought, but instead are composed of combinations of more-fundamental quarks and antiquarks. There are three flavours of quarks, up (u), down (d), and strange (s), and these form a triplet that belongs to the fundamental representation $\mathbf{3}$ of $\mathrm{SU}(3)$. The corresponding antiquark triplet then naturally belongs to the conjugate representation $\overline{\mathbf{3}}$.

If we give the quarks a baryon number of $1/3$, then we can consider the baryons as being constructed from three quarks, while the mesons from a quark and an antiquark. Moreover, such a construction naturally reproduces the multiplet structures seen in the hadronic spectra. The pseudoscalar (Figure 2.3) and vector (Figure 2.4) meson nonets decompose into the trivial representation $\mathbf{1}$ and the adjoint representation $\mathbf{8}$

$$\mathbf{3} \otimes \overline{\mathbf{3}} = \mathbf{1} \oplus \mathbf{8}. \tag{2.1}$$

Similarly, the spin-1/2 baryon octet and spin-3/2 decuplet arrangements can be seen through

$$\mathbf{3} \otimes \mathbf{3} \otimes \mathbf{3} = \mathbf{1} \oplus \mathbf{8} \oplus \mathbf{8} \oplus \mathbf{10}. \tag{2.2}$$

If the $\mathrm{SU}(3)$-flavour symmetry were exact, all particles in each representation would have the same masses; the small mass differences between the members of each representation comes from the explicit symmetry breaking of this symmetry group.

Since the quarks are spin-1/2, they can be either spin-up or spin-down. If we combine this together with the flavour symmetry, our quark vector now has 6 elements, correspond-

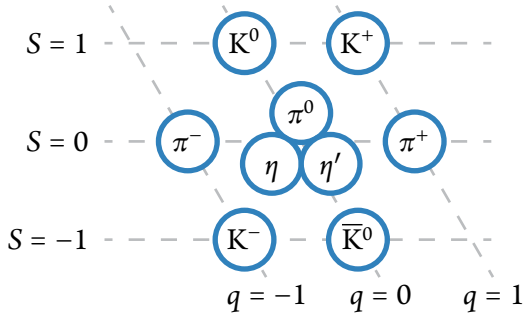

Figure 2.3: The pseudoscalar meson nonet. Particles are arranged in the same fashion as in Figure 2.1. The η' belongs to the singlet **1** representation, while the rest to the octet **8** representation.

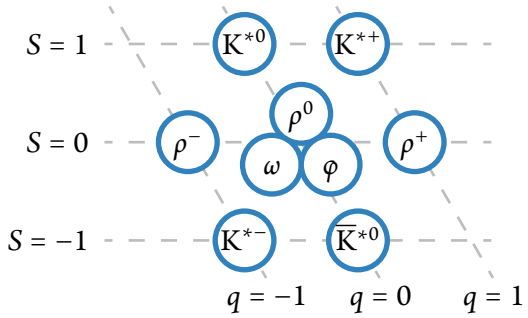

Figure 2.4: The vector meson nonet. Particles are arranged in the same fashion as in Figure 2.1.

ing to the three flavours with two spins per flavour, and our SU(3)-flavour symmetry has been promoted to a SU(6)–spin-flavour symmetry. This model then naturally represents all of the ground-state particles through

$$\mathbf{6} \otimes \overline{\mathbf{6}} = \mathbf{1} \oplus \mathbf{35} \tag{2.3}$$

$$\mathbf{6} \otimes \mathbf{6} \otimes \mathbf{6} = \mathbf{20} \oplus \mathbf{56} \oplus \mathbf{70} \oplus \mathbf{70}. \tag{2.4}$$

In the case of the ground-state baryons, with spatially-symmetric wave functions, only **56** is permitted – so that the baryons can satisfy Fermi-Dirac statistics, we need a wave function that is fully symmetric in spin-flavour, and only this term provides this. Moreover, we can split this into the spin-flavour components through

$$\mathbf{56} = (\mathbf{8}, 2) \oplus (\mathbf{10}, 4), \tag{2.5}$$

where we immediately see the octet and decuplet structures. For the mesons, splitting the terms into the spin-flavour components gives us

$$\mathbf{1} = (\mathbf{1}, 1) \quad \text{and} \quad \mathbf{35} = (\mathbf{1}, 3) \oplus (\mathbf{8}, 3) \oplus (\mathbf{8}, 1), \tag{2.6}$$

and we identify the pseudoscalar meson nonet with $(\mathbf{8}, 1) \oplus (\mathbf{1}, 1)$ and the vector meson nonet with $(\mathbf{8}, 3) \oplus (\mathbf{1}, 3)$. In the pseudoscalar sector, the symmetry is respected and the η' meson is the $(\mathbf{1}, 1)$. However, flavour symmetry is broken in the vector sector with the φ dominated by $s\bar{s}$.

2.3 Quantum Chromodynamics

While the quark model gives us an effective method for describing the lowest-lying meson and baryon multiplets, it is clearly not the whole story. The model cannot reproduce the mass—or even relative position—of the lightest positive- $(\mathrm{N}^*(1440))$ or negative-parity $(\Lambda^*(1405))$ excitations [30, 31]. Moreover, recent discoveries of exotic states such as the tetraquark $Z^-(4430)$ [32] and pentaquark $P_c^+(4380)$ and $P_c^+(4450)$ [33] are well beyond the scope of the quark model.

In addition to these, there are two major issues with the quark model as it stood during the mid-1960s. The spin-3/2 Δ^{++} would be required to contain three up quarks with parallel spin but zero orbital angular momentum. The same is true for the Ω^-, except with three strange, instead of up, quarks. Since quarks are fermions, such an arrangement should not be possible due to the Pauli exclusion principle, unless the quarks carry an additional, hidden quantum number.

There were two initial explanations to allow the quark model to describe the Δ^{++} and Ω^-. Firstly, in [34], it was proposed that the quarks obeyed order-3 parafermionic statistics instead of order-1 (the traditional Fermi-Dirac statistics), and [35] extended this with an internal SU(3) symmetry that did not commute with the SU(3) flavour symmetry of the quark model.

The internal SU(3) symmetry picture was redeveloped using ordinary Fermi-Dirac statistics for the quarks in [36]. Here, this internal symmetry is independent of the quark flavour (i.e. it commutes with SU(3)-flavour). Since there are three values for the corresponding charge, it became known as the "colour" charge, and the values "red", "green", "blue"; thus, quantum chromodynamics was born.

Quantum chromodynamics (QCD) is now believed to be the correct theory for describing the strong interaction. It is formulated as a Yang-Mills gauge theory [37] based on the SU(3) group, and we provide a brief introduction to the theory in this section. For more detailed references see, for example, [38–40].

2.3.1 Local Gauge Invariance

Consider some free, fermionic, field $\psi\colon \mathbb{M}^4 \to V$ of mass m mapping the Minkowski space-time $\mathbb{M}^4$ to some n-dimensional complex vector space $V = \mathbb{C}^n$. We can immediately write down the Lagrangian density associated with this field by

$$\mathcal{L}_{\text{free}}(x) = \overline{\psi}(x)(\mathrm{i}\gamma^\mu \partial_\mu + m)\psi(x). \tag{2.7}$$

Suppose now that in addition to the space-time degrees of freedom, the universe has some additional, internal degrees of freedom that correspond to some matrix Lie group $G \subseteq \mathrm{GL}(n, \mathbb{C})$. Our Lagrangian density should be invariant under the action of G on the vector space V – that is, $\mathcal{L}_{\text{free}} \mapsto \mathcal{L}_{\text{free}}$ for all $h \in G$.

If we pick a basis for V, we can—without loss of generality—associate a matrix $M_h \in \mathrm{M}(n, \mathbb{C})$ to each element $h \in G$ such that the action of h on V is ordinary matrix multiplication: $\psi(x) \mapsto M_h\,\psi(x)$. Clearly, the Lagrangian density is already invariant under this transformation:

$$\begin{aligned}
\mathcal{L}_{\text{free}}(x) &\mapsto \overline{\psi}(x)\, M_h^\dagger (\mathrm{i}\gamma_\mu \partial_\mu + m)\, M_h\, \psi(x) \\
&= \overline{\psi}(x)\, M_h^\dagger M_h (\mathrm{i}\gamma_\mu \partial_\mu + m)\, \psi(x) \\
&= \overline{\psi}(x)(\mathrm{i}\gamma_\mu \partial_\mu + m)\psi(x) \\
&= \mathcal{L}_{\text{free}}(x).
\end{aligned} \tag{2.8}$$

Furthermore, it should not matter if we apply a different transformation from G at each location in space-time. Again, we can without loss of generality represent the action of h on V through matrix multiplication, but this time the associated matrix M_h depends (differentiably) on x. Consequently, the derivative ∂ acts non-trivially on M_h, and so the Lagrangian density is not invariant:

$$\begin{aligned}
\mathcal{L}_{\text{free}}(x) &\mapsto \overline{\psi}(x)\, M_h(x)^\dagger (\mathrm{i}\gamma_\mu \partial_\mu + m)\, M_h(x)\, \psi(x) \\
&= \overline{\psi}(x)\, M_h(x)^\dagger M_h(x)\, (\mathrm{i}\gamma_\mu \partial_\mu + m)\, \psi(x) + \mathrm{i}\,\overline{\psi}(x)\, M_h(x)^\dagger \gamma_\mu (\partial_\mu M_h)(x)\, \psi(x) \\
&= \mathcal{L}_{\text{free}}(x) + \mathrm{i}\,\overline{\psi}(x)\, M_h(x)^\dagger \gamma_\mu (\partial_\mu M_h)(x)\, \psi(x) \\
&\neq \mathcal{L}_{\text{free}}(x).
\end{aligned} \tag{2.9}$$

That this should happen becomes obvious when we remember that the derivative is, in effect, comparing the value of the field at two (infinitesimally-separated) locations:

$$\frac{\partial \varphi}{\partial x} := \lim_{\varepsilon \to 0} \frac{\varphi(x+\varepsilon) - \varphi(x)}{\varepsilon}. \tag{2.10}$$

Not only do we get a term from the change in the field itself, but we also see the change in the applied gauge transformation; if we want to apply the derivative operator in a gauge-covariant fashion, we need to take this into account.

With this in mind, let us consider a covariant derivative construction of the form

$$D_\mu = \partial_\mu - \mathrm{i}gA_\mu(x), \tag{2.11}$$

where we have introduced a new vector field $A_\mu(x) := \mathbf{A}_\mu(x) \cdot \boldsymbol{\lambda}$, where $\mathbf{A}_\mu(x) = (A^1_\mu(x), \ldots, A^m_\mu(x))$, and $\boldsymbol{\lambda} = (\lambda_1, \ldots, \lambda_m)$ are the generators of the gauge group; let us call this field the "gauge field". We then require that $D_\mu\psi$ transforms like ψ so that the Lagrangian is invariant:

$$h(D_\mu\psi(x)) = M_h(x)\, D_\mu\psi(x). \tag{2.12}$$

Substituting in our definition for D_μ, on the left-hand side we have

$$\begin{aligned} h(D_\mu\psi(x)) &= (\partial_\mu - \mathrm{i}g\,h(A_\mu(x)))\, h(\psi(x)) \\ &= \partial_\mu(M_h(x)\,\psi(x)) - \mathrm{i}g\,h(A_\mu(x))\, M_h(x)\,\psi(x) \\ &= (\partial_\mu M_h(x))\,\psi(x) + M_h(x)\,\partial_\mu\psi(x) - \mathrm{i}g\,h(A_\mu(x))\, M_h(x)\,\psi(x), \end{aligned} \tag{2.13}$$

while on the right we have

$$\begin{aligned} M_h(x)\, D_\mu\psi(x) &= M_h(x)(\partial_\mu - \mathrm{i}gA_\mu(x))\,\psi(x) \\ &= M_h(x)\,\partial_\mu\psi(x) - \mathrm{i}g M_h(x)\, A_\mu(x)\,\psi(x). \end{aligned} \tag{2.14}$$

Setting these equal to each other again and rearranging, we have

$$h(A_\mu(x))\, M_h(x)\,\psi(x) = M_h(x)\, A_\mu(x)\,\psi(x) - \frac{i}{g}(\partial_\mu M_h(x))\,\psi(x), \tag{2.15}$$

or equivalently,

$$h(A_\mu(x)) = M_h(x)\, A_\mu(x)\, M_h(x)^{-1} - \frac{i}{g}(\partial_\mu M_h(x))\, M_h(x)^{-1}. \tag{2.16}$$

The first term is the gauge transformation if the gauge field transforms under the adjoint representation, while the second term encodes how the gauge transformation changes around x. In terms of differential geometry, the gauge field forms a connection form.

To complete our gauge-invariant Lagrangian density, we need to include a kinematic term for the gauge field. Such a term would need to be gauge invariant in its own right yet only depend on the gauge field itself – the appropriate quantity to include is the field-strength form,

$$F_{\mu\nu} = \frac{\mathrm{i}}{g}[D_\mu, D_\nu]. \tag{2.17}$$

While this is not gauge invariant, its square is, and so we write

$$\mathcal{L}_{\mathrm{gf}}(x) = -\frac{1}{2}\operatorname{tr} F^2 = -\frac{1}{4}\mathbf{F}_{\mu\nu} \cdot \mathbf{F}^{\mu\nu}, \tag{2.18}$$

where $\mathbf{F}_{\mu\nu} = (F^1_{\mu\nu}, \ldots, F^m_{\mu\nu})$ for the gauge field component of the Lagrangian density. We now have everything we need to write down the full, locally–gauge-invariant Lagrangian for our theory:

$$\mathcal{L}(x) = \overline{\psi}(x)(\mathrm{i}\gamma^\mu D_\mu + m)\psi(x) - \frac{1}{2}\operatorname{tr} F^2. \tag{2.19}$$

2.4 Properties of Quantum Chromodynamics

The Lagrangian density of Equation (2.19) is quite unremarkable. Written thus, it looks like that of quantum electrodynamics (QED), the gauge field theory formed from $G = \mathrm{U}(1)$ (the trace operation in the kinematic term for the gauge field does nothing in the case of QED, since there is only a single gauge degree of freedom, and so we generally leave it off). Since QED is a relatively simple, well-understood theory, can the same be said for QCD?

It turns out that the answer to this question is an emphatic *no*. To see this, we expand out the definition of the curvature form to get

$$\begin{aligned} F_{\mu\nu} &= \frac{\mathrm{i}}{g}\left[\partial_\mu - \mathrm{i}\,g A_\mu, \partial_\nu - \mathrm{i}\,g A_\nu\right] \\ &= \frac{\mathrm{i}}{g}\left[\partial_\mu, \partial_\nu\right] + \left[\partial_\mu, A_\nu\right] + \left[A_\mu, \partial_\nu\right] - \mathrm{i}\,g\left[A_\mu, A_\nu\right] \\ &= \partial_\mu A_\nu - \partial_\nu A_\mu - \mathrm{i}\,g\left[\mathbf{A}_\mu \cdot \boldsymbol{\lambda}, \mathbf{A}_\mu \cdot \boldsymbol{\lambda}\right] \\ &= \partial_\mu A_\nu - \partial_\nu A_\mu - \mathrm{i}\,g A^a_\mu A^b_\mu \left[\lambda_a, \lambda_b\right] \\ &= \partial_\mu A_\nu - \partial_\nu A_\mu + g f^{abc} A^a_\mu A^b_\mu \lambda_c, \end{aligned} \tag{2.20}$$

where f^{abc} are the structure constants for the associated Lie algebra, $\mathrm{Lie}(G)$. The first two terms here are standard kinematic terms for a massless vector boson, while the last allows the vector boson to self-interact. If the associated Lie algebra is Abelian, the structure constants are all zero, and so this last term is zero and there are no self-interactions between the vector bosons. This is the case for $G = \mathrm{U}(1)$ – that is, QED.

On the other hand, if the gauge group is non-Abelian, then we permit three- and four-point interactions involving only the gauge fields, and this is the case for QCD. Feynman diagrams for the interactions permitted by Abelian (QED) and non-Abelian (QCD) gauge field theories are presented in Figure 2.5. Moreover, these gauge field self-interactions naturally generate a significantly richer (and more complicated) theory, with perhaps the two most famous emergent properties being colour confinement and asymptotic freedom.

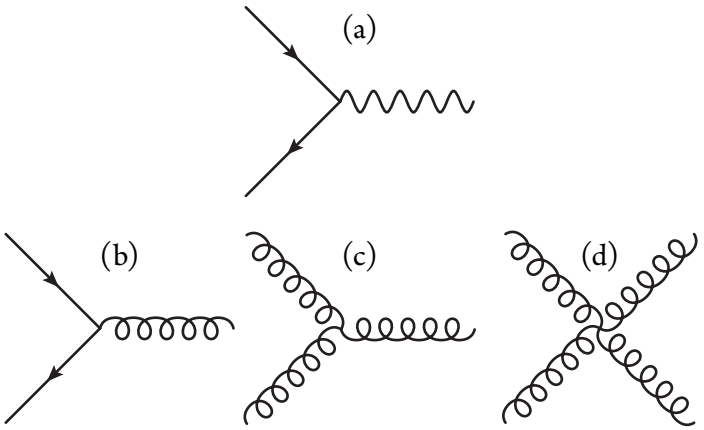

Figure 2.5: Feynman diagrams describing interaction vertices permitted by (top) quantum electrodynamics and (bottom) quantum chromodynamics. (a) Fermion-photon interaction. (b) Fermion-gluon interaction. (c) Three-gluon interaction. (d) Four-gluon interaction.

2.4.1 Asymptotic Freedom

A key feature of quantum field theories is the spontaneous and continuous creation and destruction of virtual fermion-antifermion pairs, with "empty space" being anything but empty. In the vicinity of a charge, these virtual fermion-antifermion pairs become naturally aligned with the field lines of the charge: the opposite-charged fermions are attracted to the charge while the like-charged fermions are repelled. The net effect is to partially cancel out or "screen" the field, and as one moves closer to the charge (or equivalently, probes at higher energies), this screening naturally decreases resulting in an increase to the effective charge.

In the case of QED, where the fermions are the only charged particles, this is the only consideration. However in QCD, the situation is different: the fermion-antifermion pairs still provide the same screening effect to the colour charge, however we now also have to consider the virtual gluon-gluon pairs – these produce the opposite effect and result in a decrease to the effective charge.

Which of these two effects is dominant depends on the number of flavours of quarks: if there are less than 16 flavours, the gluon "anti-screening" is dominant, while if there are more than this, the fermion screening is dominant. Since there are only 6 known flavours of quarks, we are in the first category. Thus, the effective colour charge decreases at higher energies and so we say that QCD is "asymptotically free".

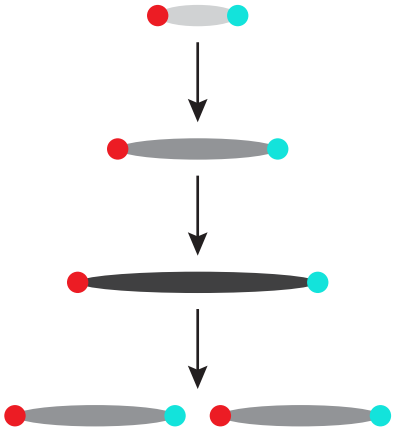

Figure 2.6: An attempt to separate and isolate a pair of quarks. As one continues to apply energy while separating the quarks, eventually the gluon field flux tube linking the quarks snaps to form a quark-antiquark pair.

2.4.2 Confinement

In the case of QED, the electric field between charged particles decreases as they are separated, with a natural result that you can effectively and practically isolate the fermions (for example, an electron). However, in the case of QCD, since the gluons also carry colour charge, the gluon field does not decrease with the distance; instead, a narrow flux tube forms between the fermions, and the strong force between them remains approximately constant regardless of their separation.

If one were to attempt to separate a pair of quarks, the energy in the flux tube connecting the quarks increases linearly with the separation. As a result, eventually it will become energetically favourable to create a quark-antiquark pair, and "snap" the flux tube into two separate flux tubes, as depicted in Figure 2.6. Thus, it is not possible to isolate the fermions in QCD – they can only exist in bound states, such as the quark-antiquark mesons and the quark-quark-quark baryons.

2.5 Path Integral Formulation

As a generalisation of the principle of least action from classical mechanics, we can represent a quantum process as a sum over all possible field configurations with an appropriate weighting phase for each field configuration. This represents an alternative approach to the

canonical quantization method, and is a valuable tool for working with field theories. For a given field φ, we write the generating function as

$$\mathcal{Z} := \int \mathcal{D}\varphi \exp(\mathrm{i}\, S[\varphi]), \tag{2.21}$$

where the action functional S is obtained from the Lagrangian density through

$$S[\varphi] := \int \mathcal{L}(\varphi; x)\, \mathrm{d}^4 x, \tag{2.22}$$

and the integration measure defined by

$$\mathcal{D}\varphi := \prod_x \mathrm{d}\varphi(x). \tag{2.23}$$

To calculate vacuum expectation values for an observable, we need only include the associated operator in the integral and normalise by the partition function:

$$\begin{aligned} \langle \mathcal{O} \rangle &= \frac{1}{\mathcal{Z}} \int \mathcal{D}\varphi\, \mathcal{O}[\varphi] \exp(\mathrm{i}\, S[\varphi]) \\ &= \frac{\int \mathcal{D}\varphi\, \mathcal{O}[\varphi] \exp(\mathrm{i}\, S[\varphi])}{\int \mathcal{D}\varphi \exp(\mathrm{i}\, S[\varphi])}. \end{aligned} \tag{2.24}$$

If we recall the equivalent quantities from statistical mechanics, this formula looks very similar, and indeed $\mathcal{Z}$ is often referred to as the "partition function". The only difference is that factor of i in the exponent; as a consequence, the integrands oscillate instead of decaying as in the classical case. Unfortunately, this minor change means that in general we cannot directly evaluate them. However, by applying the Wick rotation $t \to -\mathrm{i}t_E$ and formulating the theory in Euclidean time, the generating function takes the form

$$Z = \int \mathcal{D}\varphi \exp(-S_E[\varphi]); \tag{2.25}$$

this now has the correct form to be labelled a partition function.

✣ Three ✣
Lattice Quantum Chromodynamics

Lattice quantum chromodynamics (lattice QCD) is a first-principles, non-perturbative method for studying low-energy quantum chromodynamics (QCD) [41]. The method involves the formulation of QCD on a finite space-time lattice (and so is a lattice gauge theory) such that, in the limit of the lattice extent going to infinity and the lattice spacing going to zero, continuum QCD is recovered.

Since its initial presentation in 1974 [41], lattice QCD has demonstrated remarkable success [42]. Lattice QCD can reproduce the hadronic ground-state spectrum to within a few percent of the physical values, and, in some cases, has even correctly predicted the mass of some states to higher accuracy and precision than the then-experimentally-measured values – for example, the pseudoscalar and vector charmed B mesons [43, 44]. Moreover, in recent years, lattice QCD has been used to demonstrate a connection between SU(3) centre vortices and the two main features of QCD: the confinenent of quarks within hadrons, and dynamical mass generation and chiral symmetry breaking [45–47].

In this chapter we present an introduction to lattice QCD, and outline the basic concepts and methods used. For a more detailed overview, we defer to texts such as [48] (from which much of the treatment here has been derived) and [49]. For more detailed descriptions of the lattice actions used in this chapter, see the references cited therein.

3.1 QCD on a Lattice: The Wilson Actions

3.1.1 Defining a Space-Time Lattice

Perhaps the simplest discretisation of space-time is that of a hypercubic grid of regularly-spaced points. If a is the spacing between these points, then we can naturally describe the (now countably-infinite) locations of our new space-time as $x = an$, where $n \in \mathbb{Z}^4$ is the (multi-dimensional) index of the site. Let $\mathbb{L}$ denote the set of all lattice sites. The formulation of QCD onto the lattice of space-time points is, in essence, a choice of appropriate

gauge and quark actions, and as long as we reproduce the physical theory in the continuum limit, $a \to 0$, we have quite a lot of flexibility in this regard. Perhaps the most natural starting point is to consider actions with the same form as continuum QCD.

Integration over all space-time points has a natural analogue in a sum over the lattice sites,

$$\int \mathrm{d}^4 x \to a^4 \sum_{n \in \mathbb{L}}, \tag{3.1}$$

however discretising the derivative is less obvious. Let us first consider the definition of the derivative,

$$\partial_\mu \varphi(x) := \lim_{h \to 0} \frac{\varphi(x + h\hat{\mu}) - \varphi(x)}{h}, \tag{3.2}$$

where $\hat{\mu}$ is a unit vector in the x_μ direction. It is tempting to just remove the limit and set h to a – this is the forward difference operator, δ_μ^+ – however such a choice almost immediately runs into problems: its determinant is, in general, complex. The same thing happens if we use the backward difference operator, δ_μ^-, so instead let us use the central difference operator,

$$\partial_\mu \varphi(x) \to \delta_\mu \varphi(an) := \frac{\varphi(an + a\hat{\mu}) - \varphi(an - a\hat{\mu})}{2a}. \tag{3.3}$$

3.1.2 The Wilson Gauge Action

In the continuum, the gauge fields naturally arise as a means of ensuring the local gauge invariance of the derivative operator. Indeed, the same process is needed here, since our derivative operator is not locally gauge invariant. However, instead of working directly with the gauge fields, we work with the matrices they generate:

$$\begin{aligned} U_\mu(an) &:= \mathcal{P} \exp\left(\frac{\mathrm{i}g}{2} \int_{an}^{an + a\hat{\mu}} A_\mu(z) \cdot \lambda \, \mathrm{d}z\right) \\ &\simeq \exp(\mathrm{i}agA_\mu(an)), \end{aligned} \tag{3.4}$$

The approximation in the second line is valid for small a and comes from treating the gauge field as constant across the integration region. Using this, we can define a discretised covariant derivative in the covariant central difference operator:

$$\nabla_\mu \varphi(an) = \frac{U_\mu(an)\varphi(an + a\hat{\mu}) - U_\mu^\dagger(an - a\hat{\mu})\varphi(an - a\hat{\mu})}{2a}. \tag{3.5}$$

In keeping with their role as parallel transporters, since they carry dependence on both location and direction we can associate them with "links" joining one lattice site to another. If we think of local gauge transformations as changing the basis for the vector space

at each location on the lattice, then the gauge matrices associated with a lattice site simply describe the basis transformations needed to bring vectors at neighbouring sites into the vector space of this site: if $\psi(an) \in V(an)$, then $U_\mu(an)\psi(an + a\hat{\mu}) \in V(an) \cong V(an + a\hat{\mu})$. The adjoint of the gauge field does exactly the opposite, transforming a vector from the current site's vector space basis to that of the neighbouring sites: $U_\mu^\dagger(an)\psi(an) \in V(an + a\hat{\mu}) \cong V(an)$.

The gauge fields transform in the adjoint representation of the gauge group, and so we can immediately write down the action of a gauge transformation $G(x) \in \mathrm{SU}(3)$ on the gauge field:

$$U_\mu(an) \mapsto G(an)U_\mu(an)G^{-1}(an + a\hat{\mu}). \tag{3.6}$$

With this, we can see that the only gauge-invariant field combinations are where we either start and end at the same location, or start and end with a fermion. Some example gauge-invariant paths are shown in Figure 3.1. Thus, the simplest combination involving only the gauge field is the 1×1 "plaquette" loop:

$$P_{\mu\nu}(an) = U_\mu(an)U_\nu(an + a\hat{\mu})U_\mu^\dagger(an + a\hat{\nu})U_\nu^\dagger(na). \tag{3.7}$$

Using the approximation in Equation (3.4) together with the Baker-Campbell-Hausdorff formula, we can express this in terms of the the gauge field's curvature form, with

$$P_{\mu\nu}(an) \simeq \exp\left(\mathrm{i}(a^2 g F_{\mu\nu}(an) + \mathcal{O}(a^3))\right). \tag{3.8}$$

From this, we can obtain an identity of the same form as the kinetic term for the continuum gauge field by Taylor expanding this:

$$\mathbb{I}_3 - \frac{P_{\mu\nu} + P_{\mu\nu}^\dagger}{2} = \frac{a^4 g^2}{2} F_{\mu\nu}F_{\mu\nu} + \mathcal{O}(a^6). \tag{3.9}$$

Thus, the simplest discretisation of the gluon action is

$$S_{\mathrm{G}}[U] = \frac{2a^4}{g^2} \sum_n \sum_{\mu>\nu} \mathrm{tr}\left(\mathbb{I}_3 - \frac{P_{\mu\nu}(an) + P_{\mu\nu}^\dagger(an)}{2}\right), \tag{3.10}$$

where the constant $2/g^2$ is chosen to ensure we get the correct normalisation in the continuum limit. Recognising that $X + X^\dagger = 2\,\mathfrak{Re}\,X$, it is common to write this in the form

$$S_{\mathrm{G}}^{\mathrm{W}}[U] = \beta a^4 \sum_n \sum_{\mu>\nu} \left(1 - \frac{\mathfrak{Re}\,\mathrm{tr}\,P_{\mu\nu}(an)}{3}\right), \tag{3.11}$$

where $\beta = 6/g^2$, and this is known as the Wilson gauge action.

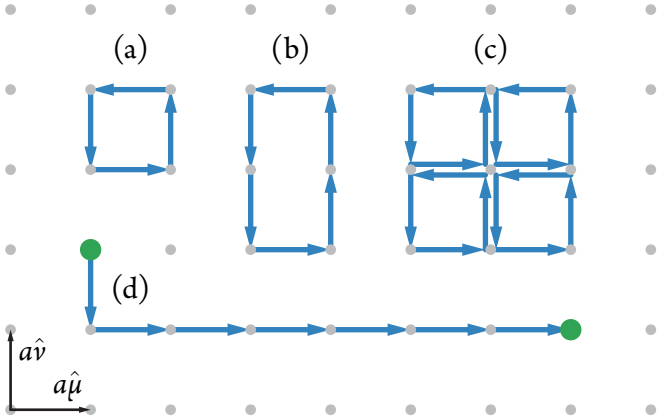

Figure 3.1: Examples of gauge-invariant combinations of discretised fields. For simplicity, we have only drawn this in two space-time dimensions. The gray points represent the lattice sites, the blue lines the gauge field links joining the lattice sites, and the green points the fermion source and sink operators. (a) The 1×1 rectangle, $R_{\mu\nu}^{1\times1}$, also known as the "plaquette", $P_{\mu\nu}$; this is the simplest gauge-invariant quantity that can be constructed using only gauge field links. (b) The 1×2 rectangle, $R_{\mu\nu}^{1\times2}$; this combination is employed in the Iwasaki gauge action used to construct the ensembles used in this work, and is discussed in Section 3.2.1. (c) The clover operator $C_{\mu\nu}$; this is commonly used to evaluate the curvature form $F_{\mu\nu}$ on the lattice and is discussed in Section 3.2.2. (d) A path starting and ending with a fermion source and sink, respectively.

3.1.3 Fermions on the Lattice: A Naïve Approach

If we consider the fermionic part of the continuum action,

$$S_{\mathrm{F}}[A_\mu, \psi] = \int \mathcal{L}_{\mathrm{F}}(A_\mu, \psi, x)\, \mathrm{d}^4x = \int \overline{\psi}(x)(\gamma_\mu D_\mu + m)\psi(x)\, \mathrm{d}^4x, \tag{3.12}$$

we can immediately write down a discretised version:

$$S_{\mathrm{F}}[U_\mu, \psi] = a^4 \sum_n \overline{\psi}(an)(\gamma_\mu \nabla_\mu + m)\psi(an). \tag{3.13}$$

Using the definition of the discretised covariant derivative, this becomes

$$S_{\mathrm{F}}[U_\mu, \psi] = a^4 \sum_n \left(\frac{\overline{\psi}(an)\gamma_\mu U_\mu(an)\psi(an + a\hat{\mu})}{2a} - \frac{\overline{\psi}(an)\gamma_\mu U_\mu^\dagger(an - a\hat{\mu})\psi(an - a\hat{\mu})}{2a} + m\overline{\psi}(an)\psi(an) \right) \quad (3.14)$$

While this takes the correct form in the continuum limit, it unfortunately does not describe the same quantum theory. To see this, we begin by writing down the momentum space Feynman propagator in the continuum:

$$S(p) = \frac{\gamma \cdot p - m}{p^2 - m^2}. \quad (3.15)$$

For a massless particle, this clearly has a single pole at $p = 0$. This pole comes from the Fourier transformation of the continuum derivative operator, and so to see the momentum structure of the discretised form, we need only consider the Fourier transform of the discretised derivative operator, the central difference operator:

$$\begin{aligned} \mathcal{F}(\delta_\mu \psi)(p) &= \frac{\mathcal{F}(\delta_\mu^+ \psi)(p) - \mathcal{F}(\delta_\mu^- \psi)(p)}{2} \\ &= \frac{\exp(\mathrm{i}ap_\mu)\,\hat{\psi}(p_\mu) - \exp(-\mathrm{i}ap_\mu)\,\hat{\psi}(p_\mu)}{2a} \\ &= \frac{\mathrm{i}}{a}\sin(ap_\mu)\,\hat{\psi}(p_\mu), \end{aligned} \quad (3.16)$$

where $\hat{\psi}$ is the Fourier transform of ψ. This has zeros at $p_\mu \in \{0, \pi/a\}$. The zero at the origin corresponds to the zero in the continuum theory, but the extra 15 zeros will also produce momentum distributions of that of a single particle propagator – that is, we are actually describing a theory with 16 species of fermion! This is the infamous fermion doubling problem, so-named because the number of fermion species goes as 2^d where d is the number of space-time dimensions, and essentially makes this lattice formulation useless for our studies.

3.1.4 Wilson Fermions

Previously we discussed that we have quite some flexibility in choosing our lattice formulation, so the question now is, can we use that flexibility to solve the fermion doubling problem? It turns out that this is not strictly possible – in [50], it is shown that it is impossible to solve the fermion doubling problem without violating one of the properties of

the original continuum theory, such as chiral symmetry or translational invariance. But as long as we can make this sacrifice without changing the physics we are interested in, we have hope.

In [41], Wilson proposed a modification of the fermion action to include a term that vanishes in the continuum limit, but raises the mass of the extra species of fermions; in the continuum limit, the extra fermions then become infinitely heavy and so decouple from the theory. The extra term makes use of the Wilson operator,

$$\Delta\psi(an) = \frac{1}{a^2}\sum_{\mu}\left(2\psi(an) - U_\mu(an)\psi(an + a\hat{\mu}) - U_\mu^\dagger(an - a\hat{\mu})\psi(an - a\hat{\mu})\right), \tag{3.17}$$

and produces the fermion action

$$S_{\mathrm{F}}[U_\mu, \psi] = a^4 \sum_n \overline{\psi}(an)\left(\gamma_\mu \nabla_\mu + \frac{ra}{2}\Delta + m\right)\psi(an), \tag{3.18}$$

where r is the Wilson parameter, usually set to 1.

To see how this resolves the issue of the extra fermion species, we take the Fourier transform of the Wilson operator:

$$\begin{aligned}
\mathcal{F}(\Delta\psi)(p) &= \frac{1}{a^2}\sum_\mu \left(2\hat{\psi}(p) - \mathcal{F}(\delta_\mu^+\psi)(p) - \mathcal{F}(\delta_\mu^-\psi)(p)\right) \\
&= \frac{1}{a^2}\sum_\mu \left(2 - \frac{\exp(\mathrm{i}ap_\mu) + \exp(-\mathrm{i}ap_\mu)}{2a}\right)\hat{\psi}(p_\mu) \\
&= \frac{2}{a^2}\sum_\mu \left(1 - \cos(ap_\mu)\right)\hat{\psi}(p_\mu).
\end{aligned} \tag{3.19}$$

This still contains a zero at $p = 0$, however it is non-zero at all the other zeros of Equation (3.16). As a result, the overall Fourier transform has only a single zero, and so we end with a single species of fermion in the continuum limit. Unfortunately, the addition of this term explicitly breaks the chiral symmetry, but since we are working away from the chiral limit, it does not present a problem in this work. Standard renormalisation techniques allow the identification of a base mass parameter that ensures $m_\pi \to 0$ as $m_q \to 0$. The Wilson term also introduces $\mathcal{O}(a)$ discretisation errors, but we can improve upon this as demonstrated in Section 3.2.2.

If we rescale the fermion fields by a factor of $\sqrt{ma + 4r}$, we can write the action as

$$S_{\mathrm{F}}^{\mathrm{W}}[U_\mu, \psi] = a^4 \sum_{n,m\in\mathbb{L}} \overline{\psi}(an)M(an, am)\psi(am), \tag{3.20}$$

where the Wilson fermion matrix is defined by

$$aM(x, y) = \delta_{x,y} - \kappa\sum_\mu \left((r - \gamma_\mu)U_\mu(x)\delta_{x+a\hat{\mu},y} + (r + \gamma_\mu)U_\mu^\dagger(x - a\hat{\mu})\delta_{x-a\hat{\mu},y}\right), \tag{3.21}$$

where

$$\kappa = \frac{1}{2ma + 8r}. \tag{3.22}$$

The parameter κ essentially describes the strength of the coupling between the fermion field at a given site to that at its neighbours, and so it is often known as the hopping parameter.

3.2 Improvements to the Lattice Actions

As noted previously, our choice of lattice actions is quite arbitrary, as long as we reproduce the correct continuum theory in the continuum limit. We used this feature in Section 3.1.4 to solve the fermion doubling problem. Our current actions have discretisation errors of $\mathcal{O}(a^2)$ for the gauge component and $\mathcal{O}(a)$ for the fermion component; can we use this flexibility to reduce these errors? The general approach to these methods is to add extra, higher-dimensional, so-called "irrelevant" operators that vanish in the continuum limit. In this section we specify the improved gauge and fermion actions that are used in this work, but leave detailed descriptions for the references listed therein.

3.2.1 The Iwasaki Gauge Action

One approach to improving the gauge action is to formulate the renormalisation group equations onto the lattice and use these to estimate, non-pertubatively, the coefficients of various irrelevant operators in an effort to move as close as possible to the renormalised trajectory. The PACS-CS configurations that we use in this work ([51], with a description in Section 3.4) were constructed using the Iwasaki gauge action [52] of the form

$$S_{\mathrm{G}}^{\mathrm{Iwasaki}}[U] = \beta \sum_{n} \sum_{\mu>\nu} \left(c_0 \, \mathfrak{Re} \operatorname{tr} R_{\mu\nu}^{1\times 1}(an) + c_1 \, \mathfrak{Re} \operatorname{tr} R_{\mu\nu}^{1\times 2}(an) \right), \tag{3.23}$$

where $R_{\mu\nu}^{1\times 1} = P_{\mu\nu}$ is the 1×1 plaquette discussed previously and $R_{\mu\nu}^{1\times 2}$ is the 1×2 rectangle (see Figure 3.1 for a pictorial representation), and the coefficients are $c_0 = 3.648$ and $c_1 = -0.331$.

3.2.2 The Wilson Clover Action

The $\mathcal{O}(a)$ errors introduced by the Wilson term in removing the fermion doubling problem are particularly troubling. Being at such a low order in a, we would need to use a very fine lattice in order to prevent these becoming a significant contribution to our results. To keep the lattice volume constant and avoid finite volume effects, we would therefore need

to use very large lattices, and this would naturally lead to an enormous increase on computational effort.

In [53], the inclusion of dimension-5 operators is proposed with coefficients selected to cancel the $\mathcal{O}(a)$ errors of the original Wilson fermion action. This produces the Sheikholeslami-Wohlert action,

$$S_{\mathrm{F}}^{\mathrm{SW}}[U,\psi] := S_{\mathrm{F}}^{\mathrm{W}} - \frac{\mathrm{i}ga^5 c_{\mathrm{SW}} r}{4} \sum_n \overline{\psi}(an)\sigma_{\mu\nu}F_{\mu\nu}(an)\psi(na), \tag{3.24}$$

where the parameter c_{SW} can be tuned to remove the $\mathcal{O}(a)$ errors. In [54], the value of this parameter was tuned non-pertubatively using the renormalisation-group improved gauge action of the proceeding section to give $c_{\mathrm{SW}} = 1.715$.

This action is often known as the "clover" action due to the usual choice for evaluating the curvature form on the lattice:

$$ga^2 F_{\mu\nu}(x) = \frac{C_{\mu\nu}(x) - C_{\mu\nu}^{\dagger}(x)}{2\mathrm{i}}, \tag{3.25}$$

where the clover operator is

$$C_{\mu\nu}(x) := \frac{P_{\mu,\nu}(x) + P_{\nu,-\mu}(x) + P_{-\mu,-\nu}(x) + P_{-\nu,-\nu}(x)}{4} \tag{3.26}$$

and is depicted in Figure 3.1(c).

3.3 Calculating Observables on the Lattice

3.3.1 Path Integrals on the Lattice

Building on the path integral formulation discussed in Section 2.5, we consider its application to our discretisation of QCD. Combining the gauge and fermion action together to produce the full QCD action, we can write

$$S_{\mathrm{QCD}}[U,\psi] = S_{\mathrm{F}}[U,\psi] + S_{\mathrm{G}}[U], \tag{3.27}$$

and

$$Z = \int \mathcal{D}U\,\mathcal{D}\psi\,\mathcal{D}\overline{\psi}\exp(-S_{\mathrm{QCD}}[U,\psi]). \tag{3.28}$$

But, since the fermions fields must be Grassmann-number valued, we can immediately integrate them out using the properties of Grassmann integration, and this results in a much-simplified partition function:

$$\begin{aligned} Z &= \int \mathcal{D}U \det M[U] \exp(-S_{\mathrm{G}}[U]) \\ &= \int \mathcal{D}U \exp(-S_{\mathrm{eff}}[U]), \end{aligned} \tag{3.29}$$

where we have defined an effective action by

$$S_{\text{eff}}[U] := S_{\text{G}}[U] - \ln \det M[U]. \tag{3.30}$$

The determinant term encapsulates all of the sea quark loop interactions. By setting the $\det M$ equal to a constant we arrive at the "quenched" approximation, in which all these interactions are neglected. While substantially reducing the computational complexity, one neglects a lot of physics. In particular, we lose any virtual quark-antiquark pairs, which may be important for investigating the structure of the $\Lambda(1405)$ (especially if there are any meson-baryon bound state components, since we only consider 3-quark baryon creation and annihilation operators). As such, we avoid this approximation in this work.

We do however make use of partial quenching for the strange quark, in which the valence quarks have a different mass to the sea quarks. This is needed because the inputs for the generation of the ensembles we use in this work have a strange sea quark with a mass that is slightly too high. As long as the mass difference between the sea and valence versions of the quark is small enough, the impact of this on the results is expected to be minimal. More details on this can be found in Section 3.4.

In exactly the same fashion as for the action in the partition function, for a given operator $\mathcal{O}$ we can construct an effective version by integrating out the fermion fields, and this allows us to simplify the corresponding vacuum expectation value. In general, this equivalent effective operator will depend on the gauge fields and the inverse of the fermion matrix (i.e. the fermion propagator), and so we write

$$\langle \mathcal{O} \rangle = \frac{\int \mathcal{D}U \, \mathcal{O}_{\text{eff}}[U, M^{-1}[U]] \exp(-S_{\text{eff}}[U])}{\int \mathcal{D}U \exp(-S_{\text{eff}}[U])}. \tag{3.31}$$

Of course, to evaluate this completely is still a computationally expensive operation. As an order-of-magnitude exercise, consider a small $10 \times 10 \times 10 \times 10$ lattice. The number of lattice sites is 10 000, and since each lattice site has 4 forward-looking links, the number of unique gauge links is 40 000. Each of these gauge links is parameterised by 8 real variables, and so the integral over all gauge field configurations is equivalent to the integral over all 8 of these parameters for each gauge link – that is, a 320 000-dimensional integral! Even using a modest 10 points in each dimension, to numerically integrate this would involve the sum of an astronomical number of terms: $10^{320\,000}$. If we consider the current generation of Intel microprocessors, which can perform about 10^{12} additions per second[1], it would take about $10^{319\,988}$ seconds to evaluate this – or $10^{319\,970}$ times the age of the universe!

If the integrand is sampled randomly, the majority of the link configurations will produce very large actions, and so be exponentially suppressed in their contribution towards

[1] A 20-core Skylake processor running at 2.6 GHz can perform 8.32×10^{11} double-precision floating-point additions per second.

the expectation value in Equation (3.31). Only very few field configurations will make a significant contribution, and so if we sample the parameter space such that each configuration appeared with a weight corresponding to its Boltzmann factor $\exp(-S_{\text{eff}}[U])$, we can efficiently compute the vacuum expectation value as just the average across this sample:

$$\langle \mathcal{O} \rangle \simeq \frac{1}{n} \sum_{i=1}^{n} \mathcal{O}(U_i), \tag{3.32}$$

where $\{ U_i \mid i = 1, \ldots, n \}$ is the ensemble of "importance sampled" gauge field configurations.

3.3.2 Two-point Propagators on the Lattice

In the previous section, we discovered that we can integrate out the fermion fields to obtain effective operators that depend only on the gauge fields and the fermion propagator. Since all of the quark dependence is expressed through the propagator component, it is natural that this becomes a fundamental component when investigating hadrons on the lattice. To calculate the propagator, S, we use the fact that it is the inverse of the fermion matrix M:

$$M^{ab}_{\alpha\beta}(z,x) S^{bc}_{\beta\gamma}(x,y) = \delta^{ac} \delta_{\alpha\gamma} \delta(z-y), \tag{3.33}$$

In the case of the Wilson and clover fermion actions, we only have local, nearest, and next-nearest references, and so we can use sparse matrix inversion techniques to efficiently calculate the propagator. In particular, in this work we used BiCGStab [55] and CGNE [56].

Even using the accelerated sparse matrix inversion algorithms on modern hardware, to calculate all elements of the full propagator would require substantial computational investment. However, it is sufficient to only consider propagation from a single space-time site to all other sites.

3.3.3 Three-point Propagators on the Lattice

If we wish to investigate the internal structure of a hadron, we need to probe it with some external current j. This current will interact with the quark fields forming the hadron, and so such an investigation will involve calculating the three-point correlation function

$$S^{ab}_{\alpha\beta}(x,y,z) := \langle \Omega | q^a_\alpha(x)\, j(y)\, \overline{q}^b_\beta(0) | \Omega \rangle\,, \tag{3.34}$$

where $\overline{q}$ and q are the quark and antiquark fields, respectively, and $|\Omega\rangle$ is the vacuum state. We can write a general current vertex as

$$j(x) = \overline{q}(x)\, \Gamma\, q(x), \tag{3.35}$$

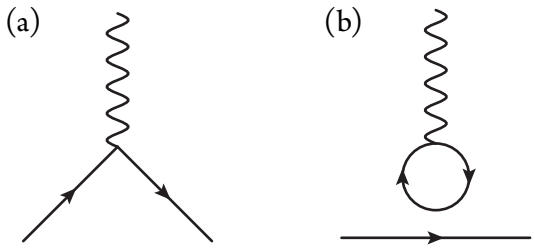

Figure 3.2: The two interaction components contributing to the three-point correlation function after Wick contraction. (a) The coupling of an inserted current to a valence quark, the so-called "connected" contribution. (b) The coupling of an inserted current to a sea quark, the "disconnected" contribution; these latter interactions are neglected in this work.

where the bilinear Γ describes the coupling at the vertex between the incoming and outgoing color-spin charge. Substituting this into the definition of the three-point propagator and performing the Wick contractions we see that there are two components: where the current couples to a valence quark, and where the current couples to a sea quark. Feynman diagrams for these are presented in Figure 3.2.

Evaluating the second of these components, involving disconnected loops, requires huge statistics, and is beyond the scope of this work. Only very recently are such contributions being directly included in lattice calculations [57–59] – and there only for ground-state baryons, not the excited states of interest in this work. Alternatively, if we are comparing against model predictions, we can explicitly exclude such diagrams from the model calculation to arrive an equivalent comparison, as is done in [60, 61].

Expressing the first component in terms of two-point (valence) quark propagators and taking the Fourier transform, we have

$$S^{ab}_{a\beta}(x, y_4, 0; \mathbf{q}) = \sum_{\mathbf{y}} \exp(\mathrm{i}\mathbf{q}\cdot\mathbf{y})\big(S(x,y)\Gamma S(y,0)\big)^{ab}_{a\beta}, \tag{3.36}$$

where 0 is the source for the two-point propagator and y_4 is the temporal component of y. While it looks like this would need the computationally-expensive all-to-all propagators discussed above, we can rewrite it as

$$M^{ab}_{a\beta}(z,x)S^{bc}_{\beta\gamma}(x, y_4, 0; \mathbf{q}) = \sum_{\mathbf{y}} \exp(\mathrm{i}\mathbf{q}\cdot\mathbf{y})\delta(z-x)\Gamma^{ad}_{a\delta}S^{dc}_{\delta\gamma}(y,0). \tag{3.37}$$

Now, we treat the right-hand side as the source for the three-point propagator and solve the resulting linear system in the same fashion as for the two-point propagator. This is the sequential source technique [62].

Since we will be interested in the electromagnetic structure of the $\Lambda(1405)$ for this work, we use the $\mathcal{O}(a)$-improved conserved vector current [63, 64]

$$j_\mu(an) := j^{\mathrm{c}}_\mu(an) + \frac{ra}{2}\sum_\nu \partial_\nu(\overline{q}(an)\sigma_{\nu\mu}q(an)), \tag{3.38}$$

where

$$\begin{aligned} j^{\mathrm{c}}_\mu(an) := \frac{1}{4}\Big(&\overline{q}(an)(\gamma_\mu - r)U_\mu(x)q(an + a\hat{\mu}) \\ &+ \overline{q}(an + a\hat{\mu})(\gamma_\mu + r)U^\dagger_\mu(an)q(an) \\ &+ \overline{q}(an - a\hat{\mu})(\gamma_\mu - r)U_\mu(an - \hat{\mu})q(an) \\ &+ \overline{q}(an)(\gamma_\mu + r)U^\dagger_\mu(an - a\hat{\mu})q(x - a\hat{\mu})\Big) \end{aligned} \tag{3.39}$$

is the conserved current for the Wilson action. To ensure all terms of the current are one-link terms, we treat the $\mathcal{O}(a)$ term as

$$\partial_\mu(\overline{q}(x)q(x)) = \overline{q}(x)(\overleftarrow{\nabla}_\mu + \overrightarrow{\nabla}_\mu)q(x), \tag{3.40}$$

where $\overleftarrow{\nabla}$ and $\overrightarrow{\nabla}$ are the forwards- and backwards-acting covariant derivative operators.

By ensuring all terms are one-link terms, the corrections to the tree-level couplings used herein do not encounter large non-perturbative mean-field improvement corrections associated with tadpole contributions. The remaining radiative corrections are anticipated to be small.

3.3.4 Statistical Analysis

Since we are now including only a sampling of all gauge field configurations in our path integrals, we need a method to estimate the statistical variance this naturally produces. In this work we use the jackknife resampling technique, which involves calculating the statistical estimator (in this case, the mean) across all subsamples (the "sub-ensembles") that omit a specific number of configurations.

Let us first develop the delete-1 jackknife resampling method, where a single sample is removed when forming each sub-ensemble. If $\mathbb{U} = \{\, U_i \mid i = 1, \ldots, n \,\}$ is our set of n gauge fields configurations, then we define $\mathbb{U}_i$ to be the set of these configurations with the i-th element removed:

$$\mathbb{U}_i := \mathbb{U} \setminus \{\, U_i \,\}. \tag{3.41}$$

On each of these subsets, we calculate the estimator s

$$s_i := s(\mathbb{U}_i), \tag{3.42}$$

and together these values form an estimate for the distribution of this estimator. In particular, it allows us to calculate the mean and variance of the estimator:

$$\bar{s} = \frac{1}{n}\sum_{i=1}^{n} s_i \quad \text{and} \quad \sigma^2(s) = \frac{n-1}{n}\sum_{i-1}^{n}(s_i - \bar{s})^2. \tag{3.43}$$

This naturally generalises to the delete-d case, where we remove d elements, keeping in mind that the normalisation of the mean and variance will change due to the change in the number of elements. Moreover, the higher-order jackknife subsamples allow us to estimate the distribution of quantities that themselves depend on the jackknife distribution. For example, if we consider linear least squares regression analysis, while the delete-1 jackknife allows us to estimate the weights of each input observation, we need the delete-2 jackknife to estimate the variance in the resulting parameters[2].

3.4 Ensembles Used in This Work

In this work we use the PACS-CS $(2+1)$-flavour full-QCD ensembles [51], made available through the ILDG [65]. The lattice has 32 points in each spatial direction and 64 points in the temporal direction, and have $\beta = 1.90$. The gauge fields are represented using the Iwasaki gauge action of Section 3.2.1 [52] with $c_0 = 3.648$ and $c_1 = -0.331$, while the fermions are represented using the clover quark action of Section 3.2.2 [53] with $c_{\mathrm{SW}} = 1.715$.

There are 5 light quark masses available, with light-quark hopping parameters $\kappa_{\mathrm{u,d}}$ of 0.137 00, 0.137 27, 0.137 54, 0.137 70, and 0.137 81. Setting the scale by extrapolating the Sommer parameter to the physical quark mass produces a lattice spacing of $0.0907(13)$ fm, and this gives pion masses ranging from 702 MeV/c^2 down to 156 MeV/c^2. We can also set the scale on each ensemble individually by considering the Sommer parameter for that particular ensemble, and this is what we use in this work. Table 3.1 summarises the properties of the five available ensembles.

The strange quark mass is the same for all light quark masses, with hopping parameter $\kappa_{\mathrm{s}} = 0.13640$. However, this is slightly too high to reproduce the physical kaon mass. Plotting the kaon mass data provided in [51] against m_π^2 in Figure 3.3 and extrapolating to the physical limit, we see that the kaon lies approximately 50 MeV/c^2 too high. We can calculate the κ_{s} required to reproduce a physical-mass kaon using two methods: first, by requiring the correct mass for the $s\bar{s}$ pseudoscalar meson, and second, by requiring the correct kaon mass at the lightest available light quark mass through the Gell-Mann–Oakes–Renner

[2]While the linear least squares method does produce an estimate for the variance (and covariance) of the parameters, it assumes a normal distribution for the input observations.

$\kappa_{u,d}$	κ_s	m_π^{phys}	m_π
0.137 00	0.136 40	701.0(100)	622.3(91)
0.137 27	0.136 40	569.8(83)	512.4(79)
0.137 54	0.136 40	411.3(61)	388.2(55)
0.137 70	0.136 40	295.7(52)	282.1(48)
0.137 81	0.136 40	155.8(69)	151.5(67)

Table 3.1: Properties of the PACS-CS $(2 + 1)$-flavour ensembles [51] used in this work. m_π^{phys} is the mass of the pion with the scale set in the physical limit, while m_π is the same with the scale set on each ensemble individually. Both mass columns carry units of MeV/c^2.

relation. The mass of the $s\bar{s}$ pseudoscalar meson is inferred from the leading linear quark mass dependence of the squared pseudoscalar mass with reference to the physical pion and kaon masses. Both methods produce almost identical hopping parameters, and so we use their average as the hopping parameter for the valence strange quarks, $\kappa_s^{\text{val}} = 0.13665$.

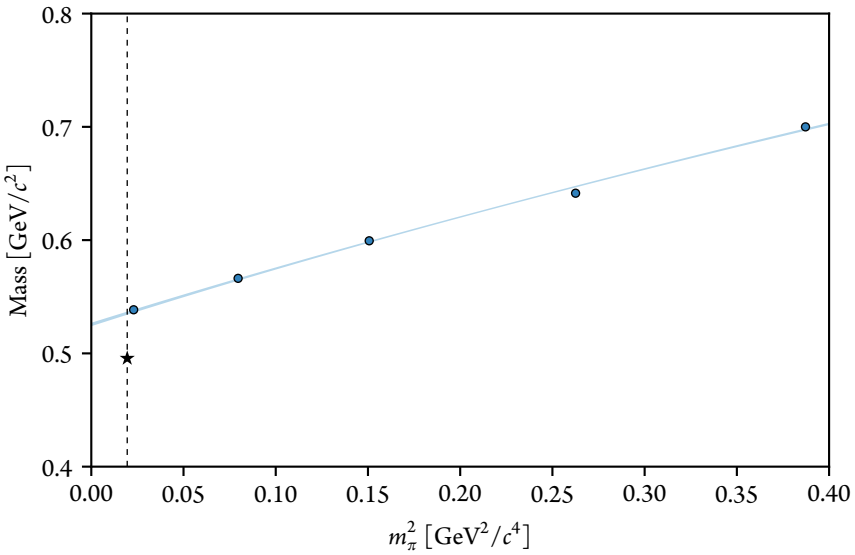

Figure 3.3: The kaon mass plotted against m_π^2 on the PACS-CS ensembles using the results from [51]. The dashed vertical line represents the physical pion mass, and the star on this line indicates the physical kaon mass. The values have been converted into physical units using the Sommer parameter to set the scale. Fitting the lattice results using a model of the form $m_K^2 = \alpha + \beta m_\pi^2$ yields $\alpha = 0.2774(71)$ GeV$^2/c^4$ and $\beta = 0.537(40)$, which produces a mass $42.9(61)$ MeV$/c^2$ too high at the physical pion mass.

✣ Four ✣

Hadronic Observables in Lattice QCD

In any quantum field theory, the information about a system is encoded in the correlation functions corresponding to the observables of interest, and we know from Section 3.3 that we can calculate such quantities on the lattice using the gluon fields and quark propagators. Thus, at this point we need to identify appropriate correlation functions and investigate the relationships between the contained fields.

If we have some quantum system described by the field operator $\chi(x) = \chi(\mathbf{x}, t)$ (an "interpolating" operator for the system), then the time evolution of this system is described by the two-point correlation function

$$G(\mathbf{p}, t) = \sum_{\mathbf{x}} e^{-i\mathbf{p}\cdot\mathbf{x}} \langle \Omega | \chi(\mathbf{x}, t) \overline{\chi}(0, 0) | \Omega \rangle , \tag{4.1}$$

where $\mathbf{p}$ is the momentum of the system, and this gives us insight into the spectrum and dispersive properties of the system. Similarly, if we probe the system at some time $0 < t' < t$ through the operator $\mathcal{O}$, the information is encoded in the three-point correlation function

$$G(\mathbf{p}, \mathbf{p}'; t, t') = \sum_{\mathbf{x}, \mathbf{x}'} e^{-i\mathbf{p}\cdot\mathbf{x}} e^{-i(\mathbf{p}'-\mathbf{p})\cdot\mathbf{x}'} \langle \Omega | \chi(\mathbf{x}, t) \mathcal{O}(\mathbf{x}', t') \overline{\chi}(0, 0) | \Omega \rangle , \tag{4.2}$$

where $\mathbf{p}'$ is the initial momentum (so that the momentum transfer is $\mathbf{q} = \mathbf{p} - \mathbf{p}'$), and this gives us information about the internal structure of the system.

These correlation functions seemingly give us a relatively straightforward method to extract the physical properties of a system. However, in practice, this is not necessarily the case. For example, the interpolating operator χ will, in general, couple to all eigenstates with the same quantum numbers; it is not, a priori, possible to construct an operator for a specific eigenstate. Thus, if we are interested in a specific state (such as in this work), we need a way of isolating its contribution.

For that matter, taking a step back from the correlation functions, there are an infinite number of interpolating operators that will couple to the system of interest – the only requirement is that they have the correct quantum numbers and are gauge invariant. The

former condition is needed so that they actually couple to the system, while the latter is equivalent to requiring them to produce colour-singlet objects, with no colour degrees of freedom.

If we consider a baryon as a local system of three quarks, the most general form for an interpolating field is a linear combination of terms of the form

$$\varepsilon^{abc}(q_a^{a\mathrm{T}}(x)C\Gamma_1 q_\beta^b(x))\Gamma_2 q_\gamma^c(x), \tag{4.3}$$

where $q_a^a(x)$ is the quark field for flavour a and carrying colour a, C is the charge conjugation matrix, and Γ_1 and Γ_2 are combinations of γ matrices that mix the fermion spins to produce a system of the appropriate J^{PC}.

Of course, as we discussed in Section 2.3, there is experimental evidence for states in the hadronic spectrum that cannot be described by the simple, three-quark structures that Equation (4.3) produces. As a result, to fully explore the hadron spectrum, more exotic interpolating operators may be needed, such as a "penta-quark" operator with the form $qqqq\overline{q}$ [66].

However, calculations involving these more exotic operators generally require substantially more computational investment, and so in this work we limit our scope to the local, three-quark interpolating operators. Since we are not using the quenched approximation, we still capture some of this exotic structure through the dynamical generation of quark-antiquark pairs. As we will see later, this is sufficient for our purposes.

4.1 Correlation Functions at the Quark Level

4.1.1 Two-Point Correlation Functions

To investigate the relationship between the fields in the two-point correlation function, we begin by inserting the general form of our interpolating field (Equation (4.3)) into the expression for two-point correlation function (Equation (4.1)):

$$G(\mathbf{p},t) = \varepsilon^{abc}\varepsilon^{a'b'c'}\sum_{\mathbf{x}} \mathrm{e}^{-\mathrm{i}\mathbf{p}\cdot\mathbf{x}}\langle\Omega|(q_a^{a\mathrm{T}}(x)C\Gamma_1 q_\beta^b(x))\Gamma_2 q_\gamma^c(x) \overline{q}_{\gamma'}^{c'}(0)\overline{\Gamma}'_2(\overline{q}_{\beta'}^{b'}(0)\overline{\Gamma}'_1\overline{C}\overline{q}_{a'}^{a'\mathrm{T}}(0))|\Omega\rangle. \tag{4.4}$$

Here, we have permitted different interpolating operators at the source and sink, as indicated by the Greek indices denoting the quark flavour quantum numbers. A prime on an index or object indicates that it belongs to the source interpolating operator.

Performing all possible Wick contractions leads to the result

$$G(\mathbf{p},t) = \varepsilon^{abc}\varepsilon^{a'b'c'}\sum_{\mathbf{x}} \mathrm{e}^{-\mathrm{i}\mathbf{p}\cdot\mathbf{x}}\left(A^{abc}_{a'b'c'} + B^{abc}_{a'b'c'} + C^{abc}_{a'b'c'} + D^{abc}_{a'b'c'} + E^{abc}_{a'b'c'} + F^{abc}_{a'b'c'}\right) \tag{4.5}$$

where

$$A^{abc}_{a'b'c'}(x) = \Gamma_2\, S^{cc'}_{\gamma\gamma'}(x,0)\,\overline{\Gamma}'_2\,\mathrm{tr}\left(\Gamma_1\, S^{bb'}_{\beta\beta'}(x,0)\,\overline{\Gamma}'_1\,(S^{aa'}_{aa'}(x,0))^{\mathrm{T}}\right)\delta_{aa'}\delta_{\beta\beta'}\delta_{\gamma\gamma'}, \tag{4.6}$$

$$B^{abc}_{a'b'c'}(x) = \Gamma_2\, S^{cc'}_{\gamma\gamma'}(x,0)\,\overline{\Gamma}'_2\,\mathrm{tr}\left(\Gamma_1^{\mathrm{T}}\, S^{ab'}_{a\beta'}(x,0)\,\overline{\Gamma}'_1\,(S^{ba'}_{\beta a'}(x,0))^{\mathrm{T}}\right)\delta_{a\beta'}\delta_{\beta a'}\delta_{\gamma\gamma'}, \tag{4.7}$$

$$C^{abc}_{a'b'c'}(x) = \Gamma_2\, S^{cb'}_{\gamma\beta'}(x,0)\,\overline{\Gamma}'_1\,(S^{ba'}_{\beta a'}(x,0))^{\mathrm{T}}\,\Gamma_1^{\mathrm{T}}\,S^{ac'}_{a\gamma'}(x,0)\,\overline{\Gamma}'_2\,\delta_{\gamma\beta'}\delta_{\beta a'}\delta_{a\gamma'}, \tag{4.8}$$

$$D^{abc}_{a'b'c'}(x) = \Gamma_2\, S^{cb'}_{\gamma\beta'}(x,0)\,\overline{\Gamma}'_1\,(S^{aa'}_{aa'}(x,0))^{\mathrm{T}}\,\Gamma'_1\,S^{bc'}_{\beta\gamma'}(x,0)\,\overline{\Gamma}'_2\,\delta_{\gamma\beta'}\delta_{aa'}\delta_{\beta\gamma'}, \tag{4.9}$$

$$E^{abc}_{a'b'c'}(x) = \Gamma_2\, S^{ca'}_{\gamma a'}(x,0)\,\overline{\Gamma}'^{\mathrm{T}}_1\,(S^{bb'}_{\beta\beta'}(x,0))^{\mathrm{T}}\,\Gamma_1^{\mathrm{T}}\,S^{ac'}_{a\gamma'}(x,0)\,\overline{\Gamma}'_2\,\delta_{\gamma a'}\delta_{\beta\beta'}\delta_{a\gamma'}, \text{ and} \tag{4.10}$$

$$F^{abc}_{a'b'c'}(x) = \Gamma_2\, S^{ca'}_{\gamma a'}(x,0)\,\overline{\Gamma}'^{\mathrm{T}}_1\,(S^{ab'}_{a\beta'}(x,0))^{\mathrm{T}}\,\Gamma_1\,S^{bc'}_{\beta\gamma'}(x,0)\,\overline{\Gamma}'_2\,\delta_{\gamma a'}\delta_{a\beta'}\delta_{\beta\gamma'}. \tag{4.11}$$

This is the most general form for a two-point correlation function formed from three-quark interpolating fields of the form given in Equation (4.3). The terminating flavour-space Kronecker deltas act to select the appropriate terms based on the quark flavours of the interpolating operator; in many cases a number of these terms will vanish due to mismatched quark flavours. Moreover, this expression is now just a product of γ matrices and quark propagators, and so is readily and inexpensively evaluated.

4.1.2 Three-Point Correlation Functions

As in the previous section, we can begin an analysis of the three-point correlation function by inserting the definitions of the interpolating operators (Equation (4.3)) and current vertex operator (Equation (3.35)) into the expression for the three-point correlation function (Equation (4.2)):

$$G(\mathbf{p},\mathbf{p}';t,t') = \varepsilon^{abc}\varepsilon^{a'b'c'}\sum_{\mathbf{x},\mathbf{x}'}\mathrm{e}^{-\mathrm{i}\mathbf{p}\cdot\mathbf{x}}\mathrm{e}^{-\mathrm{i}(\mathbf{p}'-\mathbf{p})\cdot\mathbf{x}'}\langle\Omega|(q^a_a(x)C\Gamma_1 q^b_\beta(x))\Gamma_2 q^c_\gamma(x)$$
$$\overline{q}^d_\delta(x')\Gamma_{\mathcal{O}}q^d_\delta(x')\overline{q}^{c'}_{\gamma'}(0)\overline{\Gamma}'_2(\overline{q}^{b'}_{\beta'}(0)\overline{\Gamma}'_1\overline{C}\overline{q}^{a'}_{a'}(0))|\Omega\rangle. \tag{4.12}$$

Again, we perform all possible Wick contractions to produce an expression composed of quark propagators and γ matrices, and this leads to two broad classes of terms depending on whether we contract the quark and antiquark fields in the current form with each other, or if we contract them with quark fields from the interpolating operators:

$$G(\mathbf{p},\mathbf{p}';t,t') = \varepsilon^{abc}\varepsilon^{a'b'c'}\sum_{\mathbf{x},\mathbf{x}'}\mathrm{e}^{-\mathrm{i}\mathbf{p}\cdot\mathbf{x}}\mathrm{e}^{-\mathrm{i}(\mathbf{p}'-\mathbf{p})\cdot\mathbf{x}'}\left((G_{\mathrm{vac}})^{abc}_{a'b'c'}(x) + (G_{\mathrm{val}})^{abc}_{a'b'c'}(x)\right). \tag{4.13}$$

The first of these classes produce the same terms as in the two-point correlation function but weighted by an additional trace term:

$$(G_{\mathrm{vac}})^{abc}_{a'b'c'}(x) = \mathrm{tr}(S^{dd}_{\delta\delta}(x',x')\Gamma_{\mathcal{O}})\left(A^{abc}_{a'b'c'} + B^{abc}_{a'b'c'} + C^{abc}_{a'b'c'} + D^{abc}_{a'b'c'} + E^{abc}_{a'b'c'} + F^{abc}_{a'b'c'}\right), \tag{4.14}$$

where the $A^{abc}_{a'b'c'}$ through $F^{abc}_{a'b'c'}$ are as in the previous section. As indicated by the suggestive notation, these terms encode the vacuum contributions to the amplitude; as discussed previously, these require huge statistics to produce a usable signal-to-noise ratio and are beyond the scope of this work, particularly with our focus on excited states.

The second class of terms, G_{val}, encode the contribution from coupling the current with the valence quarks. Again, we have terms of similar form to the two-point correlation function, but this time they are replicated with each flavour quark propagator replaced, in turn, with the corresponding three-point quark propagator:

$$(G_{\text{val}})^{abc}_{a'b'c'}(x) = \left(A^{abc}_{a'b'c'} + B^{abc}_{a'b'c'} + C^{abc}_{a'b'c'} + D^{abc}_{a'b'c'} + E^{abc}_{a'b'c'} + F^{abc}_{a'b'c'}\right)\Big|_{S_{\delta\delta}(x,0)\to S_{\delta\delta}(x,t',0;\mathbf{q})}, \tag{4.15}$$

where $\mathbf{q}$ is the momentum transfer, defined at the start of this chapter.

For both of the classes, we note that there is a simple sum over quark flavour δ – that is, the full three-point correlation function can be split into the contribution of the interaction with each quark flavour in turn. Moreover, since we operate on a per-flavour basis in lattice QCD, we can evaluate these individual flavour contributions (noting, of course, that only their sum is physically observable). This is particularly advantageous when working with neutral hadrons, as we will discover when we consider the three-point correlation function at the hadronic level in Section 4.2.2.

4.2 Correlation Functions at the Hadronic Level

Knowing how to calculate the two- and three-point correlation functions is not particularly useful if we do not know how to extract the physical observables of interest from them. To discover this, we need to consider the structure of the correlation functions at the higher, hadronic level. Here, we take the view that the interpolating operator $\overline{\chi}$ is a creation operation for hadronic states with corresponding quantum numbers, while χ is the corresponding annihilation operator.

4.2.1 Two-Point Correlation Functions: Energy and Mass

In true quantum mechanical spirit, let us begin by inserting a complete set of eigenstates of the Hamiltonian operator between the interpolating operators in the two-point correlation function to give

$$G(\mathbf{p},t) = \sum_{a,\tilde{\mathbf{p}},s}\sum_{\mathbf{x}} \mathrm{e}^{-\mathrm{i}\mathbf{p}\cdot\mathbf{x}} \langle\Omega|\chi(x)|a,\tilde{\mathbf{p}},s\rangle \langle a,\tilde{\mathbf{p}},s|\overline{\chi}(0)|\Omega\rangle . \tag{4.16}$$

Using the Hamiltonian and momentum operators, we can translate the annihilation operator back to the origin using

$$\chi(x) = e^{iHt} e^{-i\mathbf{P}\cdot\mathbf{x}} \chi(0) e^{i\mathbf{P}\cdot\mathbf{x}} e^{iHt}, \tag{4.17}$$

and then our correlation function simplifies into

$$\begin{aligned} G(\mathbf{p}, t) &= \sum_{a,\tilde{\mathbf{p}},s} \sum_{\mathbf{x}} e^{i(\tilde{\mathbf{p}}-\mathbf{p})\cdot\mathbf{x}} e^{-iE_a(\tilde{\mathbf{p}})t} \langle \Omega | \chi(0) | a, \tilde{\mathbf{p}}, s \rangle \langle a, \tilde{\mathbf{p}}, s | \overline{\chi}(0) | \Omega \rangle \\ &= \sum_{a,s} e^{-iE_a(\mathbf{p})t} \langle \Omega | \chi(0) | a, p, s \rangle \langle a, p, s | \overline{\chi}(0) | \Omega \rangle , \end{aligned} \tag{4.18}$$

where $E_a(\mathbf{p})$ is the energy of state a when endowed with three-momentum $\mathbf{p}$, and we made use of the definition of the Kronecker delta to perform the sum over $\tilde{\mathbf{p}}$.

If we move to a Euclidean time formulation, we have

$$G(\mathbf{p}, t) = \sum_{a,s} \sum_{\mathbf{x}} e^{-E_a(\mathbf{p})t} \langle \Omega | \chi(0) | a, p, s \rangle \langle a, p, s | \overline{\chi}(0) | \Omega \rangle . \tag{4.19}$$

Immediately, we see that each term in the sum over states can be decomposed as the product of a decaying exponential factor together with an operator overlap factor describing how the interpolating operator χ couples with state a. Moreover, all of the time dependence is contained within the exponential factor, with the contributions from higher-energy states decaying faster than those of lower-energy states. This immediately leads to the "long-time" approximation

$$\lim_{t\to\infty} G(\mathbf{p}, t) = \sum_{\mathbf{x}} e^{-E_1(\mathbf{p})t} \langle \Omega | \chi(0) | 1, p, s \rangle \langle 1, p, s | \overline{\chi}(0) | \Omega \rangle , \tag{4.20}$$

where 1 denotes the ground state of the system.

Of course, in practice, this is not truly realisable. There is only a finite extent to our space-time lattice, so $t \to \infty$ can only be approximated by ensuring the temporal extent of our lattice is sufficiently large that the approximation is good. Moreover, the signal-to-noise ratio also decays at the same rate as the correlator, and so we need to ensure we have sufficient statistics that we can still resolve a signal at a sufficiently late time. This is not so much of an issue when there is a large energy gap between states, since the decay rate is proportional to energy, however it is especially important when working with a dense spectrum.

Since the interpolating operator is a spinor when investigating baryons, we need to consider separately the positive- (a^+) and negative-parity (a^-) states. If χ transforms under

parity as $\chi \mapsto \gamma_0 \chi$, we can parametrise the operator overlap factor as

$$\langle \Omega | \chi(0) | a^+, p, s \rangle = Z_{a^+}(\mathbf{p}) \sqrt{\frac{m_{a^+}}{E_{a^+}(\mathbf{p})}} u_{m_{a^+}}(p, s) \tag{4.21}$$

$$\langle \Omega | \chi(0) | a^-, p, s \rangle = Z_{a^-}(\mathbf{p}) \sqrt{\frac{m_{a^-}}{E_{a^-}(\mathbf{p})}} \gamma_5 u_{m_{a^-}}(p, s), \tag{4.22}$$

where $u_{m_{a^\pm}}(p, s)$ is a standard Dirac spinor for a fermion of mass $m_{a^\pm}$. Inserting these into the two-point correlation function, we get

$$\begin{aligned} G^+(\mathbf{p}, t) = \sum_{a^+, s} \mathrm{e}^{-E_{a^+}(\mathbf{p})t} Z_{a^+}(\mathbf{p}) \overline{Z}'_{a^+}(\mathbf{p}) \frac{m_{a^+}}{E_{a^+}(\mathbf{p})} u_{m_{a^+}}(p, s) \overline{u}_{m_{a^+}}(p, s) \\ - \sum_{a^-, s} \mathrm{e}^{-\mathrm{i}E_{a^-}(\mathbf{p})t} Z_{a^-}(\mathbf{p}) \overline{Z}'_{a^-}(\mathbf{p}) \frac{m_{a^-}}{E_{a^-}(\mathbf{p})} \gamma_5 u_{m_{a^-}}(p, s) \overline{u}_{m_{a^-}}(p, s) \gamma_5. \end{aligned} \tag{4.23}$$

where the + superscript indicates that it is for an interpolating operator that transforms with positive parity, and the prime-decorated coupling constants correspond to the source operator while the undecorated to the sink operator. We can evaluate the sum over spins directly using

$$\sum_s u_{m_{a^\pm}}(p, s) \overline{u}_{m_{a^\pm}}(p, s) = \frac{\gamma \cdot p \pm m_{a^\pm}}{2 m_{a^\pm}}, \tag{4.24}$$

and this allows us to simplify the two-point correlation function into

$$\begin{aligned} G^+(\mathbf{p}, t) = \sum_{a^+} \frac{\mathrm{e}^{-E_{a^+}(\mathbf{p})t}}{2E_{a^+}(\mathbf{p})} Z_{a^+}(\mathbf{p}) \overline{Z}'_{a^+}(\mathbf{p}) (\gamma \cdot p + m_{a^+}) \\ + \sum_{a^-} \frac{\mathrm{e}^{-E_{a^-}(\mathbf{p})t}}{2E_{a^-}(\mathbf{p})} Z_{a^-}(\mathbf{p}) \overline{Z}'_{a^-}(\mathbf{p}) (\gamma \cdot p - m_{a^-}). \end{aligned} \tag{4.25}$$

Exactly the same process follows for interpolating operators that transform with negative parity, with the only difference being in the relative signs of the mass in the spinor term $(\gamma \cdot p \pm m_{a^-})$. Thus, we can write down a single expression to describe the behaviour of both positive- and negative-parity interpolating operators:

$$\begin{aligned} G^\pm(\mathbf{p}, t) = \sum_{a^+} \frac{\mathrm{e}^{-E_{a^+}(\mathbf{p})t}}{2E_{a^+}(\mathbf{p})} Z_{a^+}(\mathbf{p}) \overline{Z}'_{a^+}(\mathbf{p}) (\gamma \cdot p \pm m_{a^+}) \\ + \sum_{a^-} \frac{\mathrm{e}^{-E_{a^-}(\mathbf{p})t}}{2E_{a^-}(\mathbf{p})} Z_{a^-}(\mathbf{p}) \overline{Z}'_{a^-}(\mathbf{p}) (\gamma \cdot p \mp m_{a^-}). \end{aligned} \tag{4.26}$$

In order to extract useful, scalar quantities from this correlation function, we need to somehow project the spinor matrix structure down a single value; to do this, we take the

trace of the correlation function, multiplied by some projection matrix Γ. We define the projected correlation function by

$$G(\Gamma; \mathbf{p}, t) := \mathrm{tr}(\Gamma G^{\pm}(\mathbf{p}, t))$$

Since we now have a scalar quantity and all of the time dependence is in the exponent of the exponent term, we can take the ratio between distinct times and define the effective energy of the system as

$$E_{\mathrm{eff}}^{\delta t}(\Gamma; \mathbf{p}, t) := \frac{1}{\delta t} \ln \frac{G(\Gamma; \mathbf{p}, t)}{G(\Gamma; \mathbf{p}, t + \delta t)}; \tag{4.27}$$

in the long-time approximation, this allows us to extract the energy of the ground state:

$$E_{\mathrm{eff}}^{\delta t}(\Gamma; \mathbf{p}, t) \overset{t\to\infty}{=} \frac{1}{\delta t} \ln \frac{\mathrm{e}^{-E_a(\mathbf{p})t}}{\mathrm{e}^{-E_a(\mathbf{p})(t+\delta t)}} = E_a(\mathbf{p}). \tag{4.28}$$

In this work, we use $\delta t = 1$, and drop the reference to this from the effective quantities. For sufficiently large times, $E_{\mathrm{eff}}^{\delta t}(\Gamma; \mathbf{p}, t)$ will be constant in t (once the contribution from higher-energy states has decayed), at which point a constant fit of the form $E(t) = E$ will produce the energy of the ground state. Importantly, this allows us to extract the mass by considering the zero-momentum case, with the effective mass of the system defined by

$$m_{\mathrm{eff}}(\Gamma; t) := E_{\mathrm{eff}}(\Gamma; 0, t) \overset{\text{large } t}{\simeq} m_1. \tag{4.29}$$

Immediately, we note that the selection $\Gamma = \gamma_0$ removes all of the parity information, and collapses the expression into a single sum over states of both parities, with

$$G^{\pm}(\gamma_0; \mathbf{p}, t) = \sum_a \mathrm{e}^{-E_a(\mathbf{p})t} Z_a(\mathbf{p}) \overline{Z}'_a(\mathbf{p}). \tag{4.30}$$

However, such a choice would lead to significant contamination from opposite-parity states, even in the long-time approximation, since the low-lying states of both parities have similar energies. Instead, we consider the combinations

$$\Gamma^{\pm} = \frac{\gamma_0 \pm \mathbb{I}}{2}; \tag{4.31}$$

applying these projection matrices to the spinor factors in Equation (4.26) gives us

$$\mathrm{tr}(\Gamma^{+}(\gamma \cdot p \pm m_a)) = E_a(\mathbf{p}) \pm m_a, \text{ and} \tag{4.32}$$

$$\mathrm{tr}(\Gamma^{-}(\gamma \cdot p \pm m_a)) = E_a(\mathbf{p}) \mp m_a. \tag{4.33}$$

There are two immediate takeaways. Firstly, at zero momentum, we have completely isolated either the positive- or negative-parity states, and secondly that this is possible using only interpolating operators that transform with positive parity. This is due to the cyclic property of the trace – the extra γ_5 matrices that appear when coupling to opposite-parity states can be cycled around in the trace until they sandwich the projection matrix, at which point we can redefine Γ to absorb them. This is equivalent to the replacement $\Gamma^{\pm} \to \Gamma^{\mp}$.

At non-zero momentum, there is some mixing of the states, with the strength of the contribution of opposite-parity states proportional with the difference between the mass and energy [67]. For small momenta, this difference is small, and the opposite-parity contaminations are negligible.

4.2.2 Three-Point Correlation Functions: Electromagnetic Structure

To investigate the three-point correlation function at the hadronic level, we begin by inserting a complete set of eigenstates on both sides of the current insertion in Equation (4.2) to obtain

$$G(\mathbf{p},\mathbf{p}';t,t') = \sum_{a_1,\tilde{\mathbf{p}}_1,s_1}\sum_{a_2,\tilde{\mathbf{p}}_2,s_2}\sum_{\mathbf{x},\mathbf{x}'} e^{-i\mathbf{p}\cdot\mathbf{x}} e^{-i(\mathbf{p}'-\mathbf{p})\cdot\mathbf{x}'} \langle\Omega|\chi(\mathbf{x},t)|a_2,\tilde{\mathbf{p}}_2,s_2\rangle \\ \langle a_2,\tilde{\mathbf{p}}_2,s_2|\mathcal{O}(\mathbf{x}',t')|a_1,\tilde{\mathbf{p}}_1,s_1\rangle \langle a_1,\tilde{\mathbf{p}}_1,s_1|\overline{\chi}(0,0)|\Omega\rangle . \quad (4.34)$$

We can again use the Hamiltonian and momentum operators to translate the operators back to the origin, and so, moving to Euclidean time, we have

$$G(\mathbf{p},\mathbf{p}';t,t') = \sum_{a_1,a_2}\sum_{s_1,s_2} e^{-E_{a_2}(\mathbf{p})(t-t')} e^{-E_{a_1}(\mathbf{p}')t'} \langle\Omega|\chi(0)|a_2,\mathbf{p},s_2\rangle \\ \langle a_2,\mathbf{p},s_2|\mathcal{O}(0)|a_1,\mathbf{p}',s_1\rangle \langle a_1,\mathbf{p}',s_1|\overline{\chi}(0)|\Omega\rangle \quad (4.35)$$

There are now two exponential decay factors: the first depends on the temporal separation between the source and the current insertion, $t_{\mathcal{O}} - t_{\text{src}} = t'$, while the second depends on the separation between the current insertion and the sink, $t_{\text{snk}} - t_{\mathcal{O}} = t - t'$. The rate at which these decays occur may be different if the current insertion causes a state transition (so that $a_2 \neq a_1$).

All of the information about the interaction between the hadron and the current is encoded within the matrix element $\langle a_2,\mathbf{p},s_2|\mathcal{O}(0)|a_1,\mathbf{p}',s_1\rangle$. As in the two-point case, the exponential decay factors suppress excited state contributions relative to the ground state in the large time limit, however in order to use the sequential source technique to construct the three-point propagators we needed to fix the current insertion time t'. As such, we need

to select an appropriate t' so that there is sufficient time for the ground state to dominate in each decay window (before and after the current insertion) while retaining sufficient signal-to-noise ratio that the correlation function is actually usable.

As in the case for the two-point correlation function, we need to project the spinor matrix structure down to a useful scalar quantity. We again do this by taking the trace with an appropriate projection matrix,

$$G(\Gamma; \mathbf{p}, \mathbf{p}'; t, t') \coloneqq \mathrm{tr}(\Gamma G(\mathbf{p}, \mathbf{p}'; t, t')). \tag{4.36}$$

In this work, we are interested in the electromagnetic current; being a vector quantity, our three-point correlation function actually carries a Lorentz index μ, and so we make the replacement $G(\Gamma; \mathbf{p}, \mathbf{p}'; t, t') \to G^{\mu}(\Gamma; \mathbf{p}, \mathbf{p}'; t, t')$. A common parametrisation of the matrix element in Euclidean space for such a current is

$$\langle \mathbf{p}, s_2 | \mathcal{O}^{\mu} | \mathbf{p}', s_1 \rangle = \sqrt{\frac{m^2}{E(\mathbf{p})E(\mathbf{p}')}} \overline{u}_m(\mathbf{p}, s_2) \left(\gamma^{\mu} F_1(Q^2) + \frac{\mathrm{i}\sigma^{\mu\nu} q^{\nu}}{2m_1} F_2(Q^2) \right) u(\mathbf{p}', s_1), \tag{4.37}$$

where F_1 and F_2 are the Dirac and Pauli form factors and $Q^2 = (\mathbf{p} - \mathbf{p}')^2$ is the momentum transfer. Using this together with the forms of the operator overlap factors from Equations (4.21) and (4.22) we can write the projected three-point correlation function as

$$\begin{aligned} G^{\mu}(\Gamma; \mathbf{p}, \mathbf{p}'; t, t') \overset{\text{large } t}{\simeq} & \frac{Z_1(\mathbf{p}) \overline{Z}_1'(\mathbf{p}')}{4E_1(\mathbf{p}) E_1(\mathbf{p}')} \mathrm{e}^{-E_1(\mathbf{p})(t-t')} \mathrm{e}^{-E_1(\mathbf{p}')t'} \\ & \mathrm{tr}\left(\Gamma(\gamma \cdot p \pm m_1) \left(\gamma^{\mu} F_1(Q^2) + \frac{\mathrm{i}\sigma^{\mu\nu} q^{\nu}}{2m_1} F_2(Q^2) \right) (\gamma \cdot p' \pm m_1) \right), \end{aligned} \tag{4.38}$$

where the $\pm$ is selected based on the relative parities of the interpolating operator and the ground state, again indicated by 1; if they transform with the same parity, we use $+$, while if they transform with opposite parities we use $-$.

Let us define $T^{\mu}(\Gamma; \mathbf{q}; \mathbf{p}, \mathbf{p}')$ to be the trace term of the three-point correlator, with

$$T^{\mu}(\Gamma; \mathbf{q}; \mathbf{p}, \mathbf{p}') \coloneqq \mathrm{tr}\left(\Gamma(\gamma \cdot p \pm m_1) \left(\gamma^{\mu} F_1(Q^2) + \frac{\mathrm{i}\sigma^{\mu\nu} q^{\nu}}{2m_1} F_2(Q^2) \right) (\gamma \cdot p' \pm m_1) \right). \tag{4.39}$$

This allows us to write the long-time approximation for the three-point correlation function more succinctly as

$$G^{\mu}(\Gamma; \mathbf{p}, \mathbf{p}'; t, t') \overset{\text{large } t}{\simeq} \frac{Z_1(\mathbf{p}) \overline{Z}_1'(\mathbf{p}')}{4E_1(\mathbf{p}) E_1(\mathbf{p}')} \mathrm{e}^{-E_1(\mathbf{p})(t-t')} \mathrm{e}^{-E_1(\mathbf{p}')t'} T^{\mu}(\Gamma; \mathbf{q}; \mathbf{p}, \mathbf{p}'). \tag{4.40}$$

Since the t' dependence is contained within the exponent of the exponential factor and is antisymmetric with respect to the momentum, we can eliminate it by taking the product

with the initial and final state momenta reversed, to give

$$G^{\mu}(\Gamma;\mathbf{p},\mathbf{p}';t,t')G^{\mu}(\Gamma;\mathbf{p}',\mathbf{p};t,t') \overset{\text{large } t}{\simeq} \frac{Z_1(\mathbf{p})Z_1(\mathbf{p}')\overline{Z}_1'(\mathbf{p})\overline{Z}_1'(\mathbf{p}')}{16E_1(\mathbf{p})^2E_1(\mathbf{p}')^2}\mathrm{e}^{-E_1(\mathbf{p})t}\mathrm{e}^{-E_1(\mathbf{p}')t}T^{\mu}(\Gamma;\mathbf{q};\mathbf{p},\mathbf{p}')T^{\mu}(\Gamma;-\mathbf{q};\mathbf{p}',\mathbf{p}). \quad (4.41)$$

The dependence on t and the coupling factors can be eliminated by dividing by the appropriate-momenta two-point correlation functions, with

$$\frac{G^{\mu}(\Gamma;\mathbf{p},\mathbf{p}';t,t')G^{\mu}(\Gamma;\mathbf{p}',\mathbf{p};t,t')}{G(\Gamma';\mathbf{p},t)G(\Gamma';\mathbf{p}',t)} \overset{\text{large } t}{\simeq} \frac{T^{\mu}(\Gamma;\mathbf{q};\mathbf{p},\mathbf{p}')T^{\mu}(\Gamma;-\mathbf{q};\mathbf{p}',\mathbf{p})}{4E_1(\mathbf{p})E_1(\mathbf{p}')\operatorname{tr}(\Gamma'(\gamma\cdot p \pm m_1))\operatorname{tr}(\Gamma'(\gamma\cdot p' \pm m_1))}. \quad (4.42)$$

where again ± is selected based on the relative parities of the interpolating operator and the ground state.

As in the previous section, we consider the use of $\Gamma' = \Gamma^{\pm}$ based on the parity of the state; then, the trace terms in the denominator can be evaluated using Equations (4.32) and (4.33), and immediately we can construct the ratio

$$R^{\mu}(\Gamma;\mathbf{p},\mathbf{p}';t,t') := \sqrt{\frac{2E_1(\mathbf{p})}{E_1(\mathbf{p})+m_1}\frac{2E_1(\mathbf{p}')}{E_1(\mathbf{p}')+m_1}\frac{G^{\mu}(\Gamma;\mathbf{p},\mathbf{p}';t,t')G^{\mu}(\Gamma;\mathbf{p}',\mathbf{p};t,t')}{G(\Gamma^{\pm};\mathbf{p},t)G(\Gamma^{\pm};\mathbf{p}',t)}} \overset{\text{large } t}{\simeq} \sqrt{T^{\mu}(\Gamma;\mathbf{q};\mathbf{p},\mathbf{p}')T^{\mu}(\Gamma;-\mathbf{q};\mathbf{p}',\mathbf{p})}, \quad (4.43)$$

which contains nothing but the trace terms of Equation (4.39), from which we can extract the various form factors through judicious choices of Γ. Of particular interest in this work are the Sachs electromagnetic form factors, given by

$$\mathcal{G}_{\mathrm{E}}(Q^2) = F_1(Q^2) - \frac{Q^2}{(2m_1)^2}F_2(Q^2) \quad (4.44)$$

$$\mathcal{G}_{\mathrm{M}}(Q^2) = F_1(Q^2) + F_2(Q^2). \quad (4.45)$$

Quickly we can see that we can construct effective functions for these using

$$\mathcal{G}_{\mathrm{E}}^{\mathrm{eff}}(Q^2;t,t') = R^0(\Gamma_j^{\pm};\mathbf{q},0;t,t') \text{ and} \quad (4.46)$$

$$|\varepsilon_{ijk}q^i|\mathcal{G}_{\mathrm{M}}^{\mathrm{eff}}(Q^2;t,t') = (E_1(\mathbf{q})+m_1)R^k(\Gamma_j^{\pm};\mathbf{q},0;t,t'), \quad (4.47)$$

where the projection matrices are

$$\Gamma^{\pm} := \frac{\gamma_0 \pm \mathbb{I}}{2} \quad \text{and} \quad \Gamma_j^{\pm} := \Gamma^{\pm}\gamma_j\gamma_5 = \frac{\gamma_0 \pm \mathbb{I}}{2}\gamma_j\gamma_5, \quad (4.48)$$

and, as with the effective energy function, for sufficiently large t we can fit these with a constant fit model to extract the values for the ground state.

We can get a measure of the physical size of a baryon from its mean-squared charge radius, $\langle r^2 \rangle_{\mathrm{E}}$, which can be calculated through

$$\langle r^2 \rangle_{\mathrm{E}} = -6 \left. \frac{\mathrm{d}\mathcal{G}_{\mathrm{E}}(Q^2)}{\mathrm{d}Q^2} \right|_{Q^2=0}. \tag{4.49}$$

For charged baryons, it is well known that the small-Q^2 dependence of the electromagnetic form factors can be modelled using a dipole ansatz of the form

$$\mathcal{G}_{\mathrm{E}}(Q^2) = \left(\frac{\Lambda^2}{\Lambda^2 + Q^2} \right)^2 \mathcal{G}_{\mathrm{E}}(0), \tag{4.50}$$

where Λ is a constant that characterises the structure of the baryon. This allows us to evaluate the charge radius using

$$\begin{aligned} \langle r^2 \rangle_{\mathrm{E}} &= \frac{12\mathcal{G}_{\mathrm{E}}(0)}{\Lambda} \\ &= \frac{12\mathcal{G}_{\mathrm{E}}(0)}{Q^2} \left(\sqrt{\frac{\mathcal{G}_{\mathrm{E}}(0)}{\mathcal{G}_{\mathrm{E}}(Q^2)}} - 1 \right), \end{aligned} \tag{4.51}$$

where $\mathcal{G}_{\mathrm{E}}(0) = q$ is the charge of the baryon. On the other hand, for neutral baryons we need to be more careful – a dipole ansatz would imply that $\mathcal{G}_{\mathrm{E}}$ is zero for all Q^2. However, as we discovered in Section 4.1.2, we do have access to the contributions from the individual quark sectors through our lattice calculations. Since quarks *are* electrically charged, we can use a dipole ansatz for each quark individually and then sum them (with appropriate charge weightings) to reconstruct the full baryon charge radius, and this procedure is well defined for both the charged and neutral baryons.

Similarly, we can investigate the distribution of spin and angular momentum within a baryon through the evaluation of the magnetic moment $\mu = \mathcal{G}_{\mathrm{M}}(0)$, the magnetic equivalent of the electric charge. If we assume that the magnetic form factor scales the same with Q^2 as the electric form factor, this can be evaluated as

$$\mu = \frac{\mathcal{G}_{\mathrm{M}}(Q^2)}{\mathcal{G}_{\mathrm{E}}(Q^2)}. \tag{4.52}$$

Moreover, again we have access to the individual quark sector contributions through our lattice calculation.

4.3 Variational Analysis of Cross-Correlation Functions

At the beginning of this chapter, we discussed how the two- and three-point correlation functions contain information about all hadronic states with quantum numbers matching those of the interpolating operator. In Section 4.2 we explored using the long-time approximation to extract details about the ground state by waiting long enough that contributions from the higher-energy states have all but disappeared. However, what if we are interested in one of these excited states instead of the ground state? Or, what if the energy difference between the ground and excited states is small enough that there is still a significant contribution from the excited state by the time the statistical noise begins to dominate? In both of these cases, the standard long-time approximation will fail.

Of course, if we had an interpolating operator that only coupled to the state of interest, we could avoid all of these issues and directly evaluate the quantities of interest. However as we discussed previously, it is not possible, a priori, to construct such an operator. The key phrase here is "a priori" – suppose that such an operator φ^a did exist for each state a; we could then write

$$\langle \Omega | \varphi^a | \beta, p, s \rangle = \mathcal{Z}^a(\mathbf{p}) \sqrt{\frac{m_a}{E_a(\mathbf{p})}}\, u_{m_a}(p,s)\, \delta^{a\beta}. \tag{4.53}$$

Moreover, if we have any set $\mathrm{X} = \{ \chi_i \}$ of interpolating operators that spans the operator space, we can use the linearity to also write

$$\varphi^a(x) = \sum_{\chi \in \mathrm{X}} v^a_\chi \chi(x) \quad \text{and} \quad \overline{\varphi}^a(x) = \sum_{\chi \in \mathrm{X}} u^a_\chi \overline{\chi}(x), \tag{4.54}$$

for some real constants v^a_χ and u^a_χ. Equivalently, we can use vector notation to write

$$\varphi^a(x) = \mathbf{v}^a \cdot \boldsymbol{\chi}(x) \quad \text{and} \quad \overline{\varphi}^a(x) = \mathbf{u}^a \cdot \overline{\boldsymbol{\chi}}(x). \tag{4.55}$$

At this point, we note that the "perfect" combination of our basis set of interpolating operators to exactly isolate a particular state will, in general, be momentum dependent. That is, $\mathbf{v}^a \equiv \mathbf{v}^a(\mathbf{p})$ and $\mathbf{u}^a \equiv \mathbf{u}^a(\mathbf{p})$.

Let us now define a Γ-projected two-point correlation matrix by

$$\begin{aligned} \mathbb{G}(\Gamma; \mathbf{p}, t) &= \sum_{\mathbf{x}} \mathrm{e}^{-i\mathbf{p}\cdot\mathbf{x}} \operatorname{tr}\big(\Gamma \langle \Omega | \boldsymbol{\chi}(\mathbf{x}, t) (\overline{\boldsymbol{\chi}}(0,0))^{\mathrm{T}} | \Omega \rangle\big), \\ &= \sum_a \frac{\mathrm{e}^{-E_a(\mathbf{p})t}}{2E_a(\mathbf{p})} \mathbf{Z}^a(\mathbf{p}) (\overline{\mathbf{Z}}^a(\mathbf{p}))^{\mathrm{T}} \operatorname{tr}\big(\Gamma(\gamma \cdot p \pm m_a)\big). \end{aligned} \tag{4.56}$$

The (i,j)-th entry in this matrix is just the Γ-projected two-point correlation function obtained from using χ_i as the sink operator and $\overline{\chi}_j$ as the source operator. Immediately we

note that

$$\begin{aligned}\mathbb{G}(\Gamma;\mathbf{p},t)\,\mathbf{u}^{a}(\mathbf{p}) &= \sum_{\mathbf{x}} \mathrm{e}^{-\mathrm{i}\mathbf{p}\cdot\mathbf{x}}\,\mathrm{tr}\big(\Gamma\,\langle\Omega|\boldsymbol{\chi}(\mathbf{x},t)(\overline{\boldsymbol{\chi}}(0,0))^{\mathrm{T}}|\Omega\rangle\big)\,\mathbf{u}^{a}(\mathbf{p}) \\ &= \sum_{\mathbf{x}} \mathrm{e}^{-\mathrm{i}\mathbf{p}\cdot\mathbf{x}}\,\mathrm{tr}\big(\Gamma\,\langle\Omega|\boldsymbol{\chi}(\mathbf{x},t)\,\overline{\varphi}(0,0)|\Omega\rangle\big)\,\mathbf{u}^{a}(\mathbf{p}) \\ &= \frac{\mathrm{e}^{-E_a(\mathbf{p})t}}{2E_a(\mathbf{p})}\mathbf{Z}^{a}(\mathbf{p})\overline{\mathcal{Z}}^{a}(\mathbf{p})\,\mathrm{tr}\big(\Gamma(\gamma\cdot p \pm m_a)\big),\end{aligned} \tag{4.57}$$

where we have used Equation (4.53) in performing the sum over states. Conveniently, the only state present in this vector of correlation functions is a! We could similarly pre-multiply by $\mathbf{v}^{a\mathrm{T}}$ to obtain

$$\mathbf{v}^{a\mathrm{T}}(\mathbf{p})\,\mathbb{G}(\Gamma;\mathbf{p},t) = \frac{\mathrm{e}^{-E_a(\mathbf{p})t}}{2E_a(\mathbf{p})}\mathcal{Z}^{a}(\mathbf{p})(\overline{\mathbf{Z}}^{a}(\mathbf{p}))^{\mathrm{T}}\,\mathrm{tr}\big(\Gamma(\gamma\cdot p \pm m_a)\big), \tag{4.58}$$

and indeed, performing both the pre- and post-multiplication reduces the result down to a scalar quantity in operator space:

$$\mathbf{v}^{a\mathrm{T}}(\mathbf{p})\,\mathbb{G}(\Gamma;\mathbf{p},t)\,\mathbf{u}^{a}(\mathbf{p}) = \frac{\mathrm{e}^{-E_a(\mathbf{p})t}}{2E_a(\mathbf{p})}\mathcal{Z}^{a}(\mathbf{p})\overline{\mathcal{Z}}^{a}(\mathbf{p})\,\mathrm{tr}\big(\Gamma(\gamma\cdot p \pm m_a)\big). \tag{4.59}$$

The question now is, how can we find the coefficients $\mathbf{u}^{a}$ and $\mathbf{v}^{a}$ that allow us to construct these perfect interpolating operators? With the time dependence contained in the exponent of the exponential factors, we can easily construct a recurrence relationship from Equation (4.57) with

$$\begin{aligned}\mathbb{G}(\Gamma;\mathbf{p},t_0+\Delta t)\,\mathbf{u}^{a}(\mathbf{p}) &= \frac{\mathrm{e}^{-E_a(\mathbf{p})(t_0+\Delta t)}}{2E_a(\mathbf{p})}\mathbf{Z}^{a}(\mathbf{p})\overline{\mathcal{Z}}^{a}(\mathbf{p})\,\mathrm{tr}\big(\Gamma(\gamma\cdot p \pm m_a)\big) \\ &= \mathrm{e}^{-E_a(\mathbf{p})\Delta t}\mathbb{G}(\Gamma;\mathbf{p},t_0)\,\mathbf{u}^{a}(\mathbf{p})\end{aligned} \tag{4.60}$$

That is, the coefficient vector $\mathbf{u}^{a}$ is a (right) generalised eigenvector of $\mathbb{G}(\Gamma;\mathbf{p},t_0+\Delta t)$ and $\mathbb{G}(\Gamma;\mathbf{p},t_0)$, with generalised eigenvalue $\mathrm{e}^{-E_a(\mathbf{p})\Delta t}$. Similarly, $\mathbf{v}^{a}$ is a left generalised eigenvector of the same two matrices. Moreover, each solution for the eigenvalue problem will correspond to a different state in the spectrum for this system. This is the variational method for constructing "perfect" interpolating operators, and more details can be found in [68, 69].

Importantly, not only do the coefficient vectors give us the means to write down these perfect interpolating operators, we can also use them to project correlation functions for a single energy eigenstate from our original correlation matrix through

$$G^{a}(\Gamma;\mathbf{p},t) = \mathbf{v}^{a\mathrm{T}}(\mathbf{p})\,\mathbb{G}(\Gamma;\mathbf{p},t)\,\mathbf{u}^{a}(\mathbf{p}), \tag{4.61}$$

where the $\mathbf{u}^a(\mathbf{p})$ and $\mathbf{v}^a(\mathbf{p})$ are calculated using any pair of t_0 and Δt.

Of course, we will never have enough interpolating operators to completely span the operator space; in general, it is infinite dimensional. We can only approximate the full system, and the effect of this will be to introduce contaminations from energy eigenstates outside of the span of our interpolating operators. The size of these contaminations will therefore be dependent on how well we choose our operator basis – specifically, how well it spans the full operator space. We can then make use of the long-time approximation to minimise the excited-state contamination and investigate the properties of each approximately–eigenstate-projected correlation function to ensure they satisfy the single-state property of Equation (4.59).

To solve the generalised eigenvalue problem, we can either pre- or post-multiply (for $\mathbf{u}^a(\mathbf{p})$ and $\mathbf{v}^a(\mathbf{p})$, respectively) both sides by the inverse of $\mathbb{G}(\Gamma;\mathbf{p},t)$ to convert the problem into an ordinary eigenvalue problem, or we can solve the generalised eigenvalue problem directly. Generally, it is preferable to solve the generalised eigenvalue problem directly to avoid any numerical instability from the matrix inversion.

Using these coefficient vectors, we can construct eigenstate-projected three-point correlation functions by applying them to the three-point correlation matrix formed in the same fashion as $\mathbb{G}(\Gamma;\mathbf{p},t)$:

$$\mathbb{G}(\Gamma';\mathbf{p},\mathbf{p}';t,t') = \sum_{a_1,a_2}\sum_{s_1,s_2} \mathrm{e}^{-E_{a_2}(\mathbf{p})(t-t')}\mathrm{e}^{-E_{a_1}(\mathbf{p}')t'}\,\mathrm{tr}\big(\Gamma'\,\langle\Omega|\boldsymbol{\chi}(0)|a_2,\mathbf{p},s_2\rangle\otimes \langle a_2,\mathbf{p},s_2|\mathcal{O}(0)|a_1,\mathbf{p}',s_1\rangle\,\langle a_1,\mathbf{p}',s_1|\overline{\boldsymbol{\chi}}(0)|\Omega\rangle\big), \quad (4.62)$$

It follows that

$$(\mathbf{v}^a(\mathbf{p}))^{\mathrm{T}}\,\mathbb{G}(\Gamma';\mathbf{p},\mathbf{p}';t,t')\,\mathbf{u}^\beta(\mathbf{p}') = \sum_{s_1,s_2} \mathrm{e}^{-E_a(\mathbf{p})(t-t')}\mathrm{e}^{-E_\beta(\mathbf{p}')t'} \mathrm{tr}\big(\Gamma'\,\langle\Omega|\varphi^a(0)|a,\mathbf{p},s_2\rangle\,\langle a,\mathbf{p},s_2|\mathcal{O}(0)|\beta,\mathbf{p}',s_1\rangle\,\langle\beta,\mathbf{p}',s_1|\varphi^\beta(0)|\Omega\rangle\big), \quad (4.63)$$

where care has been taken to ensure the coefficient vectors used on each side match the incoming and outgoing momenta, respectively.

4.4 Improvements to the Variational Method

In order to make use of, for example, the jackknife resampling method discussed in Section 3.3.4, we need to ensure that we compare the same quantity on each of the sub-ensembles. This includes the solutions to the generalised eigenvalue problem used in the variational method, and so we need to identify a suitable method to associate the solutions across sub-ensembles. The obvious choice is to order the solutions based on the eigenvalue, however this presupposes that the ordering of the energies is the same across all

sub-ensembles; in the case of near-degenerate states, this may not be the case, and so such an approach would be prone to misidentification.

The eigenvectors, on the other hand, provide a distinct and unique "fingerprint" for each state, but to use this we need to define a suitable measure that allows us to compare eigenvectors between sub-ensembles. The inner product seems like the obvious choice, since it provides a measure of the overlap between two vectors, with a pair of eigenvectors from different sub-ensembles referring to the same state if they have maximal inner product. However, the lack of orthogonality in our basis for the operator space means this too would be prone to misidentification; since the basis vectors are not orthogonal, it is possible for an eigenvector to have large overlap with multiple eigenvectors from another sub-ensemble. Moreover, since our original interpolating operators are not normalised with respect to their overlap with the energy eigenstates, it is possible for a few (or even one) operator to dominate, again leading to misidentification.

To correct for the lack of orthogonality in the operator basis, we first note that in the ensemble average the two-point correlation matrix is Hermitian. As such, we can create an improved, unbiased estimator for the correlation matrix using

$$\tilde{\mathbb{G}}(\Gamma;\mathbf{p},t) = \frac{\mathbb{G}(\Gamma;\mathbf{p},t) + \mathbb{G}^\dagger(\Gamma;\mathbf{p},t)}{2}. \tag{4.64}$$

Not only is this matrix then Hermitian, but its columns will be linearly independent if (and only if) the interpolating operators used in its construction are also linearly independent. In this case, $\tilde{\mathbb{G}}(\Gamma;\mathbf{p},t)$ will be positive definite, and it immediately follows that the $\mathbf{u}^\alpha(\mathbf{p})$ and $\mathbf{v}^\alpha(\mathbf{p})$ will be $\tilde{\mathbb{G}}(\Gamma;\mathbf{p},t_0)$-orthogonal – that is,

$$\mathbf{v}^{\alpha\dagger}(\mathbf{p})\tilde{\mathbb{G}}(\Gamma;\mathbf{p},t_0)\mathbf{v}^\beta(\mathbf{p}) = 0, \tag{4.65}$$

for $\alpha \neq \beta$ (and similarly for $\mathbf{u}(\mathbf{p})$). Moreover, $\tilde{\mathbb{G}}(\Gamma;\mathbf{p},t)$ permits a Hermitian, positive-definite principal square root, $\tilde{\mathbb{G}}^{1/2}(\Gamma;\mathbf{p},t)$, and so this orthogonality relation can be written as

$$\begin{aligned} 0 &= \mathbf{v}^{\alpha\dagger}(\mathbf{p})\tilde{\mathbb{G}}^{1/2}(\Gamma;\mathbf{p},t_0)\tilde{\mathbb{G}}^{-1/2}(\Gamma;\mathbf{p},t_0)\tilde{\mathbb{G}}(\Gamma;\mathbf{p},t_0)\tilde{\mathbb{G}}^{-1/2}(\Gamma;\mathbf{p},t_0)\tilde{\mathbb{G}}^{1/2}(\Gamma;\mathbf{p},t_0)\mathbf{v}^\beta(\mathbf{p}) \\ &= \mathbf{v}^{\alpha\dagger}(\mathbf{p})\tilde{\mathbb{G}}^{1/2}(\Gamma;\mathbf{p},t_0)\tilde{\mathbb{G}}^{1/2}(\Gamma;\mathbf{p},t_0)\mathbf{v}^\beta(\mathbf{p}). \end{aligned} \tag{4.66}$$

That is, the vectors $\mathbf{w}^\alpha(\mathbf{p}) := \tilde{\mathbb{G}}^{1/2}(\Gamma;\mathbf{p},t_0)\mathbf{v}^\beta(\mathbf{p})$ are orthogonal.

Of course, this is just an orthogonality relation between vectors obtained from the same correlation matrix. It will only approximately hold when comparing vectors obtained from different correlation matrices. Since jackknife subensembles are all estimators for the same ensemble average, the subspaces spanned by the interpolating operators are generally sufficiently similar that this approximate orthogonality is enough to identify corresponding eigenstates. On the other hand, the subspace spanned can vary quite dramatically with

changes in momentum; an attempt to compare the eigenvectors obtained at a zero momentum with those at a large momentum is likely to fail. However, as long as one can take sufficiently-small steps through increasing momentum, it is possible to track the flow as far as one needs.

To correct for the poor normalisation, we note that

$$[\mathbb{G}(\Gamma;\mathbf{p},0)]_{ii} = \sum_a |Z_i^a(\mathbf{p})|^2 \operatorname{tr}(\Gamma(\gamma\cdot p \pm m_a)), \tag{4.67}$$

provides a measure of the relative strength of the two-point correlation function formed using χ_i at the source and sink. Using this, we can construct "normalised" interpolating operators $\hat{\chi}_i = \chi_1/\sqrt{[\mathbb{G}(\Gamma;\mathbf{p},0)]_{ii}}$, and then construct a "normalised" correlation matrix using these through

$$[\hat{\mathbb{G}}(\Gamma;\mathbf{p},t)]_{ij} = \frac{[\mathbb{G}(\Gamma;\mathbf{p},t)]_{ij}}{\sqrt{[\mathbb{G}(\Gamma;\mathbf{p},0)]_{ii}[\mathbb{G}(\Gamma;\mathbf{p},0)]_{jj}}}. \tag{4.68}$$

The elements of this matrix are $\mathcal{O}(1)$ at $t = 0$, with equality on the diagonal.

It is important to note that this is not a true norm, due to the cross-terms arising from the sum over all states in Equation (4.67), and that the poor normalisation will progressively return as we move away from $t = 0$. As such, we want to perform this normalisation procedure as close as possible to the start time t_0 used in the variational analysis. Fortunately, since the exponential decay provides a recurrence relation between successive times, we can equivalently normalise at any $t > 0$ – including at $t = t_0$.

To use the eigenvectors calculated using the normalised two-point correlation matrix to eigenstate-project the three-point correlation matrix, we need to use the same normalised interpolating operators. However, this is equivalent to pre- and post-multiplying the original three-point correlation matrix by the the same factors as in Equation (4.68), but again ensuring that the correct momenta are used:

$$[\hat{\mathbb{G}}(\Gamma';\mathbf{p},\mathbf{p}';t,t')]_{ij} = \frac{[\mathbb{G}(\Gamma';\mathbf{p},\mathbf{p}';t,t']_{ij}}{\sqrt{[\mathbb{G}(\Gamma;\mathbf{p},t_0)]_{ii}[\mathbb{G}(\Gamma;\mathbf{p}',t_0)]_{jj}}}. \tag{4.69}$$

4.5 Smearing the Operator Basis

As we noted when discussing the variational method, key to the success of the technique is the identification of a set of interpolating operators that have good overlap with the states of interest while spanning enough of the operator space to minimise contaminations. Up until this point, however, the only interpolating operators that we have discussed are those

of the form given in Equation (4.3). A set of such operators is, in general, very limited in size – for example, for the nucleon, there are only three linearly independent operators:

$$\chi_{\Gamma_1,\Gamma_2}(x) = \varepsilon^{abc}(u^{a\mathrm{T}}(x)C\,\Gamma_1 d^b(x))\Gamma_2 u^c(x), \tag{4.70}$$

for $(\Gamma_1, \Gamma_2) \in \{(\gamma_5, \mathbb{I}), (\mathbb{I}, \gamma_5), (\gamma_5\gamma_0, \mathbb{I})\}$. Moreover, as we noted in that discussion, this is the most general form for a local, three-quark interpolating operator – the only way to expand the operator basis is to relax one of the two conditions: the locality of the operator or the number of valence quarks.

Increasing the number of valence quarks would allow us to construct multi-particle interpolating operators, but as we noted previously this generally leads to a substantial increase in the required computation investment, and so is beyond the scope of this work. Instead, we focus on relaxing the locality of the operators in this work, and indeed, this makes sense from a physical perspective – one would generally expect at least some spatial distribution of the quarks within a hadron. There are two popular methods for allowing such a structure: displaced operators and smeared operators.

The former of these methods begins by replacing some of the local quark fields in Equation (4.3) with spatially-displaced quark fields $\psi_i(x) = U_i(x)\psi(x + a\hat{\mu})$, and then using the Clebsch-Gordon coefficients to construct linear combinations with the correct quantum numbers [70–72]. However, the reduced symmetry on the lattice means that distinct J^{PC}, corresponding to the infinite tower of irreducible representations of $\mathrm{O}(3)$, get mixed into the finite number of irreducible representations of O_h, and therefore care must be taken to separate these out. Moreover, such operators require propagator inversions for each source orientation, and as in the case of using higher–quark-count operators this quickly adds to the computational investment.

The latter approach begins by noting that our choice of a delta function for the source and sink field operators is not particularly physically realistic. We generally expect the wave function to have some extended, spherically-symmetric distribution about the origin, and so we look to recreate such a structure to use for our field operators. The prescription is to take our delta function operator and "smear" it in the spatial directions by including contributions from neighbouring sites; by applying this smearing multiple times, we can effectively control the width of the operator.

In this work, we use gauge-invariant Gaussian smearing [73]. We start with a delta function centred at $x = z$, $\eta^0(x) = \delta(z - x)$ and iteratively construct smeared operators through

$$\eta^i(x) = \sum_{\mathbf{y}} F(x,y)\eta^{i-1}(y), \tag{4.71}$$

where

$$F(x,y) := (1-\alpha)\delta(x,y) + \frac{\alpha}{6}\sum_{\mu=1}^{3}(U_\mu(x)\delta(x + a\hat{\mu}, y) + U^\dagger(x - a\hat{\mu})\delta(x - a\hat{\mu}, y)) \tag{4.72}$$

and a is a constant that controls the strength of the smearing.

For the source operator, this amounts to the replacement of the source vector $\eta^0(x)$ in Equation (3.33) with the smeared version $\eta^n(x)$ for some n and a and solving for this new, smeared propagator. Moreover, solving for the smeared propagator will have similar convergence properties as for the point source, and there is no appreciable increase in computational cost!

On the sink side, using a smeared operator is straightforward because the expression for the correlation functions already includes a sum over the sink location. The evaluation of a smeared sink operator merely involves the replacement of the corresponding propagators in Equation (4.5) with those constructed through the same iterative process as for the operator itself:

$$S^{n,ab}_{a\beta}(x,0) = \sum_{\mathbf{y}} F(x,y) S^{n-1,ab}_{a\beta}(y,0). \tag{4.73}$$

Again, there is no appreciable increase in the computational cost.

For a given unsmeared interpolating operator χ^0, a linear combination of smeared interpolating operators χ^n across various values for n would be expected to have spherical nodes. This would suggest that such an operator would have large overlap with radial excitations, and such is shown for the Roper resonance in [74].

✣ Five ✣

Isolating the Λ(1405)

The results presented in this chapter were originally published in Physical Review Letters [75] along with several supporting conference proceedings [76–78]. Our presentation here is adapted from these manuscripts, but also includes minor improvements to the techniques and improved statistics.

Following on from the CSSM Lattice Collaboration's recent work in developing an effective technique for investigating the low-lying odd-parity nucleon spectrum [18], it is natural to consider its application to other hadron spectra. Given the success of the technique in identifying the nearly-degenerate $\mathrm{N}^*(1535)$ and $\mathrm{N}^*(1650)$, can it also be used to resolve the low-lying $\Lambda(1405)$ that otherwise always appears high in lattice calculations? In the nucleon study, significant chiral curvature was observed in the dependence on quark mass, especially for the $\mathrm{N}^*(1650)$ – only by moving close to the physical point can this lattice state be identified with its physical counterpart. With this in mind, we use the same techniques and ensembles here to investigate the negative-parity, spin-1/2 spectrum of the Λ.

The variational analysis, described in Section 4.3 takes advantage of the extra information found by calculating cross-correlation functions for different operators at the source and sink to isolate individual states [79, 80]. Such an analysis is necessary as the lowest three $J^P = 1/2^-$ states in this channel all lie within a 400 MeV range, at $1405.1^{+1.3}_{-1.0}$ MeV/c^2, 1670 ± 10 MeV/c^2, and 1800^{+50}_{-80} MeV/c^2 [6]. Because SU(3)-flavour symmetry is broken by the heavier strange quark mass, all three of these states will survive until the signal is buried in noise, and so the long-time approximation usually used to extract ground-states will only be able to resolve a mixture of these low-lying states. To expand our operator basis beyond that provided by the usual flavour and Dirac structures, we employ gauge-invariant Gaussian smearing, described in Section 4.5, at both the source and sink.

In comparison to the odd-parity N^* resonances, where significant finite-size effects develop through avoided level crossings between the baryon and the multi-particle scattering states, the odd-parity $\Lambda(1405)$ is relatively independent of the box size. For example, using the $\overline{\mathrm{K}}\mathrm{N}$ Jülich model of hadron exchange [81, 82], the lowest multi-particle scattering states, $\pi\Sigma$ and $\overline{\mathrm{K}}\mathrm{N}$ in the $I = 0$, $S = -1$, $J^P = 1/2^-$, lie, respectively, below and above the $\Lambda(1405)$, and do not cross for lattices with $m_\pi L \in [1.7, 3.5]$ [83]. As such, we expect the finite-size effects to be small in this analysis.

5.1 Interpolating Operators for the Λ Baryon

Given that the Λ baryon lies in the centre of approximate SU(3)-flavour, there are a variety of interpolating operators that will couple to it. These correspond not only to the usual various Dirac structures, but also to the different possible flavour-symmetry structures. If we consider a flavour-octet structure, the operators have the form [84]

$$\chi_i^8(x) = \frac{1}{\sqrt{6}}\varepsilon_{abc}\Big(2\,(u_a^{\mathrm{T}}(x)CA_id_b(x))\,B_is_c(x) + (u_a^{\mathrm{T}}(x)CA_is_b(x))\,B_id_c(x) - (d_a^{\mathrm{T}}(x)CA_is_b(x))\,B_iu_c(x)\Big), \quad (5.1)$$

while if we consider a flavour-singlet structure, the operators have the form

$$\chi_i^1(x) = -2\varepsilon_{abc}\Big(-(u_a^{\mathrm{T}}(x)CA_id_b(x))\,B_is_c(x) + (u_a^{\mathrm{T}}(x)CA_is_b(x))\,B_id_c(x) - (d_a^{\mathrm{T}}(x)CA_is_b(x))\,B_iu_c(x)\Big), \quad (5.2)$$

where the $i \in \{1, 2\}$ suffix enumerates the potential Dirac structures, with

$$(A_1, B_1) = (\gamma_5, \mathbb{I}) \quad \text{and} \quad (A_2, B_2) = (\mathbb{I}, \gamma_5). \quad (5.3)$$

However, due to the inherent symmetry in the flavour-singlet structure, we note that the two Dirac structures are related through a Fierz identity, and so we relabel this operator as the unsuffixed $\chi^1 := \chi_1^1$.

Using the terms common to these two flavour structures, we can also construct the so-called "common" operators

$$\chi_i^c(x) = \frac{1}{\sqrt{2}}\varepsilon_{abc}\Big((u_a^{\mathrm{T}}(x)A_is_b(x))\,B_id_c(x) - (d_a^{\mathrm{T}}(x)A_is_b(x))\,B_iu_c(x)\Big). \quad (5.4)$$

These isospin-0 interpolating operators make no assumptions about the SU(3)-flavour symmetry properties, and should couple to all states of the Λ baryon, regardless of their SU(3)-flavour–symmetry structure. By way of analogy with the "common" operators, we name the interpolating operators with specific SU(3)-flavour–symmetry structures (χ_i^1 and χ_i^8) the "flavoured" operators.

In Ref. [85], the low-lying nucleon spectrum is investigated using the same ensembles as in this analysis using a wide range of the Gauge-invariant source- and sink-smearing described in Section 4.5 – from 16 to 1600 sweeps, which corresponds to RMS radii of between 0.20 and 16.00 (in lattice units). There they found that both small and large numbers of sweeps were beneficial in spanning the operator space, but that the extremely-high numbers of sweeps produced ill-conditioned correlation matrices, and so settled on using $\{16, 35, 100, 200\}$ sweeps with $\alpha = 0.7$. As this basis spans the space well, we apply it to the negative-parity Λ sector.

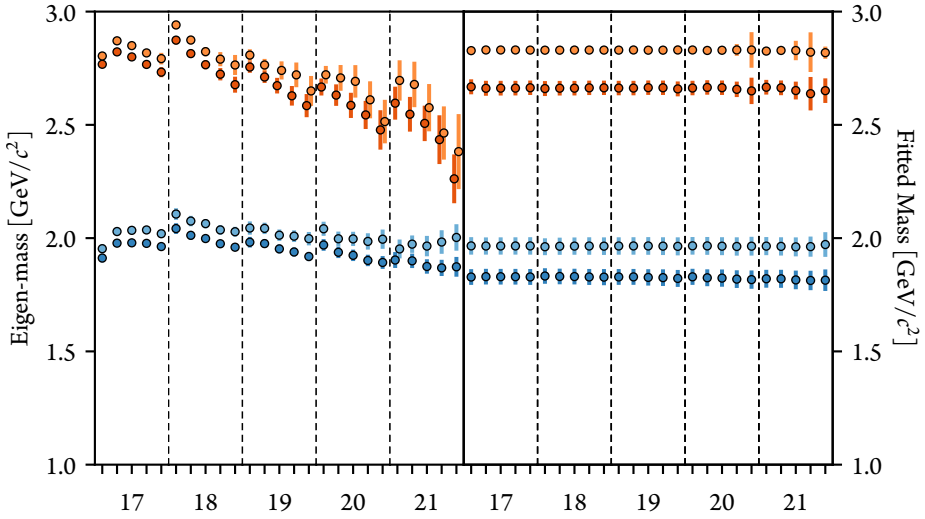

Figure 5.1: Comparison of the masses extracted from (left) the eigenvalues of Equation (4.60) (the "eigenmass") and (right) fitting the projected effective mass derived from the projected correlation function of Equation (4.61) on the ensemble with $\kappa_{u,d} = 0.13700$ for $t_0 \in \{ 17, \ldots, 21 \}$ and $\Delta t \in \{ 1, \ldots, 5 \}$. Numbers of the abscissa indicate t_0 with Δt increasing within each t_0.

5.2 Exploring the Variational Parameters

We begin our analysis of the negative-parity Λ by investigating the dependence of the spectrum on variational parameters t_0 and Δt. Since, in this work, we insert our hadron source at $t = t_{src} = 16$, let us consider the range $t_0 \in \{ 17, \ldots, 21 \}$ and $\Delta t \in \{ 1, \ldots, 5 \}$. For this initial exploration, we use the operator basis formed from the two "common" interpolating operators of Equation (5.4) together with 16 and 100 sweeps of gauge-invariant Gaussian smearing.

In Section 4.3, we discussed two methods for determining the mass of a state identified through a variational analysis – we can either invoke the long-time approximation and fit the projected effective mass, or we can extract it from the eigenvalue of the generalised eigenvalue problem. We call this latter mass the "eigenmass" of the state. Plots of the masses found using both these methods for the ensemble with $\kappa_{u,d} = 0.13700$ are presented in Figure 5.1, and for the other ensembles in Appendix A. The eigenmasses suggest the four states are split into two groups of two states each.

By selecting variational parameters too soon after the introduction of the source, there is too much contamination from higher-mass states for the variational analysis to completely isolate the low-lying states. As a result, the eigenmass shows a large dependence

on variational parameters for small t_0 and Δt. On the other hand, if we wait too long to perform the variational analysis then the noise begins to dominate and we are left with large errors on the eigenmasses and poor fits.

The fits to the projected effective masses are relatively stable across the variational parameters, especially at small t_0 and Δt. This is because the eigenvectors have a relatively weak dependence on the parameters t_0 and Δt. Moreover, the contamination from higher-mass states affecting the eigenmasses can be (mostly) removed by fitting at later times through the standard long-time approximation (at the expense of increased errors). At large values of t_0 and Δt, the ground-state plateau (of each projected effective mass) is so overshadowed by the noise it cannot be reliably fitted.

In order to proceed with our analyses, we select the variational parameters $(t_0, \Delta t) = (18, 2)$ as representative.

5.3 Exploring the Operator Space

Since the "common" interpolating operators χ_i^c of Equation (5.4) should couple to all states in the Λ channel, we begin our exploration of the operator space with combinations of these and look at the behaviour when we vary the number and amount of smearing included in the operator basis.

Plots of the masses extracted from both the eigenvalues (the "eigenmass") and from fitting the projected effective masses using $(t_0, \Delta t) = (18, 2)$ for the ensemble with $\kappa_{u,d} = 0.13700$ are presented in Figures 5.2 and 5.3 across all combinations of smearings and "common" interpolating operators, and for the other ensembles in Appendix B.

We again note the grouping of states; here, the pattern suggests that the spectrum observed in our analysis consists of n_{sm} groups of n_{op} states, where n_{sm} is the number of smearings included in the operator basis and n_{op} is the number of interpolating operators included. We discussed previously that we expect linear combinations of smeared operators to couple well with radial excitations due to the nodes in the spatial distribution. A natural extension to this is that the members of each group of states correspond to the same radial excitation, with the energy difference within the group due to some broken symmetry (such as SU(6)–spin-flavour).

Both the eigenmasses and fitted projected effective masses show some smearing dependence when only a single smearing level is included in the operator basis. Generally speaking, larger amounts of smearing produce more stable (and lower) spectra, with the exception of 200 sweeps on its own (and to a lesser extent, the combination of 100 and 200 sweeps).

On their own, both of the "common" interpolating operators produce fits of approximately the same mass, with that produced by χ_1^c lying slightly below that of χ_2^c (however

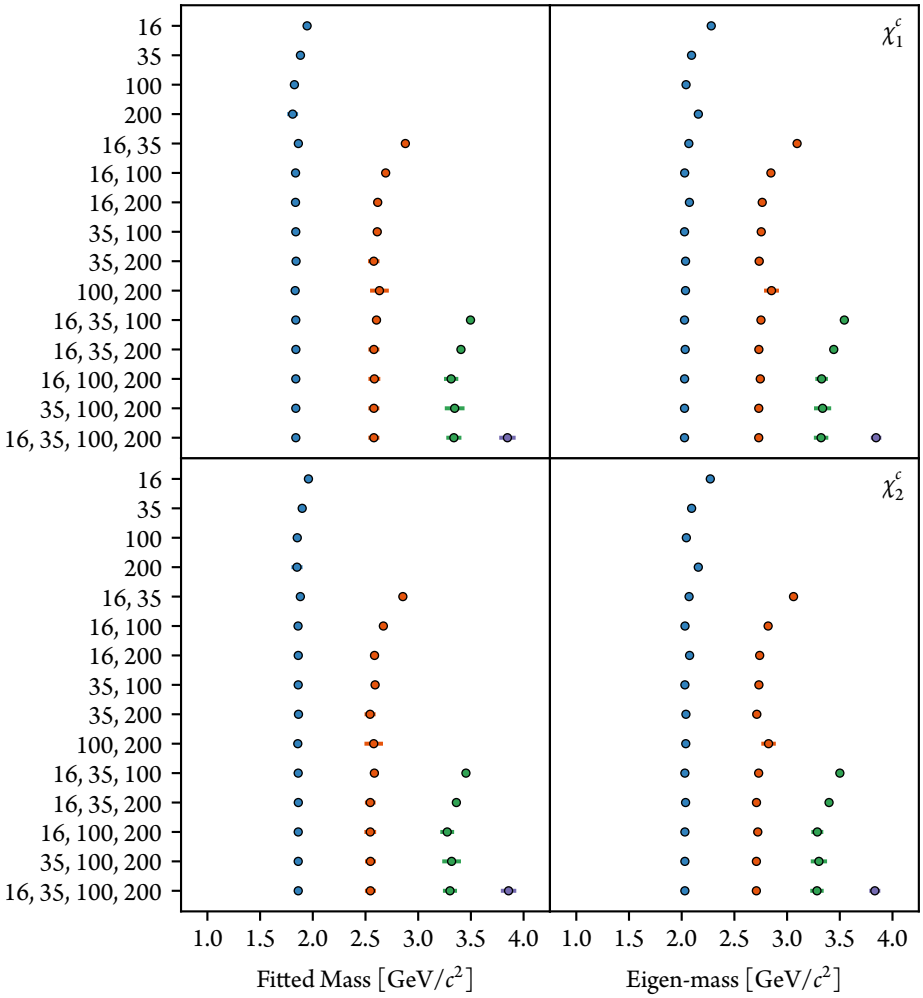

Figure 5.2: Comparison of the masses extracted from fitting the projected effective mass (left) and from the eigenvalues (right) on the ensemble with $\kappa_{u,d} = 0.13700$ across all combinations of smearing levels using a single "common" interpolating operator.

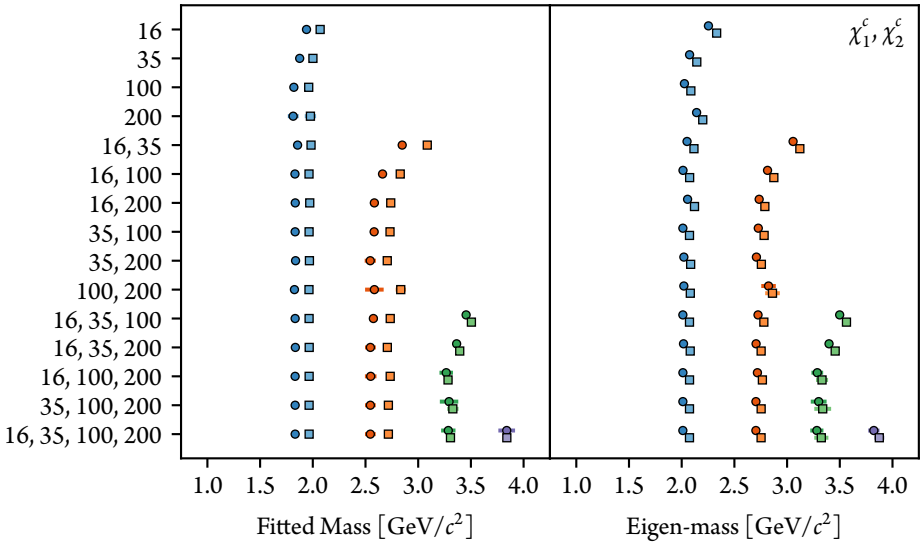

Figure 5.3: Comparison of the masses extracted from fitting the projected effective mass (left) and from the eigenvalues (right) on the ensemble with $\kappa_{u,d} = 0.13700$ across all combinations of smearing levels using both "common" interpolating operators.

this is not a statistically significant effect). However, by including both interpolating operators in a correlation matrix analysis, we can identify two nearby states, with the lower lying slightly below that produced by either of the operators individually, and the higher lying slightly above. This suggests that we were only able to isolate a mixture of these two states when using only a single interpolating operator.

Moreover, in the physical spectrum there are three low lying states – using just the "common" interpolating operators has only allowed for the identification of two states. So far we have observed that the number of states in each group follows the number of interpolating operators. Thus, a reasonable assumption is that there is also another state in the lattice spectrum but that we have not included enough interpolating operators to isolate them all. Instead our pair of isolated states is still just a pair of mixtures. Fortunately, we still have some unused interpolating operators – the "flavoured" operators of Equations (5.1) and (5.2).

Similarly to above, plots of the eigenmasses and fitted effective masses for the ensemble with $\kappa_{u,d} = 0.13700$ are included in Figures 5.4 to 5.6, and for the other ensembles in Appendix B. The pattern of states again appears as n_{sm} groups of n_{op} states – that is, we now see three low-lying states, as in the physical spectrum. The dependence of the spectrum on the smearing included in the operator basis is the same as for the "common" interpolating operators.

That we see the same number of low-lying states here as in the physical spectrum may be a consequence of using three different local interpolating operators in the correlation-matrix analysis. In actually predicting the number of low-lying states, it would be preferable to consider additional spin-flavour structures and perhaps non-local operators containing derivatives. While we identified five interpolating operators in Section 5.1, we cannot combine these in an expanded variational analysis as the correlation matrix becomes singular, indicating the additional interpolating operators do not span the space in a sufficiently unique manner.

We note that there is very little change in the quality of the fits, as represented by the reduced χ^2, upon adding the second and third interpolating operators that enable the isolation of a second and third state in each group, as demonstrated in Figure 5.7. This is due to the dominance of the first interpolating field considered in creating the lowest-lying state; the contribution from the second and third operators introduces a minor correction to the correlator without significantly influencing the quality of the fit. However, there is a cumulative effect as the correlation matrix increases in size, and the onset of plateau behaviour in the projected correlators improves significantly. This is particularly important for the study of the electromagnetic form factors, where the electromagnetic current is inserted as early as possible in Euclidean time to ensure good signal in the form factor measurements.

There is also a minor but consistent improvement in the relative error of the fitted mass for the lowest-lying state as additional interpolating operators are introduced into the operator basis. This is despite the actual mass decreasing slightly, which would otherwise naturally lead to an *increase* in the relative error. This can be attributed to the earlier onset of the plateau in the effective mass, since this permits fits starting at earlier Euclidean times where there is less statistical error.

We need to ensure that we have a sufficiently large basis to minimise contamination from higher-energy states; to ensure this, we aim to isolate two states above the states of interest. In order to satisfy this aim for the lowest group of states we need to include at least three levels of smearing. For the lowest-lying states there is statistically no difference between all operator bases that include at least three levels of smearing. As such, we adopt the basis containing all three flavoured interpolating operators at 16, 100, and 200 sweeps of smearing for the remainder of this work (with an exception for Section 5.5 where we also consider 16, 35, and 200 sweeps to ensure there is no manifest difference in the flavour structure).

5.4 Investigating the Quark Mass Dependence

To determine if our approach can isolate the otherwise-elusive $\Lambda(1405)$, we need to consider how the spectrum depends on the quark mass; only by approaching the physical

quark masses can we draw a conclusion on this. To this end, we consider the dependence on the square of the pion mass as a proxy for the quark mass – through the Gell-Mann–Oakes–Renner relation we have $m_\pi^2 \propto m_q$ at leading order in the chiral expansion [86]. In Figure 5.8 we present the dependence of the spectrum on the square of the pion mass using both "common" interpolating operators, while in Figure 5.10 we present the same using all three "flavoured" operators. Figures 5.9 and 5.11 present the same but restricted to the low-lying states.

As we move towards the physical point, while the lowest-lying state does trend towards the physical value for the $\Lambda(1405)$, it remains high. Moreover, the level ordering with respect to the nearby multi-particle scattering states is wrong. This is despite the expectation that the finite-size effects will be small. However, we do note that the second lattice state reproduces the physical value for third physical state, and this again suggests that the lowest-lying lattice state for this operator basis is a mixture, of the lowest two physical states.

On the other hand, as we discussed previously, the use of the "flavoured" operators allows us isolate all three low-lying states as demonstrated in Figures 5.10 and 5.11. Now we can also reproduce the correct level ordering on our lightest ensemble. Moreover, the mass on the lightest ensemble is consistent with the physical $\Lambda(1405)$. We include a tabulation of these values in Table 5.1.

We also observe that the masses of the low-lying states experience significant jumps near the infinite-volume scattering thresholds, likely through avoided level crossings. On the lattice these scattering thresholds are basis states that get mixed in the finite volume to form energy-eigenstates.

Using the "common" interpolating operators, we obtain a value of $1.534(46)\ \mathrm{GeV}/c^2$ at the lightest quark mass, still above that of the $\Lambda(1405)$. Indeed, this value is very near the average of the two lowest-lying physical states. We also still have the problem of the missing state, and so we must conclude that using the "common" interpolating operators cannot cleanly resolve the low-lying $J^P = 1/2^-$ sector for the Λ baryon.

For the "flavoured" operators, the values obtained on this lightest ensemble are consistent with the physical masses of the Λ spectrum. We have successfully isolated the $\Lambda(1405)$ for the first time in lattice QCD. In Table 5.2 we present a comparison between the physical masses for the lightest $J^P = 1/2^-$ Λ states in nature with the values obtained on the lightest ensemble (with $\kappa_{\mathrm{ud}} = 0.13781$) from the "flavoured" analysis. Since there are currently only these three energy eigenstates in the experimentally-observed physical spec-

Figure 5.4: *(facing page)* Comparison of the masses extracted from fitting the projected effective mass (left) and from the eigenvalues (right) on the ensemble with $\kappa_{\mathrm{u,d}} = 0.13700$ across all combinations of smearing levels using a single "flavoured" interpolating operator.

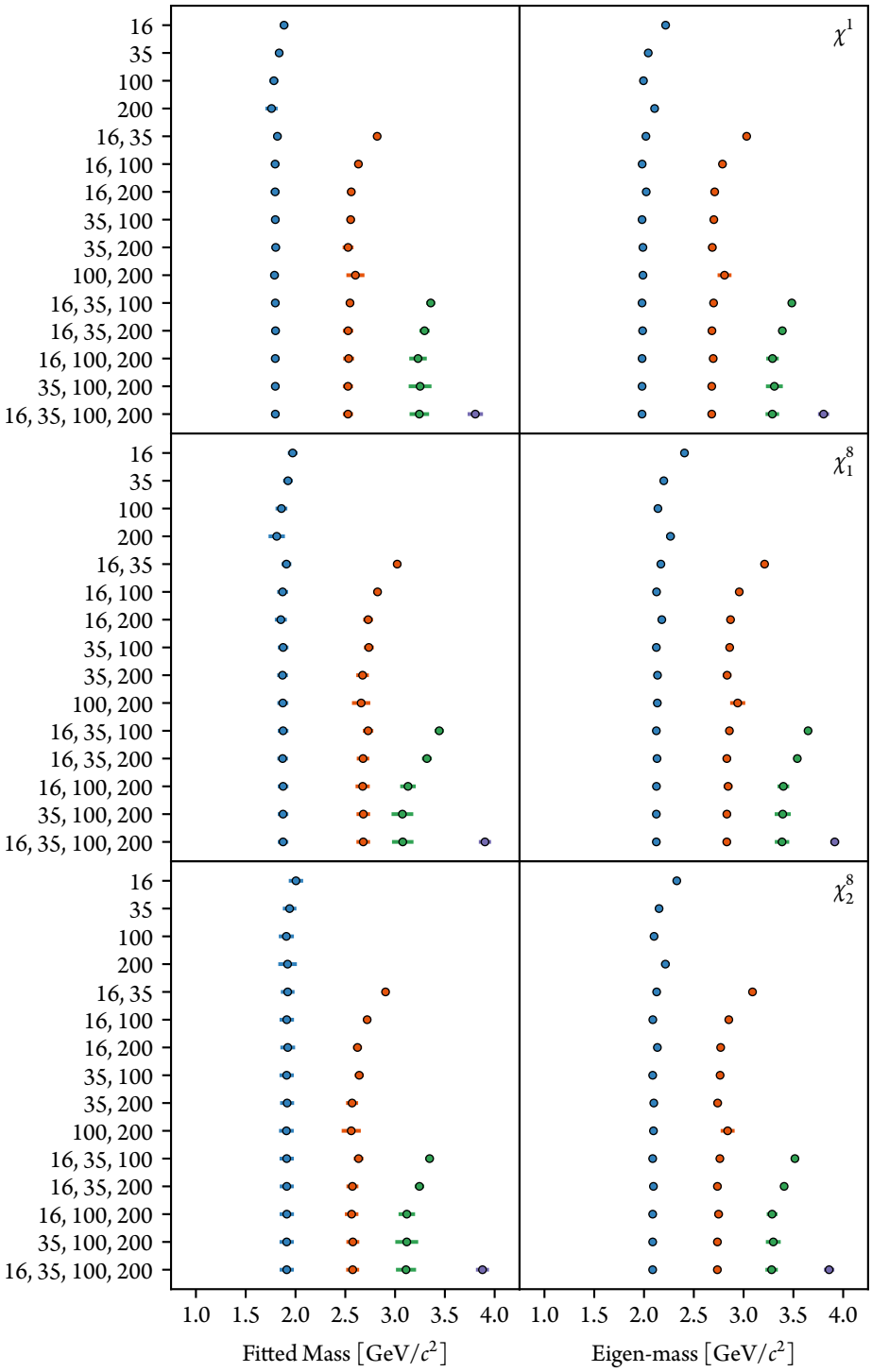
16
35
100
200
16, 35
16, 100
16, 200
35, 100
35, 200
100, 200
16, 35, 100
16, 35, 200
16, 100, 200
35, 100, 200
16, 35, 100, 200
χ^1
χ_1^8
χ_2^8
1.0 1.5 2.0 2.5 3.0 3.5 4.0
Fitted Mass [GeV/c^2]
Eigen-mass [GeV/c^2]

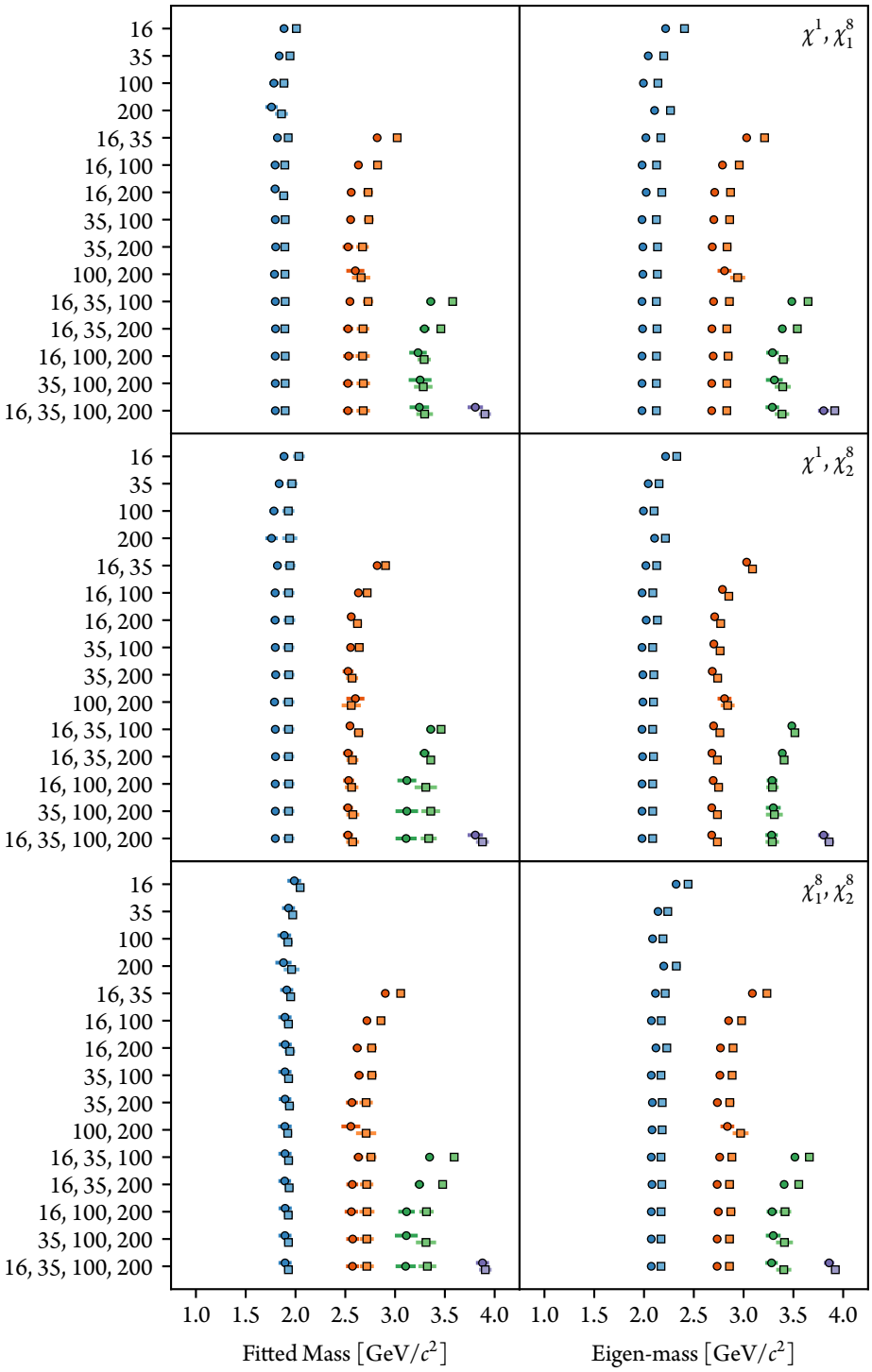
16
35
100
200
16, 35
16, 100
16, 200
35, 100
35, 200
100, 200
16, 35, 100
16, 35, 200
16, 100, 200
35, 100, 200
16, 35, 100, 200
χ^1, χ_1^8
χ^1, χ_2^8
χ_1^8, χ_2^8
1.0 1.5 2.0 2.5 3.0 3.5 4.0
Fitted Mass [GeV/c^2]
Eigen-mass [GeV/c^2]

Figure 5.5: *(facing page)* Comparison of the masses extracted from fitting the projected effective mass (left) and from the eigenvalues (right) on the ensemble with $\kappa_{u,d} = 0.13700$ across all combinations of smearing levels using two of the three "flavoured" interpolating operators.

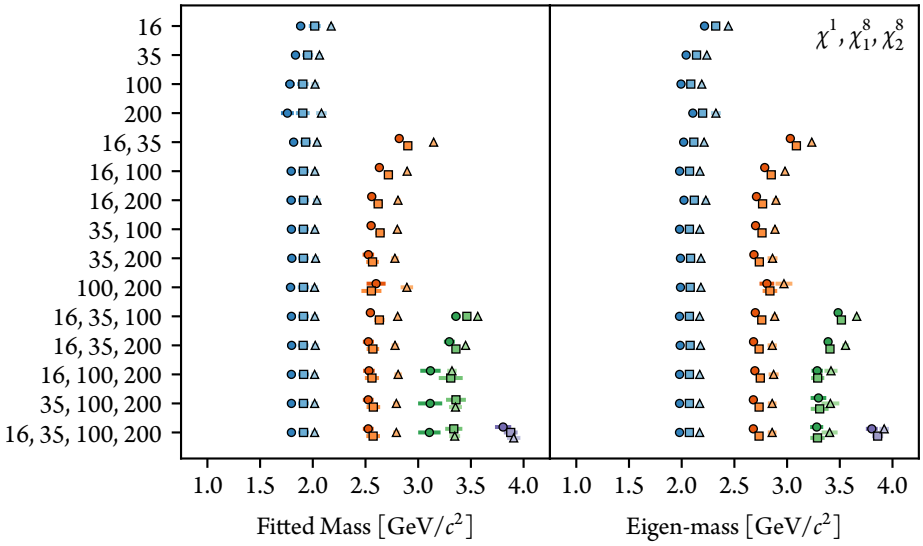

Figure 5.6: Comparison of the masses extracted from fitting the projected effective mass (left) and from the eigenvalues (right) on the ensemble with $\kappa_{u,d} = 0.13700$ across all combinations of smearing levels using all three "flavoured" interpolating operators.

trum, it's not possible to compare the higher-energy states resolved in our analysis with those in nature.

In [87], we develop a simple model using Hamiltonian effective field theory focussing on the flavour-singlet couplings to the bare basis state required by the admission of a three-quark configuration carrying the quantum numbers of the $\Lambda(1405)$. This allows us to investigate the finite-volume effects, and a bootstrap analysis in the infinite-volume limit produced a mass of $1.48^{+0.17}_{-0.07}$ GeV/c^2 for the $\Lambda(1405)$. The bootstrap distribution has a very sharp peak at the most probable value of 1.41 GeV/c^2, in good agreement with the experimental value of $1.4051^{+0.0013}_{-0.0010}$ GeV/c^2.

This analysis is extended in [88] to not distinguish between the possible flavour-symmetry structures, and here two complex poles in the scattering amplitude are identified for the $\Lambda(1405)$, the locations of which depend on if a bare baryonic state is included in

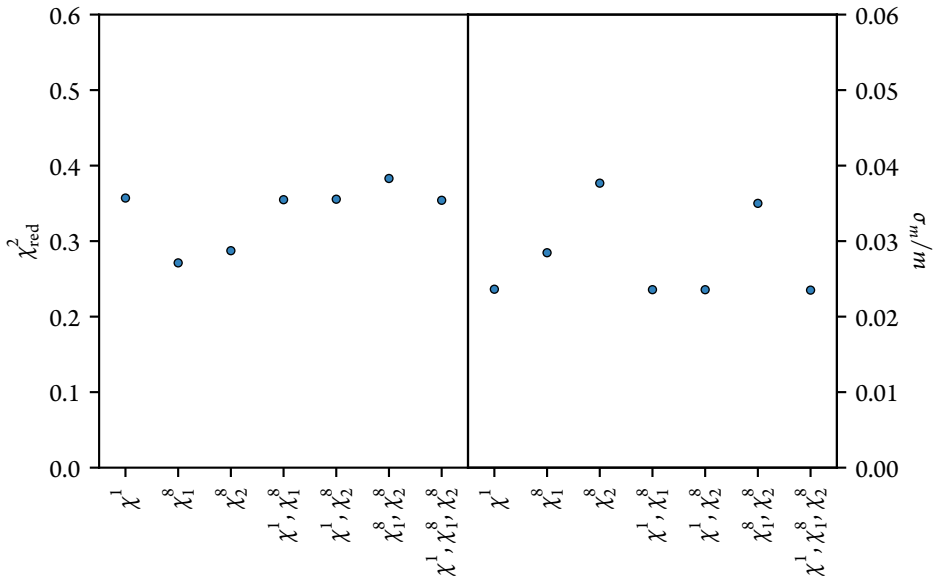

Figure 5.7: Comparison of the quality of the fits to the projected effective mass, as represented by (left) the reduced χ^2 and (right) the relative error in the mass, across the available combinations of "flavoured" interpolating operators on the ensemble with $\kappa_{u,d} = 0.13700$. We selected 16, 100, and 200 sweeps of gauge-invariant Gaussian smearing for all combinations presented here. There is very little variation in these metrics across the combinations, especially when the singlet interpolating operator, χ^1, is included. This is due to the dominance of a singlet flavour structure in the lowest-lying state, which is discussed later in Section 5.5.

the matrix Hamiltonian model[1]. Since the bare state is needed not only to find a candidate for the Λ(1670), but also to obtain an accurate description of our lattice results near the SU(3)-flavour limit, we quote here the two poles for the Λ(1405) when the bare state is included: $(1429 - 22\mathrm{i})\ \mathrm{MeV}/c^2$ and $(1338 - 89\mathrm{i})\ \mathrm{MeV}/c^2$.

5.5 Flavour-Symmetry Structure

The eigenvectors from our variational analysis not only allow us to project correlation functions for pure energy eigenstates, but they can be directly viewed to gain an understanding of each states' structure. In essence, the components of the eigenvector for a particular state

[1]The poles are complex as the Λ(1405) is an unstable resonance in the physical spectrum; the real part describes the location of the corresponding peak in the cross section while the imaginary part describes its width (or equivalently, the decay rate of the resonance).

m_π	m_1	m_2	m_3	m_4	m_5
0.6223(91)	1.797(42)	1.913(52)	2.017(31)	2.533(55)	2.561(67)
0.5124(79)	1.737(46)	1.904(36)	2.112(21)	2.387(75)	2.536(53)
0.3882(55)	1.629(51)	1.844(45)	1.933(18)	2.310(56)	2.565(58)
0.2821(48)	1.645(55)	1.762(61)	1.883(42)	2.579(77)	2.735(57)
0.1515(67)	1.442(50)	1.622(65)	1.867(37)	2.336(90)	2.51(13)

m_π	m_6	m_7	m_8	m_9
0.6223(91)	2.810(34)	3.116(96)	3.31(11)	3.320(45)
0.5124(79)	2.659(30)	3.145(84)	3.176(49)	3.249(27)
0.3882(55)	2.688(35)	3.023(62)	3.258(59)	3.322(32)
0.2821(48)	2.755(30)	3.228(89)	3.325(63)	3.333(26)
0.1515(67)	2.672(47)	3.266(72)	3.51(19)	3.547(55)

Table 5.1: Fits to projected effective masses using "flavoured" interpolating operators for each ensemble considered in this work, thus providing the energy-eigenstate spectrum of $J^P = 1/2^-$ Λ states on our finite volume lattice with $L \sim 3$ fm. All values are in GeV/c^2.

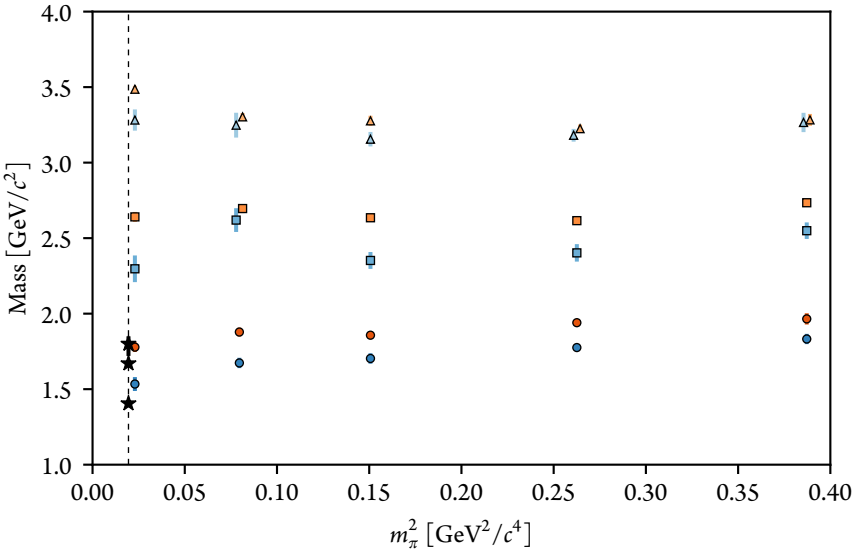

Figure 5.8: Dependence on m_π^2 of the eigenstate-projected masses obtained using the "common" interpolating operators χ_1^c and χ_2^c. The dashed vertical line represents the physical pion mass, and the star-shaped points on this line indicate the masses of the states found in nature. Points have been offset slightly on the m_π^2 axis where needed to avoid collisions and aid viewing; where this occurs, the centre of the group lies as the true value.

state	physical [6]	"flavoured"
Λ(1405)	$1.4051^{+0.0013}_{-0.0010}$	1.442(50)
Λ(1670)	1.670 (10)	1.622(65)
Λ(1800)	$1.800\ ^{+0.050}_{-0.080}$	1.867(37)

Table 5.2: Comparison of the masses of the lowest-lying physical states with those of the lightest group of states the "flavoured" analysis on the lightest ensemble considered. Our lattice QCD investigation has resolved three low-lying energy eigenstates in accordance with nature. All values are in GeV/c^2.

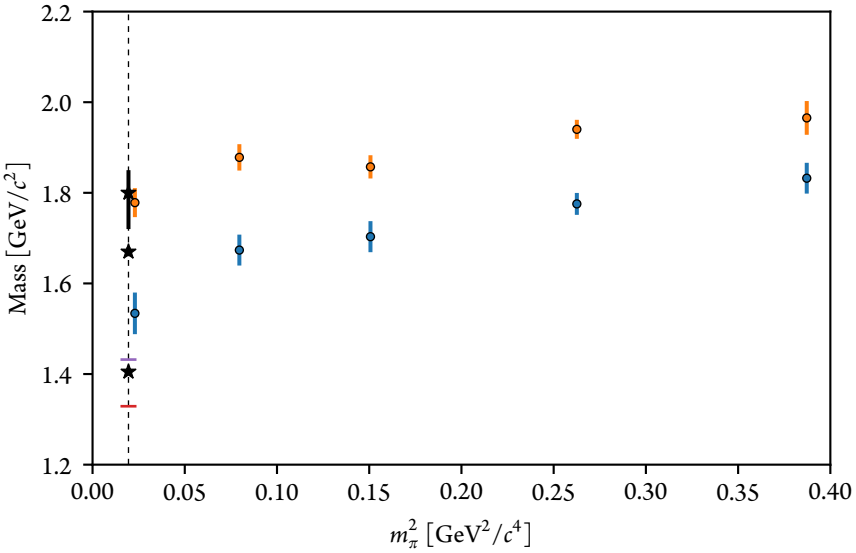

Figure 5.9: As for Figure 5.8, but restricted to the two lowest-lying states. The star-shaped points on this line indicate the masses of the states found in nature while the horizontal bars represent the (red) $\pi\Sigma$ and (purple) $\overline{\mathrm{K}}\mathrm{N}$ infinite-volume scattering thresholds.

describe the importance of each interpolating operator in creating that state; a large eigenvector component suggests that the corresponding operator is important in describing the wave function of that energy eigenstate.

Figures 5.12 and 5.13 plot the absolute value of the components of the right eigenvectors ($\mathbf{u}^a$ of the generalised eigenvalue problem in Equation (4.60)) projecting the three lowest-lying states using the "flavoured" interpolating operators for the two smearing combinations being used in this analysis. The behaviour is the same in both cases – the SU(3)-flavour–singlet operator χ^1 (at all the included smearing levels) is—by far—the predominant contributor to the lowest-lying state. This suggests that this state, which we have identified with the $\Lambda(1405)$, carries a predominant flavour-singlet structure. The other two states are dominated by the SU(3)-flavour–octet operators χ_i^8 of both Dirac structures, with the χ_2^8 being (slightly) favoured for the second state and χ_1^8 for the third.

To further investigate the flavour-symmetry structures, we calculate the lengths of the projections onto the SU(3)-flavour–symmetry–specific subspaces – those spanned by the operators with each flavour symmetry structure. If the component of the (left) eigenvector associated with interpolating operator χ and n sweeps of smearing is u_χ^n, then the length of the projection onto the subspace associated with the operator χ is given by

$$p_\chi := \sum_{n \in S} \left(u_\chi^n\right)^2, \tag{5.5}$$

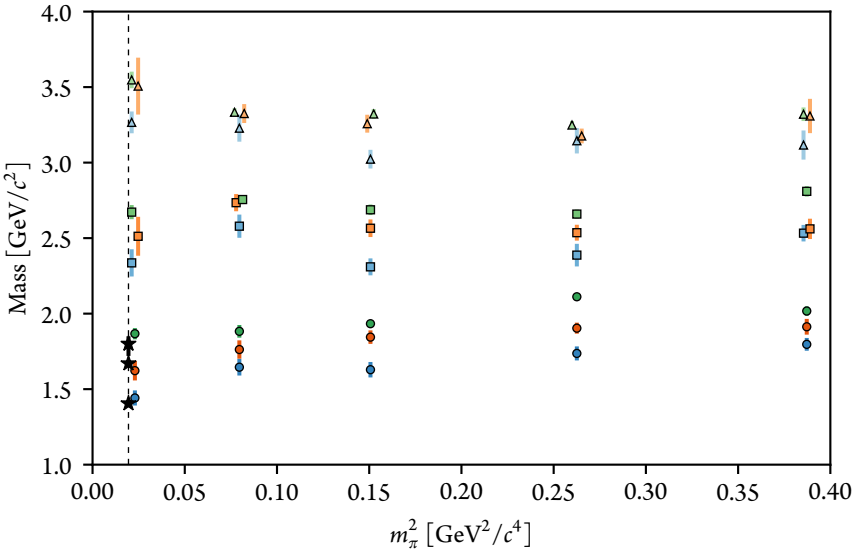

Figure 5.10: Dependence on m_π^2 of the eigenstate-projected masses obtained using the "flavoured" interpolating operators χ^1, χ_1^8, and χ_2^8. The dashed vertical line represents the physical pion mass, and the star-shaped points on this line indicate the masses of the states found in nature. Points have been offset slightly on the m_π^2 axis where needed to avoid collisions and aid viewing; where this occurs, the centre of the group lies as the true value.

where S is the set of smearings included in the variational analysis, and this gives us a quantitative measure of the relative contribution for each interpolating operator. In Figure 5.14 we plot these lengths across our ensembles for both sets of smearings under consideration, and tabulate the results in Table 5.3. We can clearly see the dominance of the flavour-singlet operator χ_1 in the low-lying state. Moreover, that the values are essentially identical in each set of smearings gives confidence that our selection of a specific set of smearings does not manifestly influence the structure of the projected states here – the flavour structure is independent of the smearing basis used.

It is also worth noting that the separation between the flavour-singlet and -octet structured operators is at its most pronounced near the SU(3)-flavour limit, with the contribution from the octet operators near-vanishing for the lowest-lying state, and the singlet operator the same for the other two states. This is expected due to the increasingly-broken SU(3)-flavour–symmetry as we move towards the physical pion mass.

In approaching the physical point, two types of SU(3) symmetry breaking are encountered. The first, discussed above, is the mixing of interpolating operators in the process of isolating the energy eigenstates. The second is the breaking of the interpolating operator symmetry itself due the unique role of the heavier strange quark. Together, these effects

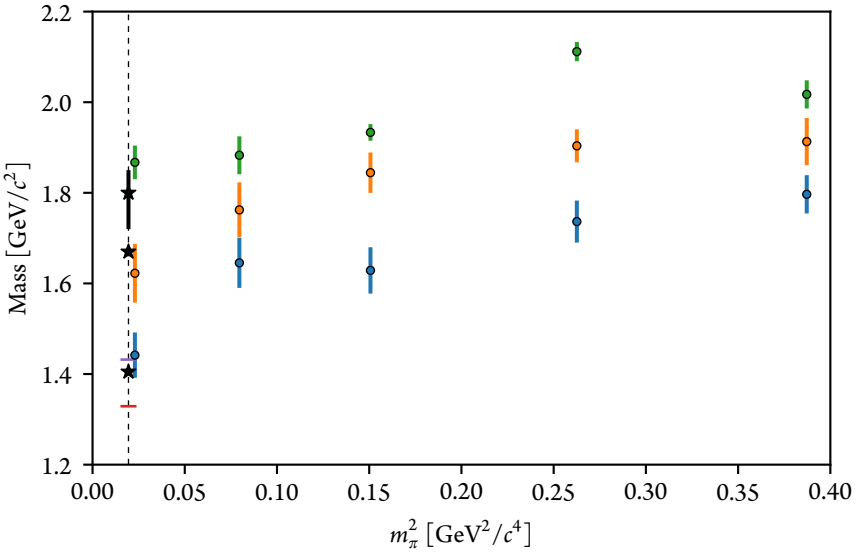

Figure 5.11: As for Figure 5.10, but restricted to the three lowest-lying states. The star-shaped points on this line indicate the masses of the states found in nature while the horizontal bars represent the (red) $\pi\Sigma$ and (purple) $\overline{\mathrm{K}}\mathrm{N}$ infinite-volume scattering thresholds.

give rise to significant flavour symmetry breaking at the physical point.

Figure 5.12: *(facing page)* The components of the left eigenvector projecting the correlation functions associated with the three lowest-lying states using all three "flavoured" interpolating operators and 16, 35, and 200 sweeps of smearing. The lowest-lying state (top plot) is always dominated by the flavour-singlet interpolating operator, with a mild contribution from the flavour-octet operators as we move away from the $SU(3)$-flavour limit. Points have been offset slightly on the m_π^2 axis where needed to avoid collisions and aid viewing; where this occurs, the centre of the group lies as the true value. The legend describing the series has been distributed across all three plots to aid visibility; this combined legend applies to all plots of this Figure.

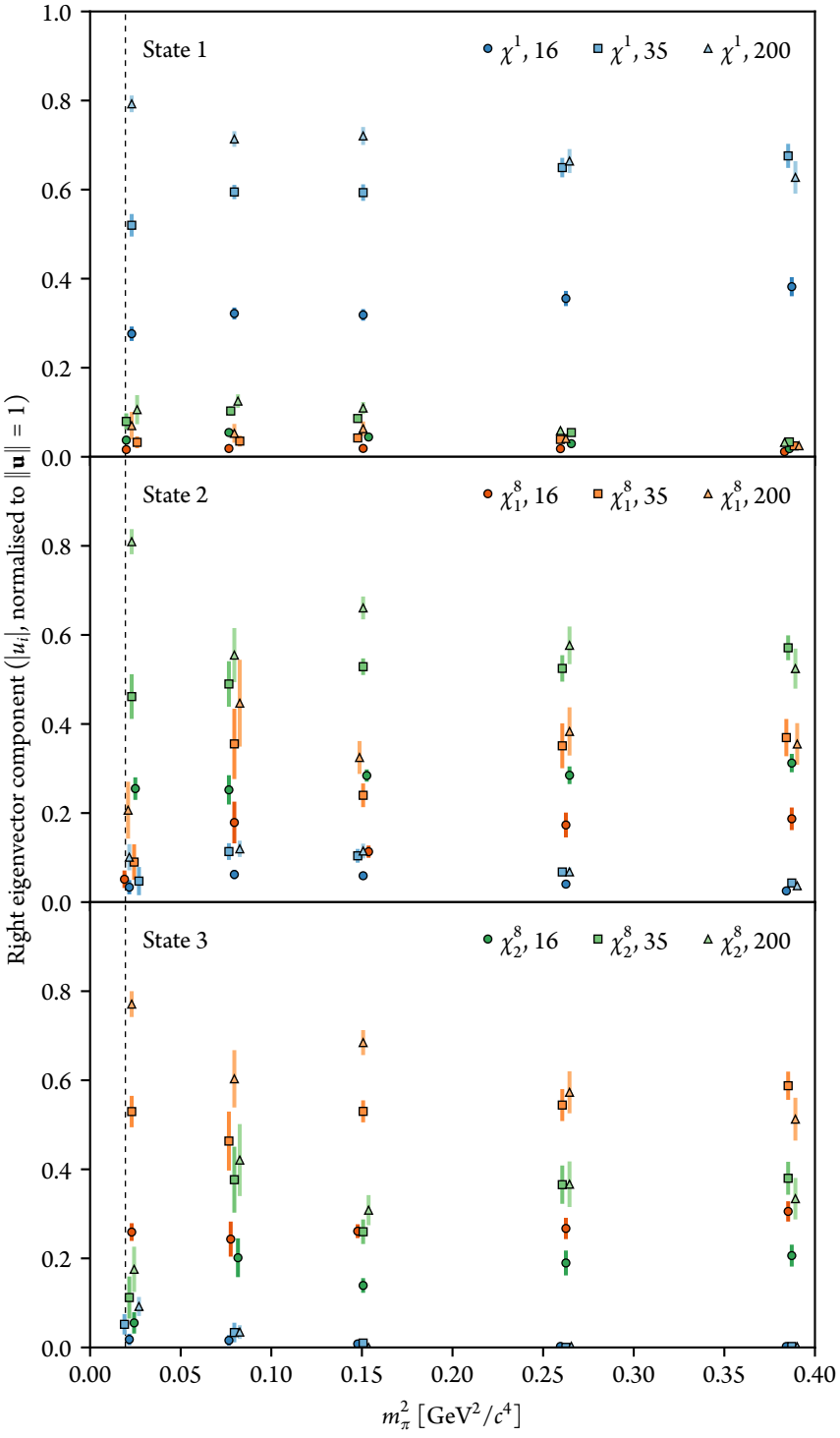
State 1
χ^1, 16
χ^1, 35
χ^1, 200
State 2
χ_1^8, 16
χ_1^8, 35
χ_1^8, 200
State 3
χ_2^8, 16
χ_2^8, 35
χ_2^8, 200
Right eigenvector component ($|u_i|$, normalised to $\|\mathbf{u}\| = 1$)
m_π^2 [GeV$^2/c^4$]
0.0
0.2
0.4
0.6
0.8
1.0
0.00
0.05
0.10
0.15
0.20
0.25
0.30
0.35
0.40

Figure 5.13: *(facing page)* As for Figure 5.12, but using 16, 100, and 200 sweeps of smearing. Again, the lowest-lying state (top plot) is always dominated by the flavour-singlet interpolating operator, with a mild contribution from the flavour-octet operators as we move away from the SU(3)-flavour limit.

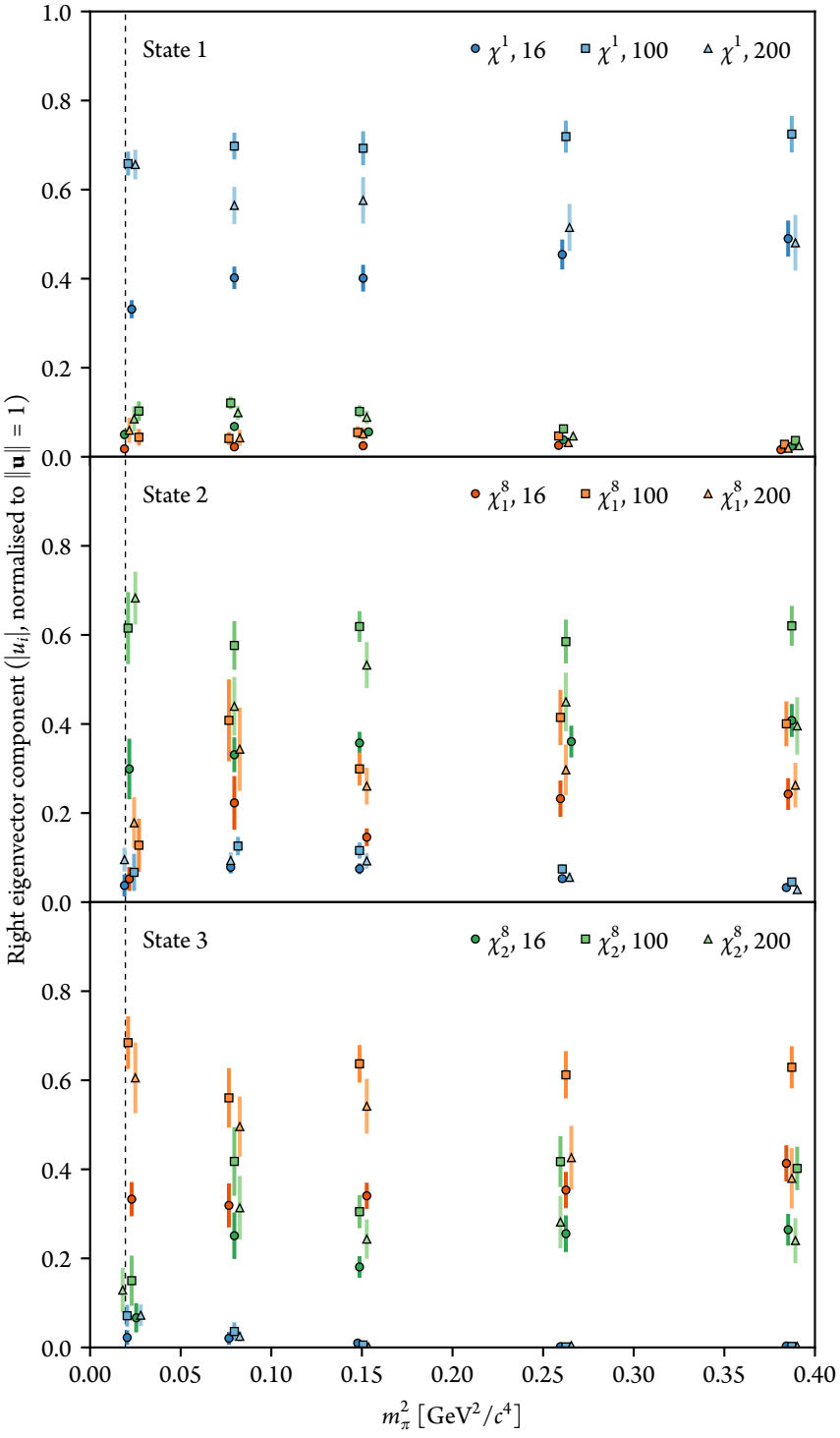
State 1
χ^1, 16
χ^1, 100
χ^1, 200
State 2
χ_1^8, 16
χ_1^8, 100
χ_1^8, 200
State 3
χ_2^8, 16
χ_2^8, 100
χ_2^8, 200
Right eigenvector component ($|u_i|$, normalised to $\|\mathbf{u}\| = 1$)
m_π^2 [GeV$^2/c^4$]
0.0
0.2
0.4
0.6
0.8
1.0
0.00
0.05
0.10
0.15
0.20
0.25
0.30
0.35
0.40

Figure 5.14: *(facing page)* The length of the projection of the left eigenvector onto SU(3)-flavour–symmetry–specific subspaces (that is, the subspaces spanned by the components associated with specific interpolating operators) across the ensembles used in this analysis. This gives a measure of the relative strength of each flavour-symmetry structure in each state, and clearly shows the dominance of the flavour-singlet structure for the lightest state (top plot). Points have been offset slightly on the m_π^2 axis to avoid collisions and aid viewing; the centre of each group of points lies at the true value. The legend presented in the top plot also applies to the other two plots of this Figure.

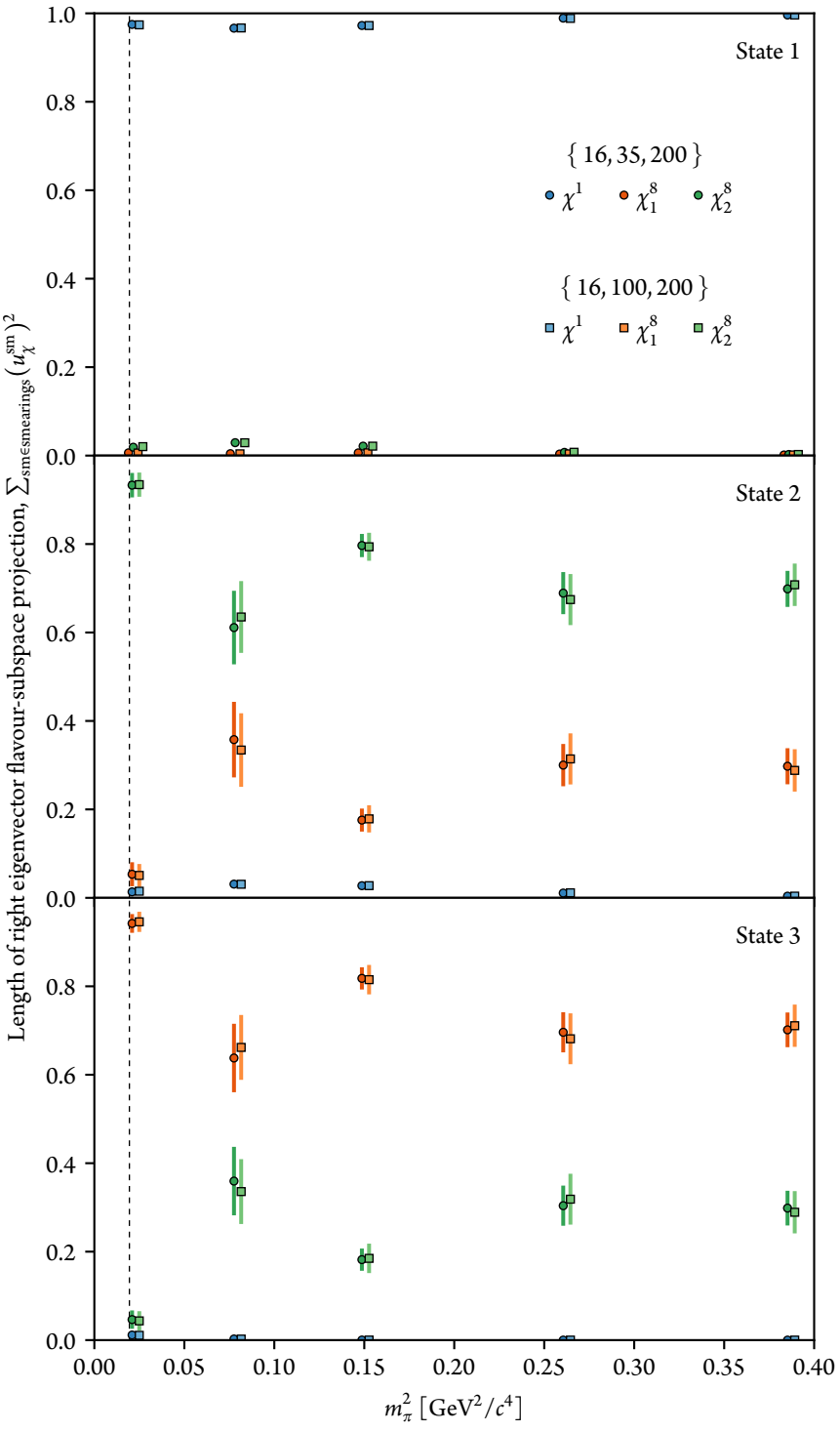
State 1
{ 16, 35, 200 }
χ^1 χ_1^8 χ_2^8
{ 16, 100, 200 }
χ^1 χ_1^8 χ_2^8
State 2
State 3
Length of right eigenvector flavour-subspace projection, $\sum_{\text{smésmearings}} (u_\chi^{\text{sm}})^2$
m_π^2 [GeV$^2/c^4$]
0.0
0.2
0.4
0.6
0.8
1.0
0.00
0.05
0.10
0.15
0.20
0.25
0.30
0.35
0.40

	16, 35, 200			16, 100, 200		
m_π [GeV/c^2]	χ^1	χ^8_1	χ^8_2	χ^1	χ^8_1	χ^8_2
0.6223(91)	0.996 16(54)	0.001 35(33)	0.002 49(39)	0.996 08(70)	0.001 40(37)	0.002 52(50)
0.5124(79)	0.9892(14)	0.003 53(88)	0.007 30(94)	0.9886(18)	0.003 85(98)	0.0076(13)
0.3882(55)	0.9725(42)	0.0061(22)	0.0214(35)	0.9724(51)	0.0062(22)	0.0214(43)
0.2821(48)	0.9664(51)	0.0044(24)	0.0292(45)	0.9670(56)	0.0040(20)	0.0290(51)
0.1515(67)	0.9749(87)	0.0062(44)	0.0189(75)	0.9739(77)	0.0058(38)	0.0203(67)

Table 5.3: The lengths of the projection of the left eigenvector onto the SU(3)-flavour–symmetry–specific subspaces formed by the span of each "flavoured" interpolating operator for the lowest-lying state for both smearing sets considered in this analysis. Both smearing sets agree well within errors.

✣ Six ✣

Electromagnetic Structure of the Λ(1405)

The results presented in this chapter were originally published in Physical Review Letters [61] along with several supporting conference proceedings [60, 89–91]. The Editors also selected the Letter as a "PRL Editors' Suggestion". Our presentation here is adapted from these manuscripts, with additional results relating to the electric charge radius and magnetic moment.

Now that we have developed an effective technique for isolating individual energy eigenstates, we can apply other lattice QCD techniques to investigate other properties of the $\Lambda(1405)$ on our finite volume lattice. The electromagnetic form factors are particularly interesting as they provide insight into the distribution of charge and magnetism within the $\Lambda(1405)$. Moreover, the form factors can be resolved one quark flavour at a time in lattice QCD, allowing us to directly investigate the internal structure of this mysterious baryon.

6.1 Sachs Electromagnetic Form Factors

In the same way that using eigenstate-projected correlation functions allows us to reduce the contamination from other eigenstates in an effective mass analysis, it can also be used to improve the effective Sachs electromagnetic form factors $\mathcal{G}_{\mathrm{E,M}}$ developed in Section 4.2.2. This allows us to investigate each energy eigenstate individually. As in the previous chapter, we use the operator basis obtained using the three "flavoured" interpolating operators at 16, 100, and 200 sweeps of gauge-invariant Gaussian smearing.

For a fixed inserted momentum, the momentum transfer is dependent on the mass of the state. As such, it will vary across the available ensembles. This means that to obtain a meaningful comparison between the ensembles we need to extrapolate to a common Q^2. The momentum transfer for the $\Lambda(1405)$ across the ensembles is tabulated in Table 6.1. To minimise the shift across the ensembles we select $Q^2 = 0.16\,\mathrm{GeV}^2/c^4$, since it is near the average of the available values, and use the dipole ansatz of Equation (4.50) to perform the adjustment. We assume that the magnetic form factors scale the same as the electric form

$m_\pi\,[\mathrm{GeV}/c^2]$	$Q^2_{\Lambda(1405)}\,[\mathrm{GeV}^2/c^4]$
0.6223(91)	0.142 206(49)
0.5124(79)	0.145 701(56)
0.3882(55)	0.160 165(98)
0.2821(48)	0.163 42(11)
0.1515(67)	0.169 390(88)

Table 6.1: Momentum transfer, Q^2, for the $\Lambda(1405)$ on each available ensemble.

factors at the quark-sector level for the small values of Q^2 considered here. This determines $\mathcal{G}_\mathrm{M}(0) = \mathcal{G}_\mathrm{M}/\mathcal{G}_\mathrm{E}$ for unit-charge quark sectors.

In Figure 6.1, we present the quark mass dependence of these form factors for the $\Lambda(1405)$, along with the contributions from individual, unit-charged quark sectors. To check that our extrapolation to a common Q^2 does not significantly change the results, we plot the form factors both before and after the extrapolation. These results are tabulated in Table 6.2. The conserved vector current was inserted at $t = 21$ as the eigenstate-projected two-point correlation functions are dominated by a single state by this time. Figure 6.2 illustrates the two-point correlation function and demonstrates the importance of our variational analysis.

At the heaviest u and d quark masses, approaching the SU(3)-flavour limit, $m_u = m_d = m_s$, the underlying approximate flavour-singlet structure is manifest in both $\mathcal{G}_E$ and $\mathcal{G}_M$ with the light and strange sectors contributing equally. However, at the lightest quark mass ensemble, closest to nature, the strange quark contribution to the magnetic form factor of the $\Lambda(1405)$ drops by an order of magnitude and approaches zero. As the simulation parameters describing the strange quark are held fixed, this is a remarkable environmental effect, and of unprecedented strength.

To ensure that this is not an artificial effect from the selection of the fit window, we plot the effective strange-sector contribution to the Sachs magnetic form factor in Figure 6.3. Clearly, any reasonable fit in the region of the plateau will produce a similarly-low value for the lightest ensemble.

To test if there is any basis dependence in this contribution to the magnetic form factor, we perform the same form factor analysis but using different levels of smearing. In particular, we consider $\{\,16, 100\,\}$, $\{\,35, 100\,\}$, $\{\,16, 35, 100\,\}$, and $\{\,16, 35, 100, 200\,\}$ in addition to the $\{\,16, 100, 200\,\}$ used above. A plot of the quark mass dependence of $\mathcal{G}^\mathrm{s}_\mathcal{M}$ for these operator bases is presented in Figure 6.4. All of these operator bases agree well within errors, and so we continue our analysis using the original set of smearings, $\{\,16, 100, 200\,\}$.

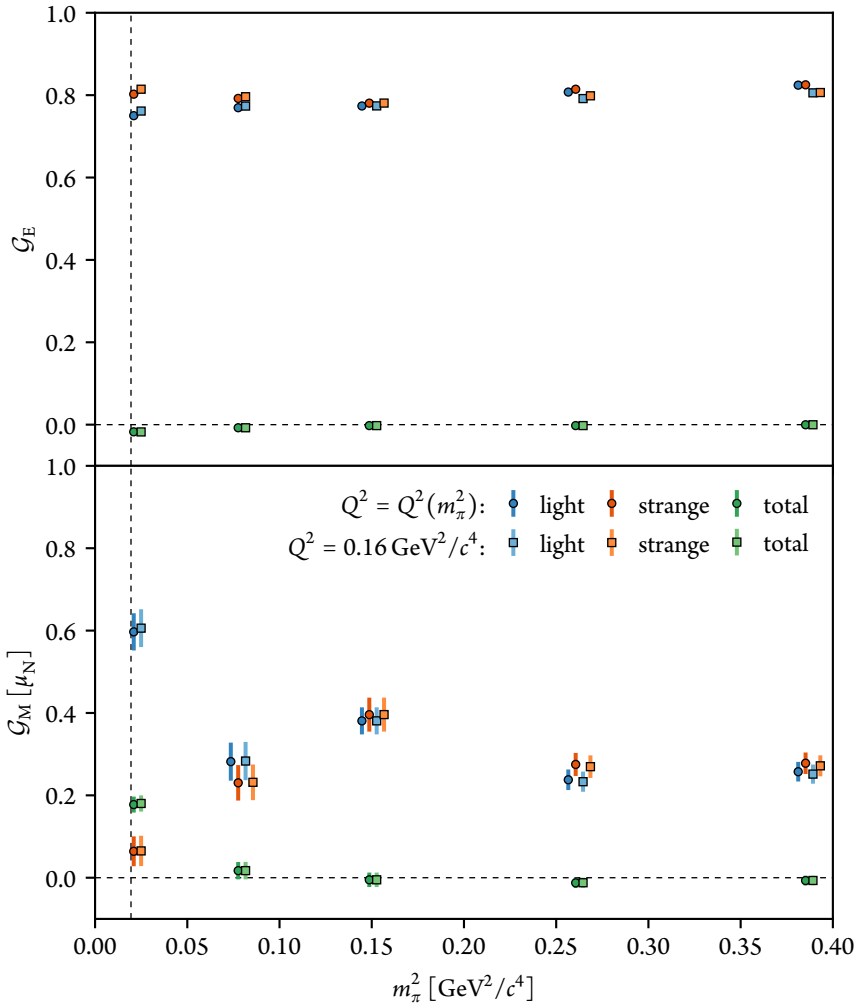

Figure 6.1: Dependence of the Sachs electric (top) and magnetic (bottom) form factors on the quark mass (as represented by the square of the pion mass) for the $\Lambda(1405)$, along with contributions from the individual unit-charged quark sectors. Values are plotted both before (left) and after (right) extrapolation to a common $Q^2 = 0.16\,\mathrm{GeV}^2/c^4$ using the dipole ansatz of Equation (4.50). The dashed, vertical line indicates the physical pion mass. Points have been offset slightly on the m_π^2 axis about their true values where needed to avoid collisions and aid viewing; where this occurs, the centre of the group lies at the true value.

	$Q^2 = Q^2(m_\pi^2)$			$Q^2 = 0.16\,\mathrm{GeV}^2/c^4$		
$m_\pi\,[\mathrm{GeV}/c^2]$	$\mathcal{G}_\mathrm{E}$	$\mathcal{G}_\mathrm{E}^{\mathrm{u,d}}$	$\mathcal{G}_\mathrm{E}^{\mathrm{s}}$	$\mathcal{G}_\mathrm{E}$	$\mathcal{G}_\mathrm{E}^{\mathrm{u,d}}$	$\mathcal{G}_\mathrm{E}^{\mathrm{s}}$
0.6223(91)	−0.0003(19)	0.8243(38)	0.8251(43)	−0.0003(19)	0.8056(41)	0.8064(42)
0.5124(79)	−0.0023(19)	0.8075(34)	0.8144(44)	−0.0022(18)	0.7917(36)	0.7984(44)
0.3882(55)	−0.0023(37)	0.7737(55)	0.7806(96)	−0.0023(37)	0.7739(55)	0.7808(96)
0.2821(48)	−0.0075(37)	0.7695(64)	0.7921(93)	−0.0076(38)	0.7735(63)	0.7962(93)
0.1515(67)	−0.0174(31)	0.7502(80)	0.8024(46)	−0.0177(31)	0.7614(77)	0.8144(47)
$m_\pi\,[\mathrm{GeV}/c^2]$	$\mathcal{G}_\mathrm{M}$	$\mathcal{G}_\mathrm{M}^{\mathrm{u,d}}$	$\mathcal{G}_\mathrm{M}^{\mathrm{s}}$	$\mathcal{G}_\mathrm{M}$	$\mathcal{G}_\mathrm{M}^{\mathrm{u,d}}$	$\mathcal{G}_\mathrm{M}^{\mathrm{s}}$
0.6223(91)	−0.007(12)	0.257(24)	0.278(26)	−0.007(11)	0.252(23)	0.272(25)
0.5124(79)	−0.012(12)	0.238(25)	0.275(28)	−0.012(12)	0.233(24)	0.270(27)
0.3882(55)	−0.005(18)	0.381(33)	0.396(41)	−0.005(18)	0.381(33)	0.396(41)
0.2821(48)	0.017(21)	0.282(46)	0.230(43)	0.017(21)	0.283(46)	0.232(43)
0.1515(67)	0.178(19)	0.597(45)	0.064(36)	0.180(20)	0.606(46)	0.065(37)

Table 6.2: Sachs electric (top) and magnetic (bottom) form factors for the Λ(1405) along with the contributions from individual (unit-charged) quark sectors both before and after extrapolation to a common $Q^2 = 0.16\,\mathrm{GeV}^2/c^4$ using the dipole ansatz of Equation (4.50). Magnetic form factors are expressed in terms of the nuclear magneton, μ_N.

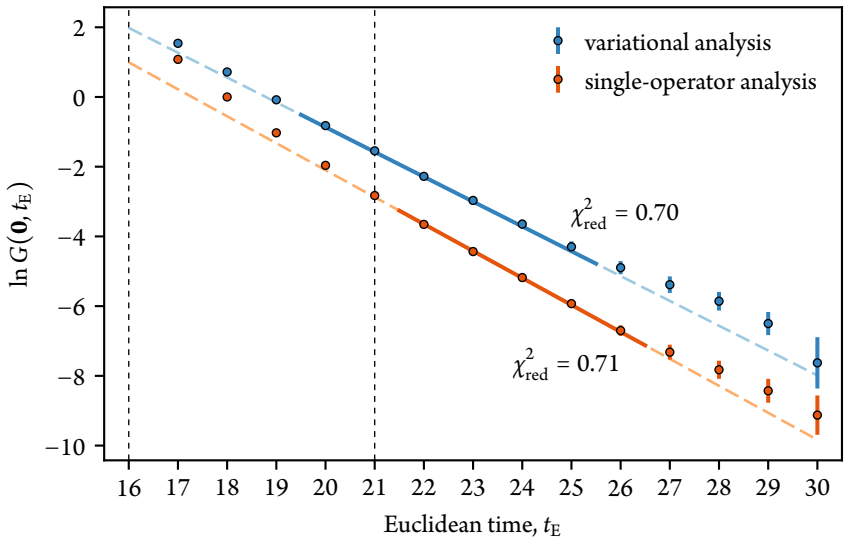

Figure 6.2: Two-point correlation function for the Λ(1405) on the ensemble with $\kappa_{\mathrm{u,d}} = 0.13781$ obtained through (blue) our "flavoured" variational analysis of Chapter 5 and (red) a traditional single-operator analysis (χ^1 with 16 sweeps of smearing). The fit windows were selected through a reduced-χ^2 analysis. The dashed vertical line at $t = 16$ indicates the baryon insertion time, while the dashed vertical line at $t = 21$ indicates the conserved vector current insertion time. Not only does the variational analysis produce a lower mass (represented here by the negative of the slope of the fits), but the projected correlation functions become dominated by a single state at a sooner time (represented by the earlier start time to the fits).

6.2 The Λ(1405) is a $\overline{\mathrm{K}}$N Molecular Bound State

If we consider the Λ(1405) as an elementary three-quark state, the strange quark must make a sizeable contribution to the magnetic form factor, with equal contributions from all three quarks in the SU(3)-flavour limit. Similarly, if we consider a $\pi\Sigma$ bound state, the strange quark is confined within the spin-1/2 Σ and so again should make a non-zero contribution to the magnetic form factor.

On the other hand, if we consider the Λ(1405) as a $\overline{\mathrm{K}}$N molecular bound state, the Λ(uds) valence quark configuration is complemented by a $u\bar{u}$ quark–antiquark pair making a $\overline{\mathrm{K}}^-$ ($s\bar{u}$) proton (uud) bound state, or a $d\bar{d}$ quark-antiquark pair making a $\overline{\mathrm{K}}^0$ ($s\bar{d}$) neutron (ddu) bound state. In both cases, the strange quark is confined within a spin-0 kaon and has no preferred spin orientation. Because of this and the fact that the antikaon must have zero orbital angular momentum in order to conserve parity, the strange quark cannot contribute

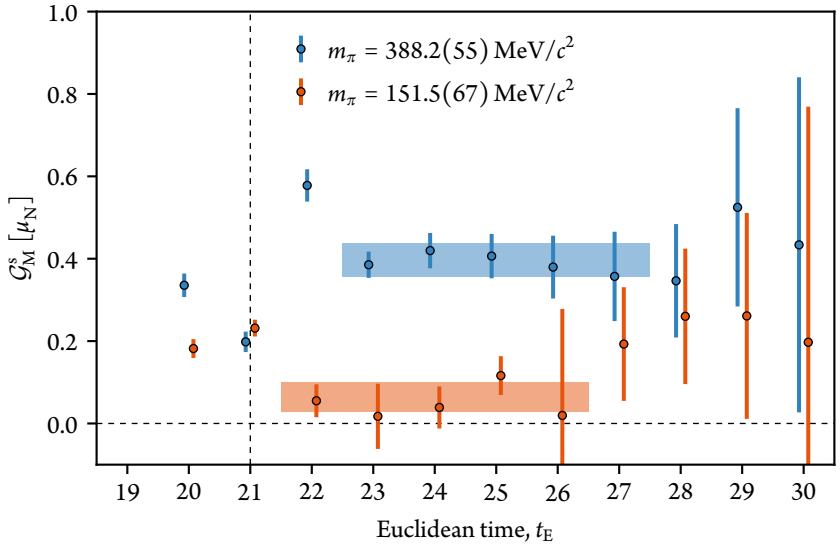

Figure 6.3: The effective unit-charge strange-quark contribution to the Sachs magnetic form factor on the ensembles with (blue) $m_\pi = 388.2(55)\,\mathrm{MeV}/c^2$ and (red) $m_\pi = 151.5(67)\,\mathrm{MeV}/c^2$. The "best fits" for these series were selected through an analysis of the reduced-χ^2 calculated from the full variance-covariance matrix. The electromagnetic current is inserted at $t = 21$ and represented by the dashed, vertical line, and the rapid onset of the plateau following this reflects our use of optimised interpolating-field operators through the variational analysis.

to the magnetic form factor of the $\Lambda(1405)$.

Thus, only if the $\overline{\mathrm{K}}\mathrm{N}$ component in the structure of the $\Lambda(1405)$ is dominant would one expect to find the vanishing strange quark magnetic form factor apparent in our results. As the u and d quark masses become light, and the cost of creating $u\bar{u}$ and $d\bar{d}$ quark-antiquark pairs from the QCD vacuum diminishes, we observe an important rearrangement of the quark structure within the $\Lambda(1405)$ consistent with the dominance of a molecular $\overline{\mathrm{K}}\mathrm{N}$ bound state.

As mentioned in the previous chapter, in [61] we use Hamiltonian effective field theory to construct a model focussing on various flavour-singlet couplings to a bare baryonic state, and use this to investigate the spectrum of the $J^P = 1/2^-$ Λ sector. Using this model, the emergence of a dominant molecular $\overline{\mathrm{K}}\mathrm{N}$ bound state as the quark mass approaches the physical values is directly reproduced.

Similarly, in [60, 91], we use partially-quenched chiral effective field theory to isolate and remove the disconnected interaction diagrams that are inaccessible to our direct lattice calculation. This enables a prediction of the light quark sector contributions to be

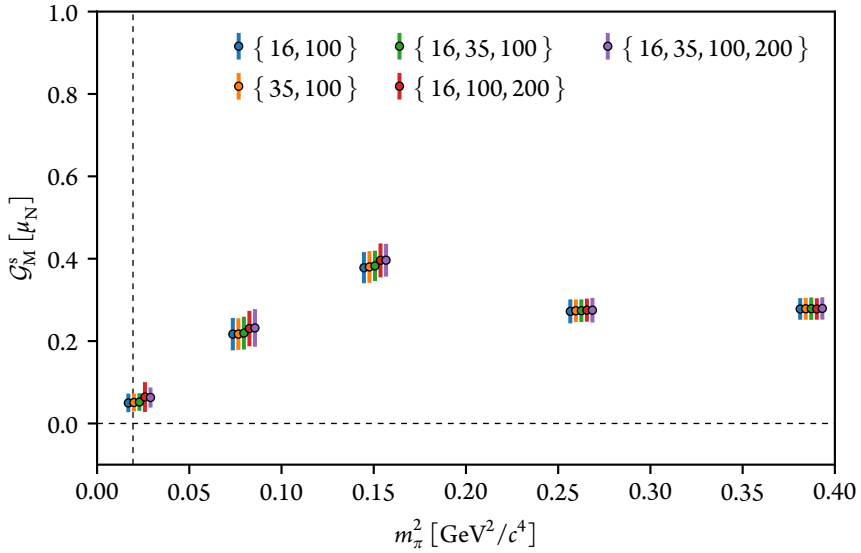

Figure 6.4: Dependence of the strange quark contribution to the Sachs magnetic form factor on the quark mass (as represented by the square of the pion mass) for the lowest-lying state (the $\Lambda(1405)$) extracted using various smearing bases. All operator bases agree within the statistical errors. Points have been offset slightly on the m_π^2 axis about their true values for ease of viewing; the central point for each group lies as the true value for m_π^2.

observed in our simulations. Towards the SU(3)-flavour limit, the predictions of this "connected $\overline{\mathrm{K}}\mathrm{N}$ model" (i.e. where only the connected interaction diagrams are included) are very different from our direct lattice calculations. However, once the $\Lambda(1405)$ rearranges its structure in the light-quark regime, there is good agreement between the model and our lattice results. This is manifest on the ensemble with the lightest quark mass, again confirming the development of a dominant molecular $\overline{\mathrm{K}}\mathrm{N}$ bound state in the structure of the $\Lambda(1405)$ as we move towards the physical limit.

These analyses are extended in [88] to include the flavour-octet couplings. At heavy quark masses, towards the SU(3) flavour limit, the authors show that the $\Lambda(1405)$ is dominated by a flavour-singlet bare baryon state. On the other hand, at light quark masses, towards the physical point, while there is some mixing of a flavour-octet bare baryonic state they confirm that the $\Lambda(1405)$ is dominated by a molecular bound $\overline{\mathrm{K}}\mathrm{N}$ component.

m_π [GeV/c^2]	$\langle r^2\rangle_{\mathrm{E}}$	$\langle r^2\rangle_{\mathrm{E}}^{\mathrm{u,d}}$	$\langle r^2\rangle_{\mathrm{E}}^{\mathrm{s}}$
0.6223(91)	0.0006(14)	0.3333(83)	0.3316(96)
0.5124(79)	0.0050(19)	0.3618(75)	0.3467(97)
0.3882(55)	0.0049(44)	0.399(12)	0.385(20)
0.2821(48)	0.0156(49)	0.400(14)	0.353(19)
0.1515(67)	0.0351(49)	0.426(17)	0.3210(90)

m_π [GeV/c^2]	μ	$\mu^{\mathrm{u,d}}$	μ^{s}
0.6223(91)	−0.0082(69)	0.312(29)	0.337(32)
0.5124(79)	−0.014(11)	0.295(31)	0.338(36)
0.3882(55)	−0.005(20)	0.492(43)	0.507(57)
0.2821(48)	0.025(28)	0.366(60)	0.291(55)
0.1515(67)	0.239(26)	0.796(63)	0.080(46)

Table 6.3: The (top) electric mean-squared charge radius and (bottom) magnetic moment for the $\Lambda(1405)$ obtained using a dipole ansatz for the small-Q^2 behaviour of $\mathcal{G}_{\mathrm{E}}$ and $\mathcal{G}_{\mathrm{M}}$, along with the contributions from the individual, unit-charged quark sectors. Mean-squared charge radii are expressed in units of fm^2, while the magnetic moments are expressed in terms of the nuclear magneton, μ_{N}.

6.3 Electric Charge Radius and Magnetic Moment

As we discussed in Section 4.2.2, we can use our values for the Sachs electromagnetic form factors to calculate the electric charge radius and magnetic moment, and these give us insight into the distribution of charge and spin within the state. As the states observed on the lattice are eigenstates and do not have an open decay channel, the use of a dipole to characterise the distribution is appropriate. Plots of these quantities for the $\Lambda(1405)$ are included in Figure 6.5, with the values tabulated in Table 6.3.

At the heaviest quark masses, approaching the flavour-symmetry limit, the mean-squared charge radius for the light quarks in the $\Lambda(1405)$ is the same as for the strange quark. This is consistent with the dominant component being a bare baryonic state, where all three quarks are treated equally with respect to the structure of the state. As we move towards the lighter quark masses, there is a small increase in the light quark mean-squared charge radius. This is expected, since the distribution will naturally "spread out" as the mass decreases. However, at the same time there is a decrease in the charge radius for the strange quark – since the mass of the strange quark is fixed, this is purely an environment effect.

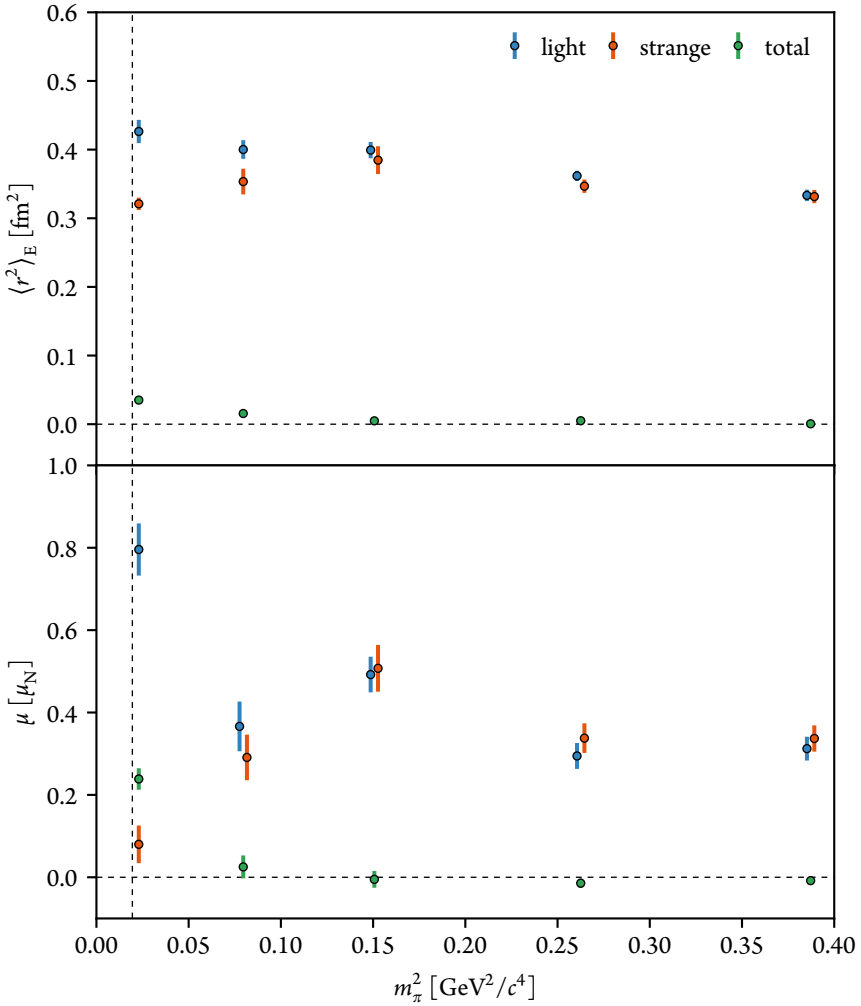

Figure 6.5: The (top) electric charge radius and (bottom) magnetic moment for the $\Lambda(1405)$, along with the contributions from the individual, unit-charged quark sectors. The dashed, vertical line indicates the physical pion mass. Individual quark sector contributions have been offset slightly on the m_π^2 axis about their true values where needed for ease of viewing; where this occurs, the centre of the group lies at the true value.

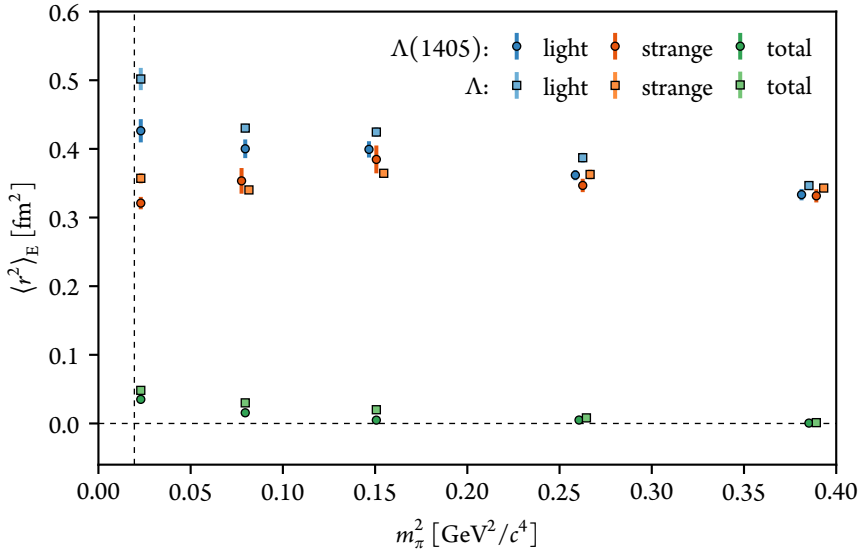

Figure 6.6: Comparison between the mean-squared charge radii of the Λ(1405) and the positive-parity ground-state Λ. The light-quark mean-squared charge radius of the Λ(1405) is suppressed relative to the ground state, which is consistent with the development of a significant $\overline{\text{K}}$N component in the structure of the Λ(1405). The dashed vertical line indicates the physical pion mass. Points have been offset slightly on the m_π^2 axis about their true values where needed to avoid collisions and aid viewing; where this occurs, the centre of the group lies at the true value.

If we compare these charge radii against the positive-parity, ground-state Λ, as demonstrated in Figure 6.6, we see that these results are also consistent with the development of a significant $\overline{\text{K}}$N component in the structure of the Λ(1405). Since the centre of mass will lie nearer to the heavier nucleon, the anti-light quarks will be distributed further out by the antikaon, and this will result in a suppressed light-quark charge radius for the Λ(1405) relative to the ground state.

For the magnetic moment, we note the large difference between the light and strange quark contributions as we move towards the physical quark mass. The same justification as for the near-vanishing strange magnetic form factor from the previous section applies: we would only expect the contribution from the strange quark to the magnetic moment to vanish in the limit that the Λ(1405) is purely a $\overline{\text{K}}$N molecular bound state, where the strange quark is confined with a spin-0 kaon with zero orbital angular momentum.

✣ Seven ✣
Concluding Remarks

Since its original prediction in 1959, and subsequent discovery in 1960, the nature of the $\Lambda(1405)$ has been the subject of intense debate. As we discussed early in this work, it is very difficult to reconcile the experimentally-observed unexpectedly-low mass with a simple three-quark state in a naïve constituent-quark model. On the other hand, since it sits just below the $\overline{\mathrm{K}}\mathrm{N}$ scattering threshold, we could describe it as a molecule-like bound state of an antikaon and a nucleon, and this approach has been explored through various theoretical and phenomenological formalisms.

Not only does this work form the first investigation of the low-lying $J^P = 1/2^-$ spectrum of the Λ baryon at near-physical pion masses using lattice QCD, it is also the first lattice QCD study to demonstrate the isolation of the elusive $\Lambda(1405)$. Not only do we reproduce the physical masses for *all* of the experimentally-observed resonant states in the $J^P = 1/2^-$ Λ sector, but we do so using conventional three-quark operators. By analysing the eigenvectors obtained from our variational analysis, we observe that the $\Lambda(1405)$ is dominated by the flavour-singlet interpolating operators but contained important flavour-octet contributions at light u and d quark masses, far from the $\mathrm{SU}(3)$ symmetric point. This observation has since been independently confirmed by the BGR Collaboration in [92].

To complement our lattice calculations, we used Hamiltonian effective field theory to construct a model constrained by our lattice results. Using this model, we are able to clearly see the emergence of a dominant $\overline{\mathrm{K}}\mathrm{N}$ component in the structure of the $\Lambda(1405)$ as the quark masses approached their physical value.

Since this investigation, a Hamiltonian effective field theory calculation incorporating direct two-to-two particle interactions has been carried out in [88]; with these additional interactions, the two-pole structure of the $\Lambda(1405)$ is observed. As one approaches the physical light quark-mass regime, the bare quark-model-like basis state becomes associated with the third and fourth states of the finite-volume spectrum traditionally associated with octet flavour symmetry. The $\Lambda(1405)$ remains dominated by the $\overline{\mathrm{K}}\mathrm{N}$ component as observed in this work. This result is also independently supported by the unitary chiral perturbation theory analysis of Molina and Döring in [93, 94].

Continuing this work's lattice investigation of the $\Lambda(1405)$, we presented results for the Sachs electric and magnetic form factors, along with the associated electric mean-

squared charge radius and magnetic moment. Near the SU(3)-flavour symmetric limit, where the up, down, and strange quarks all have the same mass, our results here clearly demonstrate the effect of this symmetry, with all three quarks contributing equally. In this limit, the electric and magnetic form factors for the $\Lambda(1405)$ all but vanish, with a correspondingly-low result for the electric mean-squared charge radius and magnetic moment.

However, as we move towards the physical point, we observe a fundamental redistribution of the quarks within the $\Lambda(1405)$, and the contribution from the strange quark to the magnetic form factor nearly vanishes. This observation can only be reconciled if we admit a dominant $\overline{\mathrm{K}}\mathrm{N}$ component in the structure of the $\Lambda(1405)$, just as we found previously using our Hamiltonian model. The other possible structures—of a pure three-quark state and a $\pi\Sigma$ component—would require a substantial contribution from the strange quark to the magnetic form factor.

With this in mind, we used the recently redeveloped graded symmetry approach in partially-quenched chiral perturbation theory to identify and separate the contributions from connected and disconnected interaction diagrams. Since the disconnected diagrams are inaccessible in our lattice QCD study, we constructed a connected $\overline{\mathrm{K}}\mathrm{N}$ model where only the connected diagrams contribute to the coupling with an external electromagnetic current. Using this model, we demonstrate that the contribution from the light-quark sector to the magnetic form factor from our lattice results is consistent with a $\overline{\mathrm{K}}\mathrm{N}$ model on the lightest ensemble available in this work. At this point the lattice QCD results and our connected $\overline{\mathrm{K}}\mathrm{N}$ model are remarkably consistent, again confirming the $\overline{\mathrm{K}}\mathrm{N}$ structure of the $\Lambda(1405)$.

Combining all of these results together and summarising, we have presented compelling evidence that the $\Lambda(1405)$ is dominated by a molecule-like bound state of an antikaon and a nucleon in the physical limit. This structure is signified by

- the vanishing of the strange quark contribution to the magnetic moment,
- the agreement between the connected $\overline{\mathrm{K}}\mathrm{N}$ model and our light quark form factors at the lightest ensemble, with $m_\pi = 156\,\mathrm{MeV}/c^2$, and
- the dominance of the $\overline{\mathrm{K}}\mathrm{N}$ component found in the finite-volume Hamiltonian effective field theory treatment.

At the same time, the presence of a non-trivial flavour-singlet three-quark component explains why the state is readily accessible through our variational analysis constructed using only local three-quark interpolating operators. Moreover, our ability to excite this state with a localised three-quark interpolating operator provides further evidence of a localised bound state.

From a broader perspective, we have presented evidence for the existence of molecular meson-baryon bound states in QCD. The evidence is firmly founded on the electromagnetic structure of the $\Lambda(1405)$ and supported by more traditional spectral analyses. If the kaon and nucleon can form bound states, it is natural to search for $K\Sigma$ and $K\Lambda$ bound states in the odd-parity nucleon resonance spectrum. Again, an exploration of the electromagnetic structure of these states as performed in this study for the $\Lambda(1405)$ will be vital to disclosing the presence of molecular meson-baryon bound states.

For future investigations of the $\Lambda(1405)$, it would be instructive to explore and isolate the contributions from nearby multi-particle scattering states using multi-particle interpolating operators, both to the energy spectrum and to the electromagnetic form factors (especially through their individual quark sector contributions). Using the very developed framework in [95, 96] it should then be possible to combine all the low-lying contributions observed in lattice QCD and make contact with the full resonance structure.

Bibliography

[1] R. H. Dalitz and S. F. Tuan, Phys. Rev. Lett. **2**, 425 (1959).

[2] R. Dalitz and S. Tuan, Ann. Phys. **10**, 307 (1960).

[3] M. Alston, L. W. Alvarez, P. Eberhard, M. L. Good, W. Graziano, H. K. Ticho and S. G. Wojcicki, Phys. Rev. Lett. **5**, 520 (1960).

[4] M. H. Alston, L. W. Alvarez, P. Eberhard, M. L. Good, W. Graziano, H. K. Ticho and S. G. Wojcicki, Phys. Rev. Lett. **6**, 698 (1961).

[5] A. Engler et al., Phys. Rev. Lett. **15**, 224 (1965).

[6] C. Patrignani et al., Chin. Phys. C **40**, 100001 (2016).

[7] N. Isgur and G. Karl, Phys. Rev. D **18**, 4187 (1978).

[8] N. Isgur and G. Karl, Phys. Rev. D **20**, 1191 (1979).

[9] S. Capstick and N. Isgur, Phys. Rev. D **34**, 2809 (1986).

[10] R. H. Dalitz, T. C. Wong and G. Rajasekaran, Phys. Rev. **153**, 1617 (1967).

[11] E. A. Veit, B. K. Jennings, R. C. Barrett and A. W. Thomas, Phys. Lett. B **137**, 415 (1984).

[12] E. A. Veit, B. K. Jennings, A. W. Thomas and R. C. Barrett, Phys. Rev. D **31**, 1033 (1985).

[13] N. Kaiser, P. Siegel and W. Weise, Nucl. Phys. A **594**, 325 (1995).

[14] D. Jido, T. Sekihara, Y. Ikeda, T. Hyodo, Y. Kanada-En'yo and E. Oset, Nucl. Phys. A **835**, 59 (2010).

[15] Y. Nemoto, N. Nakajima, H. Matsufuru and H. Suganuma, Phys. Rev. D **68**, 094505 (2003).

[16] T. Burch, C. Gattringer, L. Y. Glozman, C. Hagen, D. Hierl, C. B. Lang and A. Schäfer, Phys. Rev. D **74**, 014504 (2006).

[17] T. T. Takahashi and M. Oka, Phys. Rev. D **81**, 034505 (2010).

[18] M. S. Mahbub, W. Kamleh, D. B. Leinweber, P. J. Moran and A. G. Williams, Phys. Rev. D **87**, 011501 (2013).

[19] J. Chadwick, Nature **129**, 312 (1932).

[20] V. D. Hopper and S. Biswas, Phys. Rev. **80**, 1099 (1950).

[21] M. Gell-Mann, *The Eightfold Way: A Theory of Strong Interaction Symmetry*, tech. rep. CTSL-20 (California Institute of Technology, 1961).

[22] M. Gell-Mann, Phys. Rev. **125**, 1067 (1962).

[23] Y. Ne'eman, Nucl. Phys. **26**, 222 (1961).

[24] M. Gell-Mann, in proceedings of the 11th International Conference on High-Energy Physics (ICHEP'62), Geneva, Switzerland, Jul 4–11, 1962, edited by J. Prentki (1962), pp. 533–542.

[25] R. E. Behrends, J. Dreitlein, C. Fronsdal and W. Lee, Rev. Mod. Phys. **34**, 1 (1962).

[26] S. L. Glashow and J. J. Sakurai, Nuovo Cimento **26**, 622 (1962).

[27] V. E. Barnes et al., Phys. Rev. Lett. **12**, 204 (1964).

[28] M. Gell-Mann, Phys. Lett. **8**, 214 (1964).

[29] G. Zweig, in *Developments in the Quark Theory of Hadrons, vol. 1: 1964–1978*, edited by D. B. Lichtenberg and S. P. Rosen (Hadronic Press, 1964), pp. 22–101.

[30] N. Isgur and G. Karl, Phys. Lett. B **72**, 109 (1977).

[31] N. Isgur and G. Karl, Phys. Rev. D **19**, 2653 (1979).

[32] R. Aaij et al., Phys. Rev. Lett. **112**, 222002 (2014).

[33] R. Aaij et al., Phys. Rev. Lett. **115**, 072001 (2015).

[34] O. W. Greenberg, Phys. Rev. Lett. **13**, 598 (1964).

[35] M. Y. Han and Y. Nambu, Phys. Rev. **139**, B1006 (1965).

[36] H. Fritzsch, M. Gell-Mann and H. Leutwyler, Phys. Lett. B **47**, 365 (1973).

[37] C. N. Yang and R. L. Mills, Phys. Rev. **96**, 191 (1954).

[38] T.-P. Cheng and L.-F. Li, *Gauge Theory of Elementary Particle Physics* (Oxford University Press, 1988).

[39] P. Skands, in *Searching for New Physics at Small and Large Scales*, proceedings of the 2012 Theoretical Advanced Study Institute In Elementary Particle Physics (TASI 2012), Boulder, Colorado, June 4–29, 2012, edited by M. Schmaltz and E. Pierpaoli (Sept. 2013).

[40] W. Greiner, S. Schramm and E. Stein, *Quantum Chromodynamics* (Springer, 2007).

[41] K. G. Wilson, Phys. Rev. D **10**, 2445 (1974).

[42] A. S. Kronfeld, Annu. Rev. Nucl. Part. Sci. **62**, 265 (2012).

[43] I. F. Allison, C. T. H. Davies, A. Gray, A. S. Kronfeld, P. B. Mackenzie and J. N. Simone, Phys. Rev. Lett. **94**, 172001 (2005).

[44] E. B. Gregory, C. T. H. Davies, E. Follana, E. Gamiz, I. D. Kendall, G. P. Lepage, H. Na, J. Shigemitsu and K. Y. Wong, Phys. Rev. Lett. **104**, 022001 (2010).

[45] K. Langfeld, Phys. Rev. D **69**, 014503 (2004).

[46] E.-A. O'Malley, W. Kamleh, D. Leinweber and P. Moran, Phys. Rev. D **86**, 054503 (2012).

[47] D. Trewartha, W. Kamleh and D. Leinweber, Phys. Lett. B **747**, 373 (2015).

[48] H. J. Rothe, World Sci. Lect. Notes Phys. **43**, 1 (1992).

[49] R. Gupta, in *Probing the Standard Model of Particle Interactions*, proceedings of the Les Houches 1997 Summer School in Theoretical Physics, Session 68, Les Houches, France, July 28–September 5, 1997, edited by R. Gupta, A. Morel, E. De Rafael and F. David (1997), pp. 83–219.

[50] H. Nielsen and M. Ninomiya, Nucl. Phys. B **185**, 20 (1981).

[51] S. Aoki et al., Phys. Rev. D **79**, 034503 (2009).

[52] Y. Iwasaki, 'Renormalization Group Analysis of Lattice Theories and Improved Lattice Action – Part II: Four-dimensional non-Abelian SU(N) gauge model', 1983.

[53] B. Sheikholeslami and R. Wohlert, Nucl. Phys. B **259**, 572 (1985).

[54] S. Aoki et al., Phys. Rev. D **73**, 034501 (2006).

[55] H. A. van der Vorst, SIAM J. Sci. and Stat. Comput. **13**, 631 (1992).

[56] Å. Björck and T. Elfving, BIT Numer. Math. **19**, 145 (1979).

[57] R. Babich, R. C. Brower, M. A. Clark, G. T. Fleming, J. C. Osborn, C. Rebbi and D. Schaich, Phys. Rev. D **85**, 054510 (2012).

[58] G. S. Bali et al., Phys. Rev. Lett. **108**, 222001 (2012).

[59] A. Abdel-Rehim, C. Alexandrou, M. Constantinou, V. Drach, K. Hadjiyiannakou, K. Jansen, G. Koutsou and A. Vaquero, Phys. Rev. D **89**, 034501 (2014).

[60] J. M. M. Hall, W. Kamleh, D. B. Leinweber, B. J. Menadue, B. J. Owen and A. W. Thomas, in proceedings of the 26th International Nuclear Physics Conference (INPC2016), Adelaide, Australia, September 11–16, 2016 (2017).

[61] J. M. M. Hall, W. Kamleh, D. B. Leinweber, B. J. Menadue, B. J. Owen, A. W. Thomas and R. D. Young, Phys. Rev. Lett. **114**, 132002 (2015).

[62] C. Bernard, T. Draper, G. Hockney and A. Soni, 'Calculation of Weak Matrix Elements: Some Technical Aspects', in *Lattice Gauge Theory: A Challenge in Large-Scale Computing*, edited by B. Bunk, K. H. Mütter and K. Schilling (Springer US, Boston, MA, 1986), pp. 199–207.

[63] G. Martinelli, C. Sachrajda and A. Vladikas, Nucl. Phys. B **358**, 212 (1991).

[64] S. Boinepalli, D. B. Leinweber, A. G. Williams, J. M. Zanotti and J. B. Zhang, Phys. Rev. D **74**, 093005 (2006).

[65] M. G. Beckett, P. Coddington, B. Joó, C. M. Maynard, D. Pleiter, O. Tatebe and T. Yoshie, Comput. Phys. Commun. **182**, 1208 (2011).

[66] B. G. Lasscock, J. Hedditch, W. Kamleh, D. B. Leinweber, W. Melnitchouk, A. W. Thomas, A. G. Williams, R. D. Young and J. M. Zanotti, Phys. Rev. D **72**, 014502 (2005).

[67] F. M. Stokes, W. Kamleh, D. B. Leinweber, M. S. Mahbub, B. J. Menadue and B. J. Owen, Phys. Rev. D **92**, 114506 (2015).

[68] M. S. Mahbub, A. Ó. Cais, W. Kamleh, B. G. Lasscock, D. B. Leinweber and A. G. Williams, Phys. Rev. D **80**, 054507 (2009).

[69] B. Blossier, M. D. Morte, G. von Hippel, T. Mendes and R. Sommer, J. High Energy Phys. **2009**, 094 (2009).

[70] S. Basak, R. Edwards, G. T. Fleming, U. M. Heller, C. Morningstar, D. Richards, I. Sato and S. J. Wallace, Phys. Rev. D **72**, 074501 (2005).

[71] S. Basak, R. G. Edwards, G. T. Fleming, U. M. Heller, C. Morningstar, D. Richards, I. Sato and S. Wallace, Phys. Rev. D **72**, 094506 (2005).

[72] R. G. Edwards, J. J. Dudek, D. G. Richards and S. J. Wallace, Phys. Rev. D **84**, 074508 (2011).

[73] S. Güsken, Nucl. Phys. B Proc. Suppl. **17**, 361 (1990).

[74] D. S. Roberts, W. Kamleh and D. B. Leinweber, Phys. Rev. D **89**, 074501 (2014).

[75] B. J. Menadue, W. Kamleh, D. B. Leinweber and M. S. Mahbub, Phys. Rev. Lett. **108**, 112001 (2012).

[76] B. J. Menadue, W. Kamleh, D. B. Leinweber and M. S. Mahbub, AIP Conf. Proc. **1354**, 213 (2011).

[77] B. J. Menadue, W. Kamleh, D. B. Leinweber and M. S. Mahbub, PoS **LATTICE2011**, 129 (2011).

[78] B. J. Menadue, W. Kamleh, D. B. Leinweber and M. S. Mahbub, AIP Conf. Proc. **1418**, 130 (2011).

[79] M. Lüscher and U. Wolff, Nucl. Phys. B **339**, 222 (1990).

[80] C. Michael, Nucl. Phys. B **259**, 58 (1985).

[81] G. Janssen, B. C. Pearce, K. Holinde and J. Speth, Phys. Rev. D **52**, 2690 (1995).

[82] O. Krehl, R. Rapp and J. Speth, Phys. Lett. B **390**, 23 (1997).

[83] M. Döring, J. Haidenbauer, U.-G. Meißner and A. Rusetsky, EPJ A **47**, 163 (2011).

[84] W. Melnitchouk, S. Bilson-Thompson, F. D. R. Bonnet, J. N. Hedditch, F. X. Lee, D. B. Leinweber, A. G. Williams, J. M. Zanotti and J. B. Zhang, Phys. Rev. D **67**, 114506 (2003).

[85] M. S. Mahbub, W. Kamleh, D. B. Leinweber, P. J. Moran and A. G. Williams, Phys. Lett. B **707**, 389 (2012).

[86] M. Gell-Mann, R. J. Oakes and B. Renner, Phys. Rev. **175**, 2195 (1968).

[87] J. M. M. Hall, W. Kamleh, D. B. Leinweber, B. J. Menadue, B. J. Owen, A. W. Thomas and R. D. Young, PoS **LATTICE2014**, 094 (2014).

[88] Z.-W. Liu, J. M. M. Hall, D. B. Leinweber, A. W. Thomas and J.-J. Wu, Phys. Rev. D **95**, 014506 (2017).

[89] B. J. Menadue, W. Kamleh, D. B. Leinweber, M. Selim Mahbub and B. J. Owen, PoS **LATTICE2013**, 280 (2014).

[90] W. Kamleh, J. M. M. Hall, D. B. Leinweber, B. J. Menadue, B. J. Owen, A. W. Thomas and R. D. Young, PoS **CD15**, 037 (2016).

[91] J. M. M. Hall, W. Kamleh, D. B. Leinweber, B. J. Menadue, B. J. Owen and A. W. Thomas, Phys. Rev. D **95**, 054510 (2017).

[92] G. P. Engel, C. B. Lang and A. Schäfer, Phys. Rev. D **87**, 034502 (2013).

[93] R. Molina and M. Döring, Phys. Rev. D **94**, 056010 (2016).

[94] R. Molina and M. Döring, Phys. Rev. D **94**, 079901 (2016).

[95] R. A. Briceño, M. T. Hansen and A. Walker-Loud, Phys. Rev. D **91**, 034501 (2015).

[96] R. A. Briceño and M. T. Hansen, Phys. Rev. D **94**, 013008 (2016).

Appendix A

Exploring the Variational Parameters: Plots

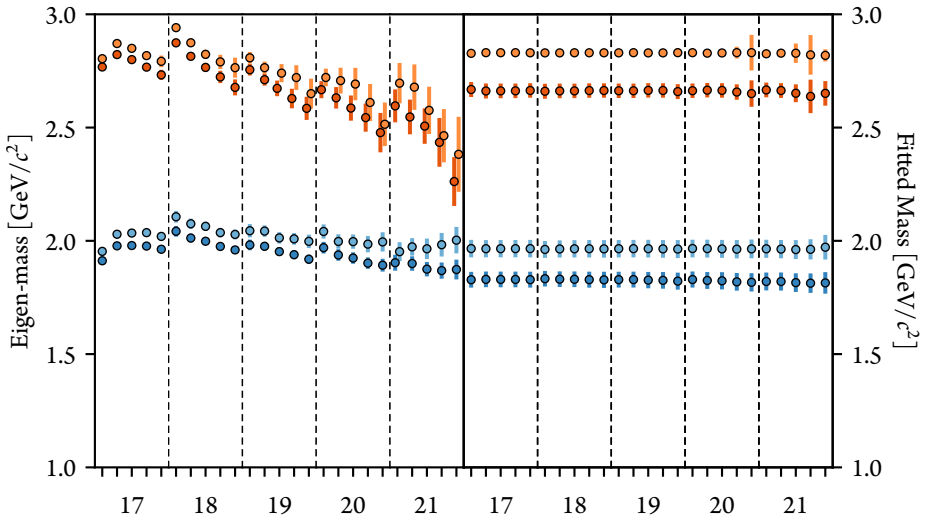

Figure A.1: Comparison of the masses extracted from the eigenvalues (left) and from fitting the projected effective mass (right) on the ensemble with $\kappa_{u,d} = 0.13700$ for $t_0 \in \{17, \ldots, 21\}$ and $\Delta t \in \{1, \ldots, 5\}$. Numbers of the abscissa indicate t_0 with Δt increasing within each t_0.

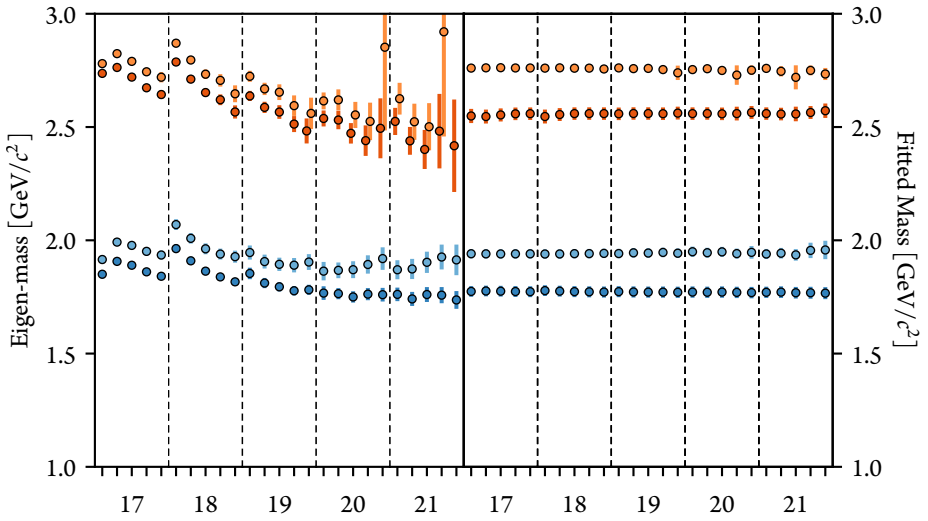

Figure A.2: Comparison of the masses extracted from the eigenvalues (left) and from fitting the projected effective mass (right) on the ensemble with $\kappa_{u,d} = 0.13727$ for $t_0 \in \{17, \ldots, 21\}$ and $\Delta t \in \{1, \ldots, 5\}$. Numbers of the abscissa indicate t_0 with Δt increasing within each t_0.

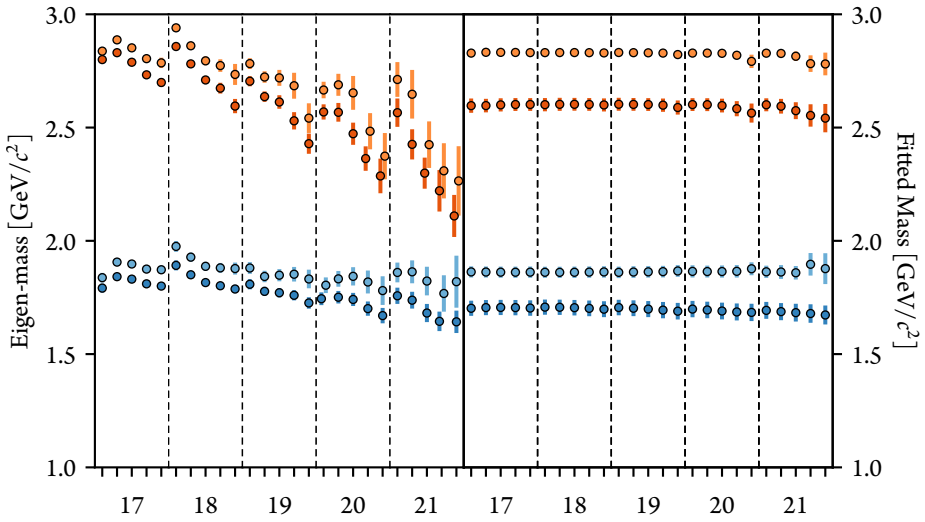

Figure A.3: Comparison of the masses extracted from the eigenvalues (left) and from fitting the projected effective mass (right) on the ensemble with $\kappa_{u,d} = 0.13754$ for $t_0 \in \{17, \ldots, 21\}$ and $\Delta t \in \{1, \ldots, 5\}$. Numbers of the abscissa indicate t_0 with Δt increasing within each t_0.

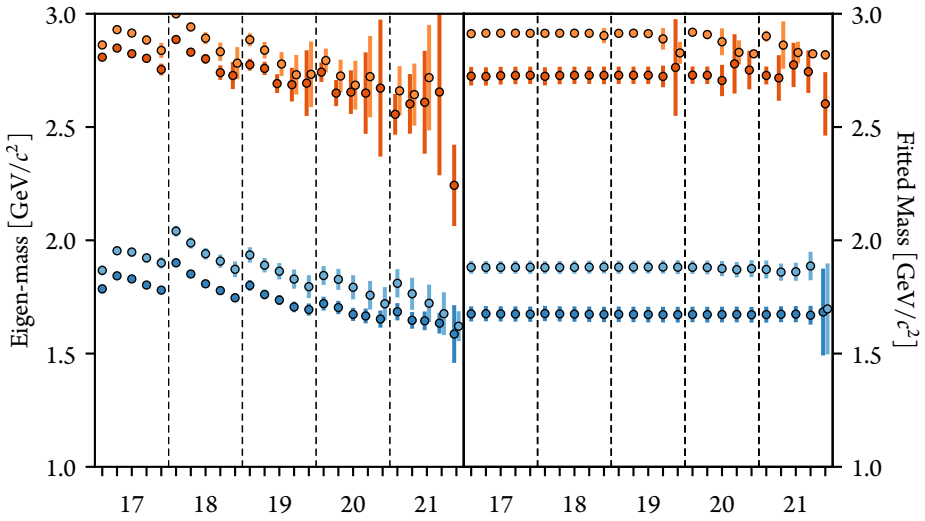

Figure A.4: Comparison of the masses extracted from the eigenvalues (left) and from fitting the projected effective mass (right) on the ensemble with $\kappa_{u,d} = 0.13770$ for $t_0 \in \{17, \ldots, 21\}$ and $\Delta t \in \{1, \ldots, 5\}$. Numbers of the abscissa indicate t_0 with Δt increasing within each t_0.

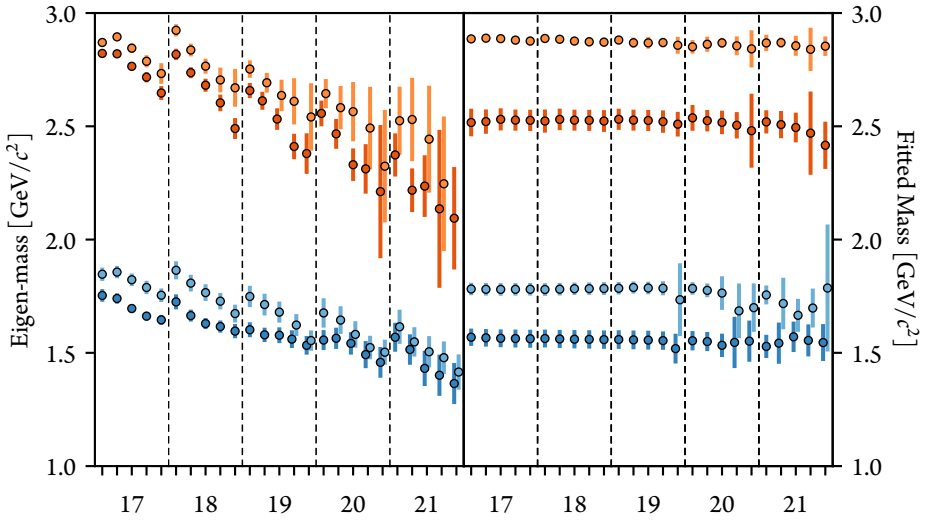

Figure A.5: Comparison of the masses extracted from the eigenvalues (left) and from fitting the projected effective mass (right) on the ensemble with $\kappa_{u,d} = 0.13781$ for $t_0 \in \{17, \ldots, 21\}$ and $\Delta t \in \{1, \ldots, 5\}$. Numbers of the abscissa indicate t_0 with Δt increasing within each t_0.

✣ Appendix B ✣

Exploring the Operator Space: Plots

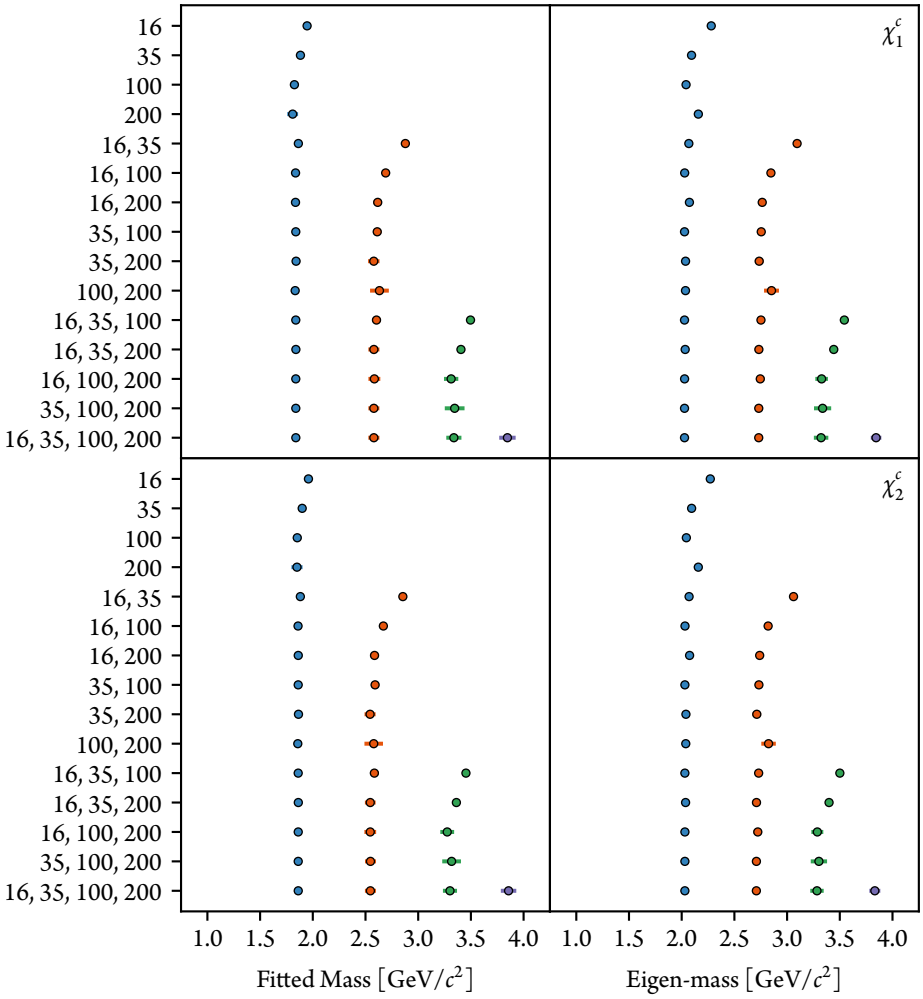

Figure B.1: Comparison of the masses extracted from fitting the projected effective mass (left) and from the eigenvalues (right) on the ensemble with $\kappa_{u,d} = 0.13700$ across all combinations of smearing levels using a single "common" interpolating operator.

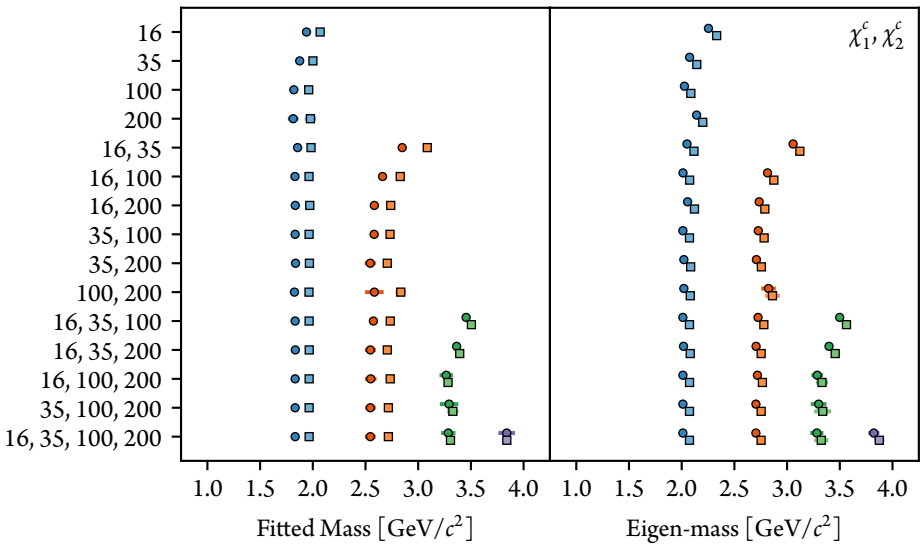

Figure B.2: Comparison of the masses extracted from fitting the projected effective mass (left) and from the eigenvalues (right) on the ensemble with $\kappa_{u,d} = 0.13700$ across all combinations of smearing levels using both "common" interpolating operators.

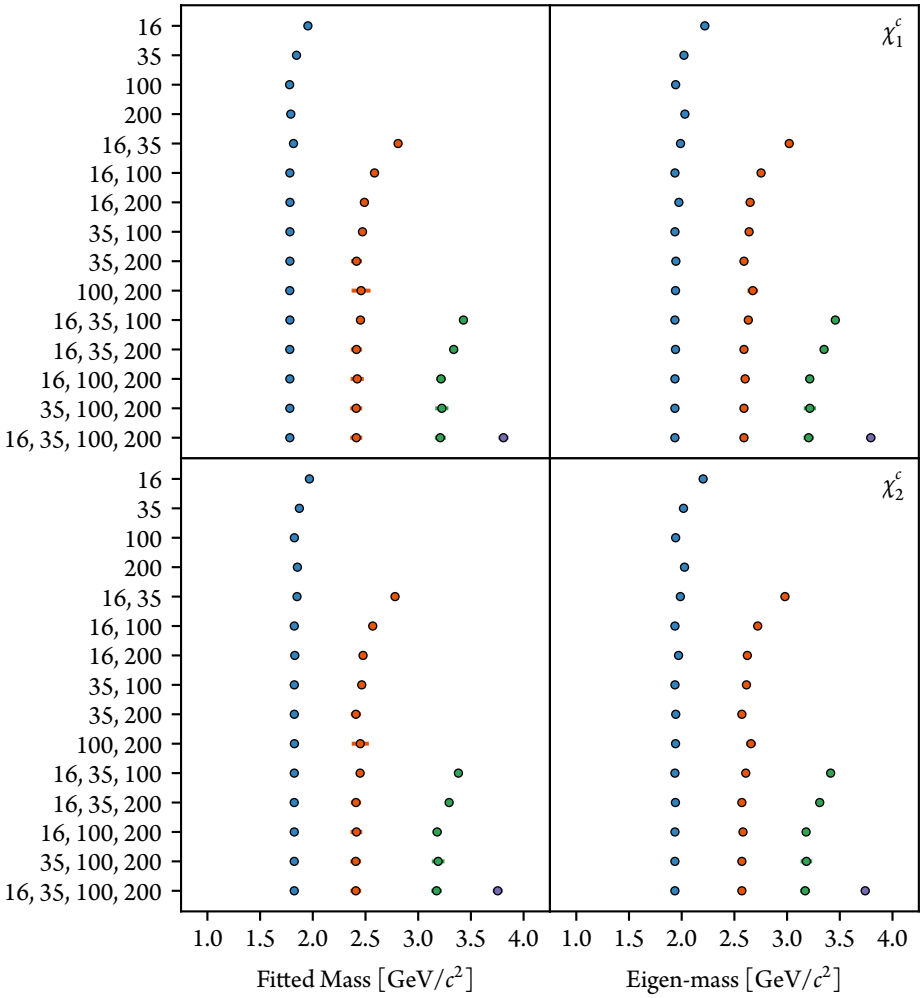

Figure B.3: Comparison of the masses extracted from fitting the projected effective mass (left) and from the eigenvalues (right) on the ensemble with $\kappa_{u,d} = 0.13727$ across all combinations of smearing levels using a single "common" interpolating operator.

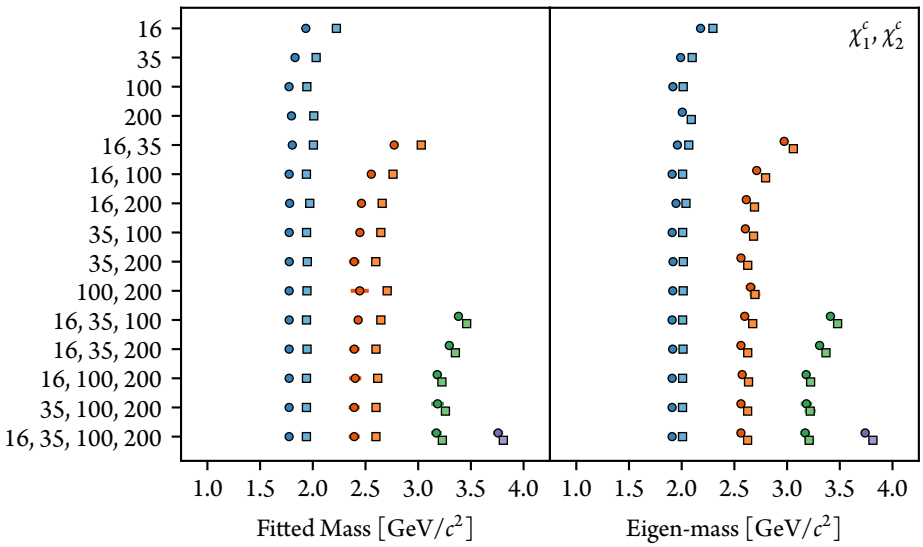

Figure B.4: Comparison of the masses extracted from fitting the projected effective mass (left) and from the eigenvalues (right) on the ensemble with $\kappa_{u,d} = 0.13727$ across all combinations of smearing levels using both "common" interpolating operators.

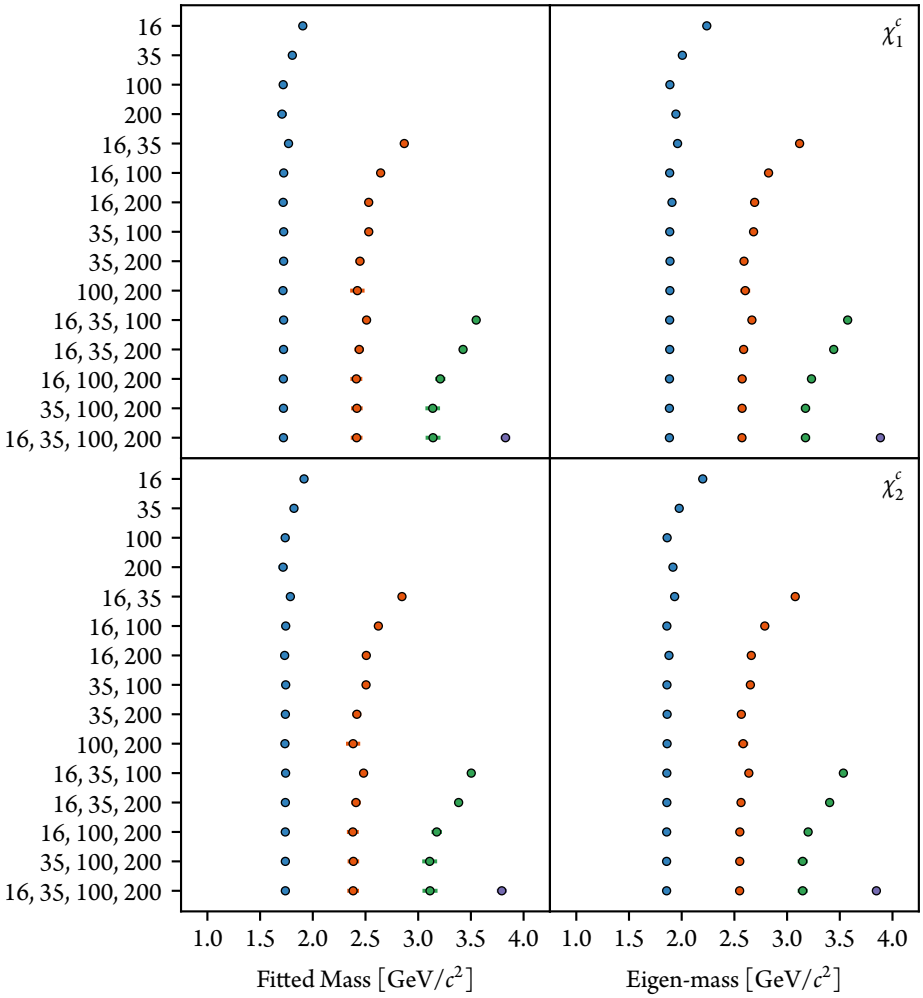

Figure B.5: Comparison of the masses extracted from fitting the projected effective mass (left) and from the eigenvalues (right) on the ensemble with $\kappa_{u,d} = 0.13754$ across all combinations of smearing levels using a single "common" interpolating operator.

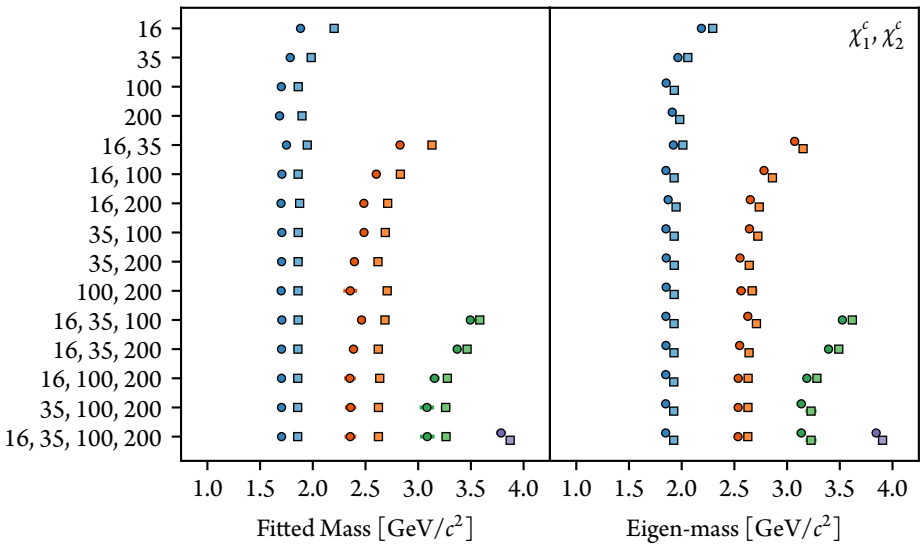

Figure B.6: Comparison of the masses extracted from fitting the projected effective mass (left) and from the eigenvalues (right) on the ensemble with $\kappa_{u,d} = 0.13754$ across all combinations of smearing levels using both "common" interpolating operators.

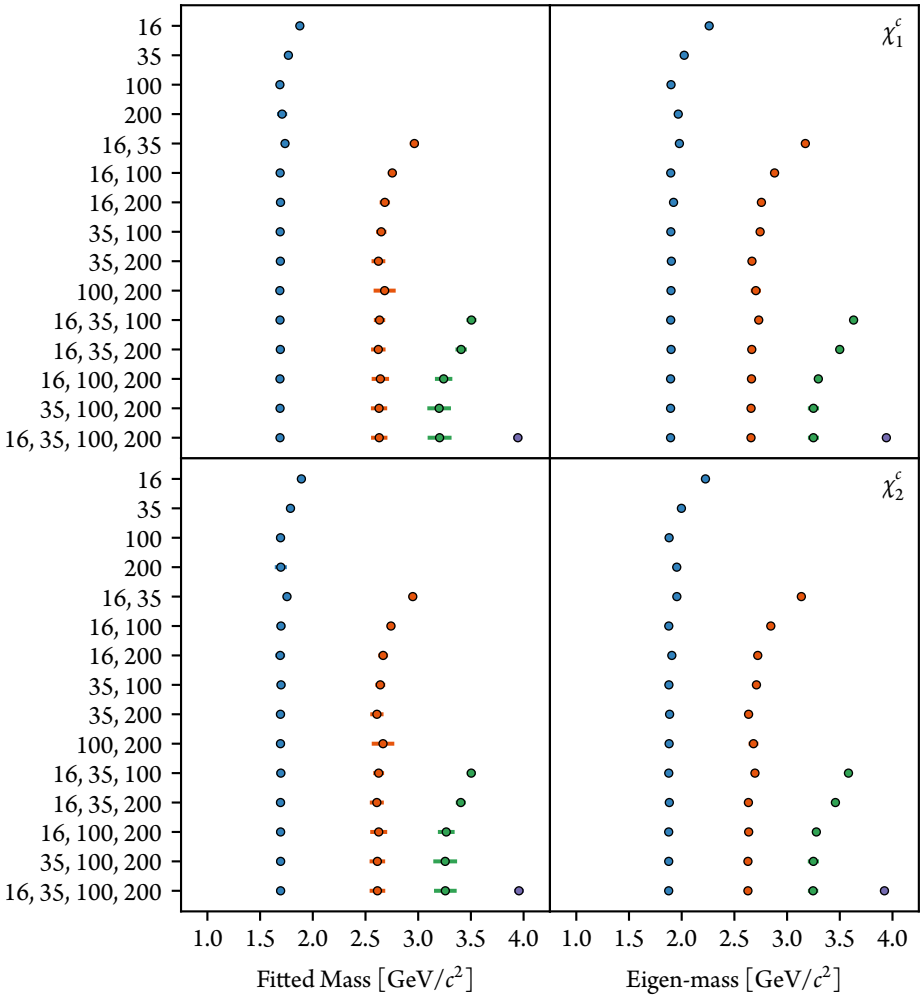

Figure B.7: Comparison of the masses extracted from fitting the projected effective mass (left) and from the eigenvalues (right) on the ensemble with $\kappa_{u,d} = 0.13770$ across all combinations of smearing levels using a single "common" interpolating operator.

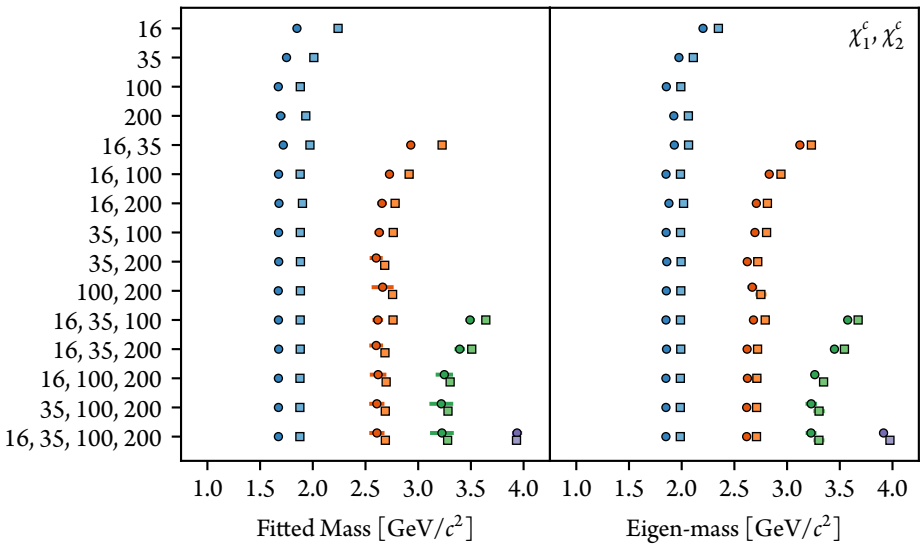

Figure B.8: Comparison of the masses extracted from fitting the projected effective mass (left) and from the eigenvalues (right) on the ensemble with $\kappa_{u,d} = 0.13770$ across all combinations of smearing levels using both "common" interpolating operators.

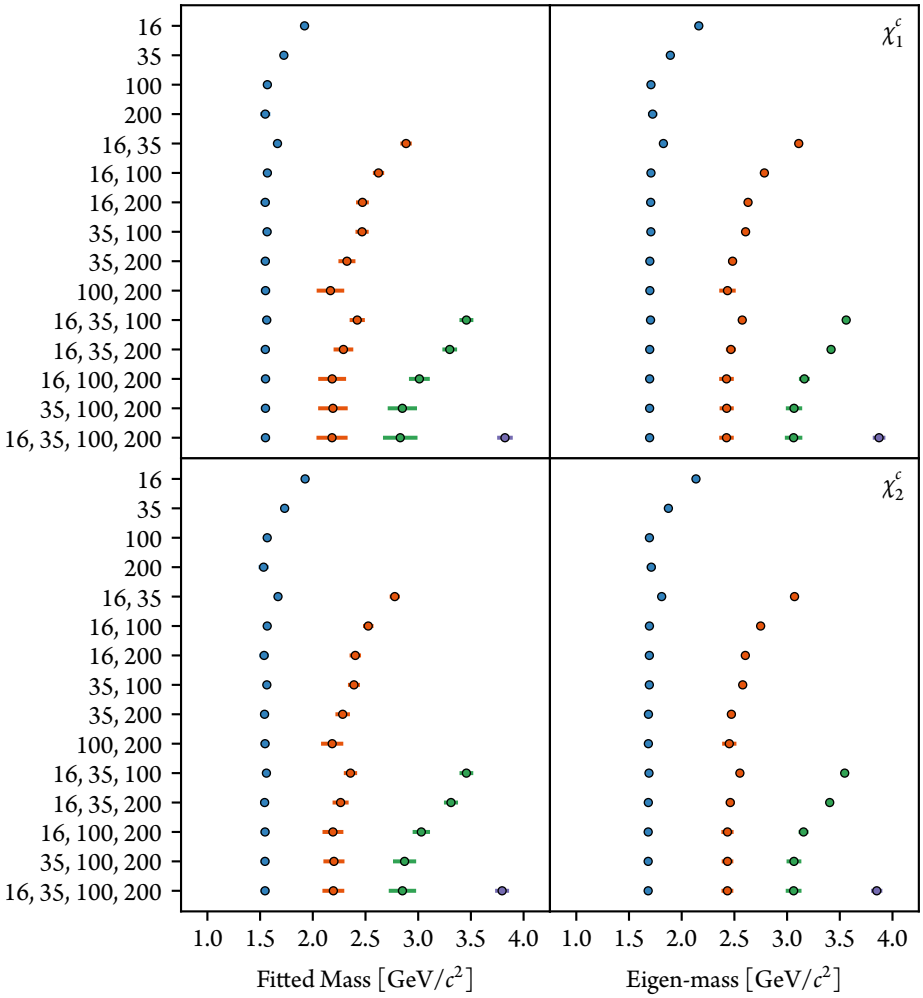

Figure B.9: Comparison of the masses extracted from fitting the projected effective mass (left) and from the eigenvalues (right) on the ensemble with $\kappa_{u,d} = 0.13781$ across all combinations of smearing levels using a single "common" interpolating operator.

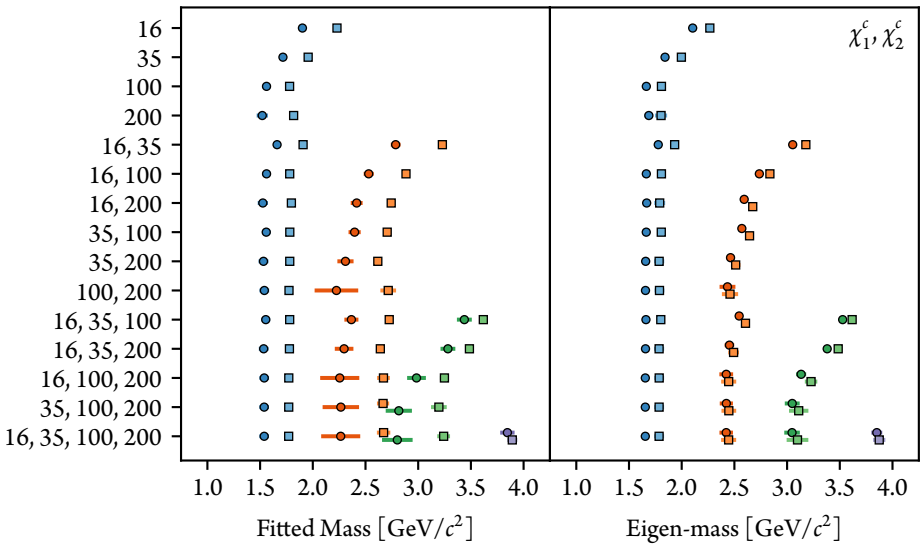

Figure B.10: Comparison of the masses extracted from fitting the projected effective mass (left) and from the eigenvalues (right) on the ensemble with $\kappa_{u,d} = 0.13781$ across all combinations of smearing levels using both "common" interpolating operators.

Figure B.11: *(facing page)* Comparison of the masses extracted from fitting the projected effective mass (left) and from the eigenvalues (right) on the ensemble with $\kappa_{u,d} = 0.13700$ across all combinations of smearing levels using a single "flavoured" interpolating operator.

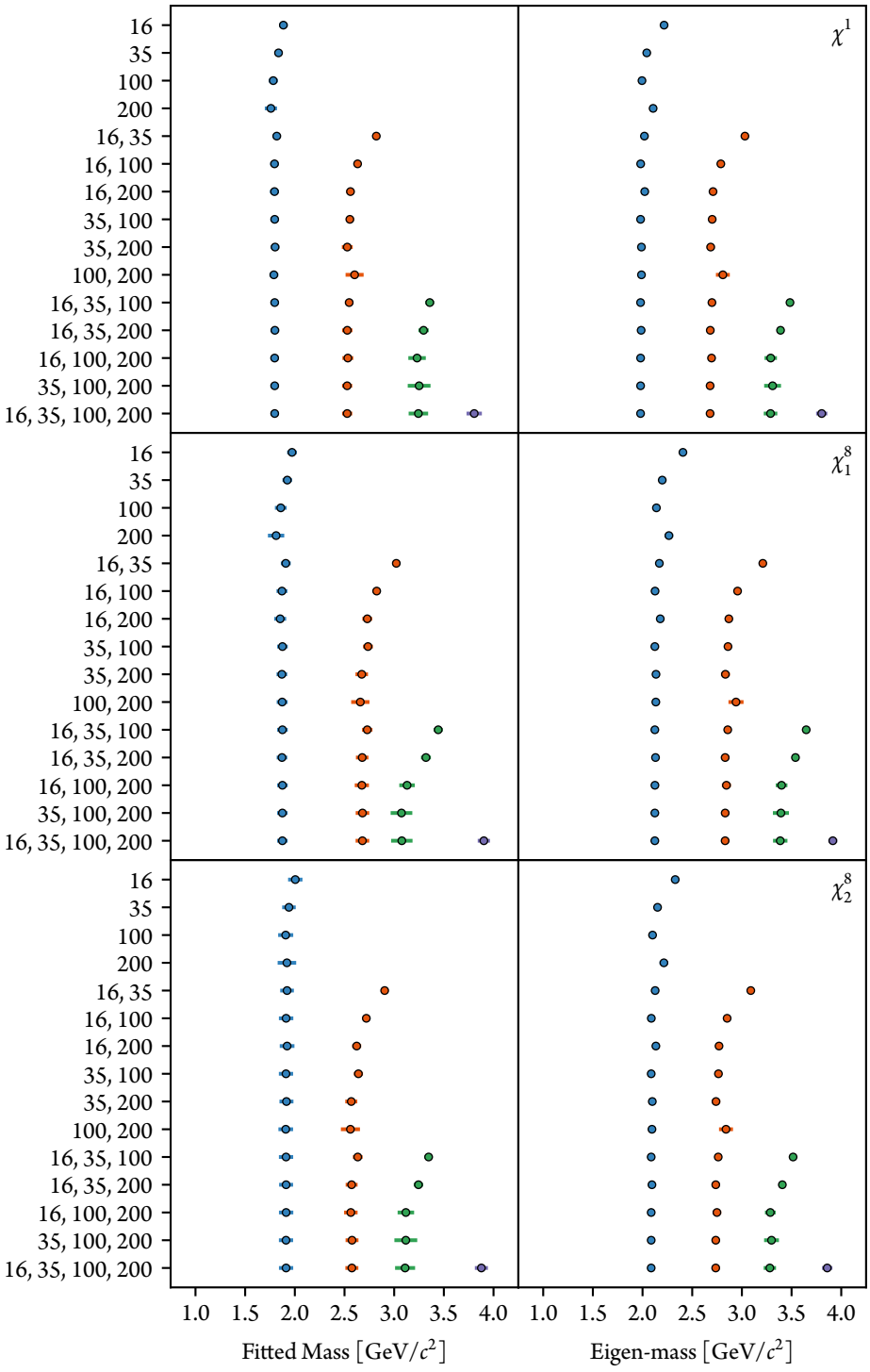
16
35
100
200
16, 35
16, 100
16, 200
35, 100
35, 200
100, 200
16, 35, 100
16, 35, 200
16, 100, 200
35, 100, 200
16, 35, 100, 200
χ^1
χ_1^8
χ_2^8
1.0 1.5 2.0 2.5 3.0 3.5 4.0
Fitted Mass [GeV/c^2]
Eigen-mass [GeV/c^2]

Figure B.12: *(facing page)* Comparison of the masses extracted from fitting the projected effective mass (left) and from the eigenvalues (right) on the ensemble with $\kappa_{u,d} = 0.13700$ across all combinations of smearing levels using two of the three "flavoured" interpolating operators.

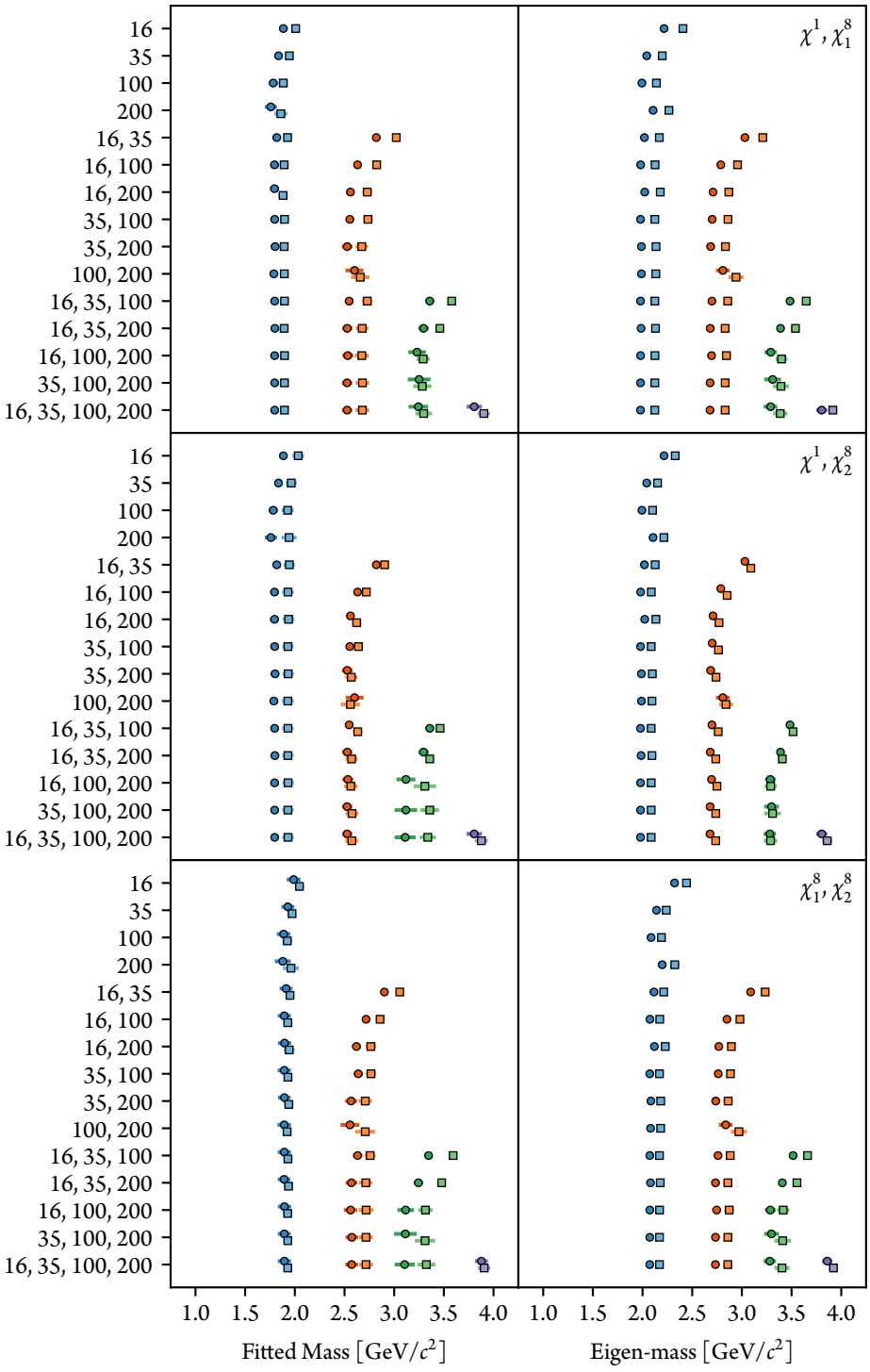
16
35
100
200
16, 35
16, 100
16, 200
35, 100
35, 200
100, 200
16, 35, 100
16, 35, 200
16, 100, 200
35, 100, 200
16, 35, 100, 200
χ^1, χ^8_1
χ^1, χ^8_2
χ^8_1, χ^8_2
1.0 1.5 2.0 2.5 3.0 3.5 4.0
Fitted Mass [GeV/c^2]
Eigen-mass [GeV/c^2]

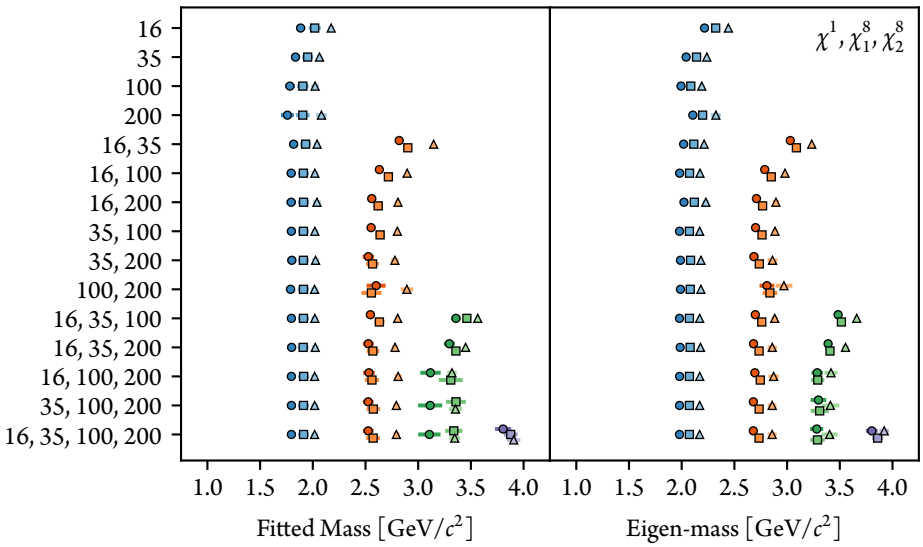

Figure B.13: Comparison of the masses extracted from fitting the projected effective mass (left) and from the eigenvalues (right) on the ensemble with $\kappa_{u,d} = 0.13700$ across all combinations of smearing levels using all three "flavoured" interpolating operators.

Figure B.14: *(facing page)* Comparison of the masses extracted from fitting the projected effective mass (left) and from the eigenvalues (right) on the ensemble with $\kappa_{u,d} = 0.13727$ across all combinations of smearing levels using a single "flavoured" interpolating operator.

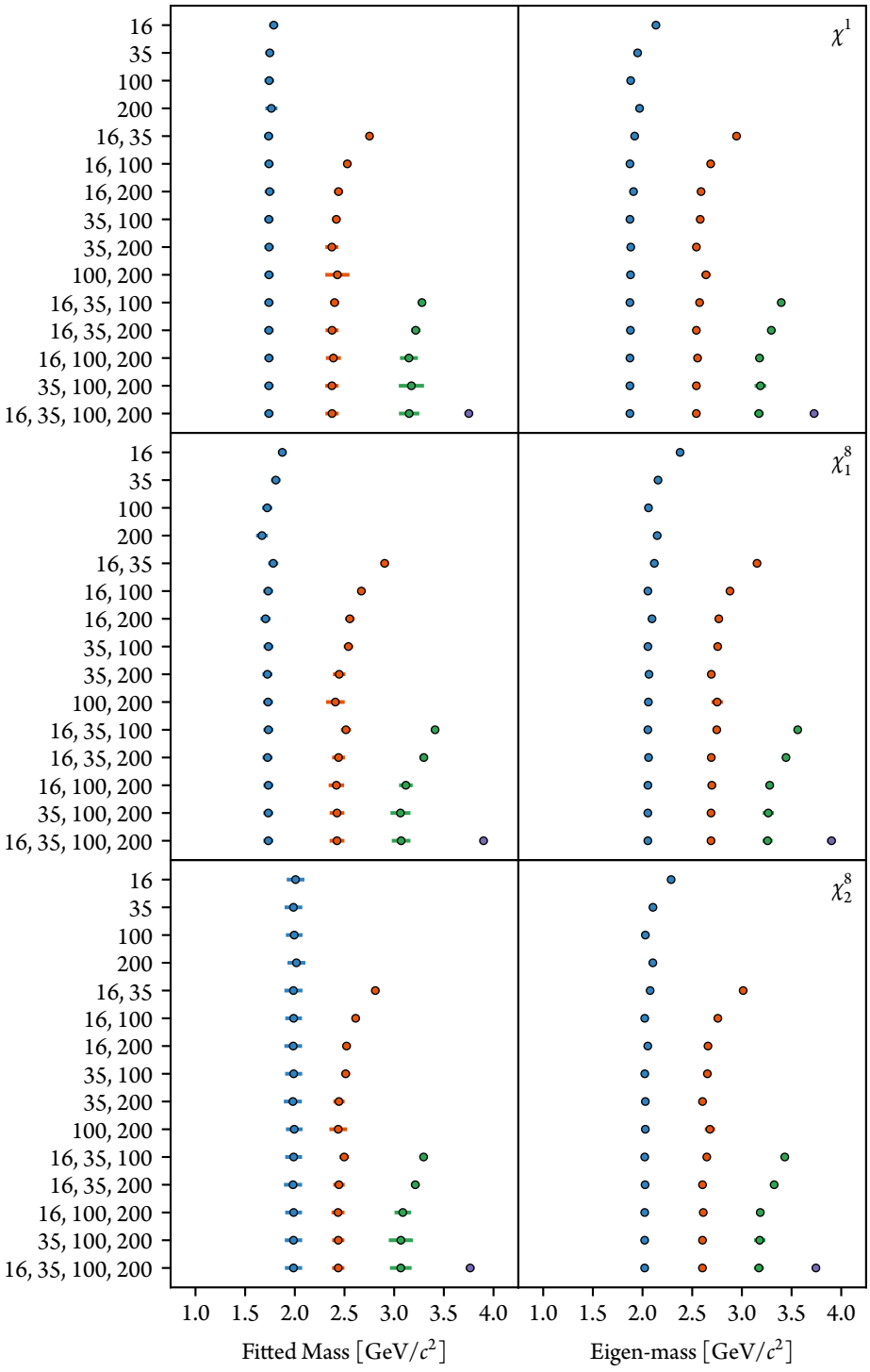
16
35
100
200
16, 35
16, 100
16, 200
35, 100
35, 200
100, 200
16, 35, 100
16, 35, 200
16, 100, 200
35, 100, 200
16, 35, 100, 200
χ^1
χ_1^8
χ_2^8
1.0
1.5
2.0
2.5
3.0
3.5
4.0
Fitted Mass [GeV/c^2]
Eigen-mass [GeV/c^2]

Figure B.15: *(facing page)* Comparison of the masses extracted from fitting the projected effective mass (left) and from the eigenvalues (right) on the ensemble with $\kappa_{u,d} = 0.13727$ across all combinations of smearing levels using two of the three "flavoured" interpolating operators.

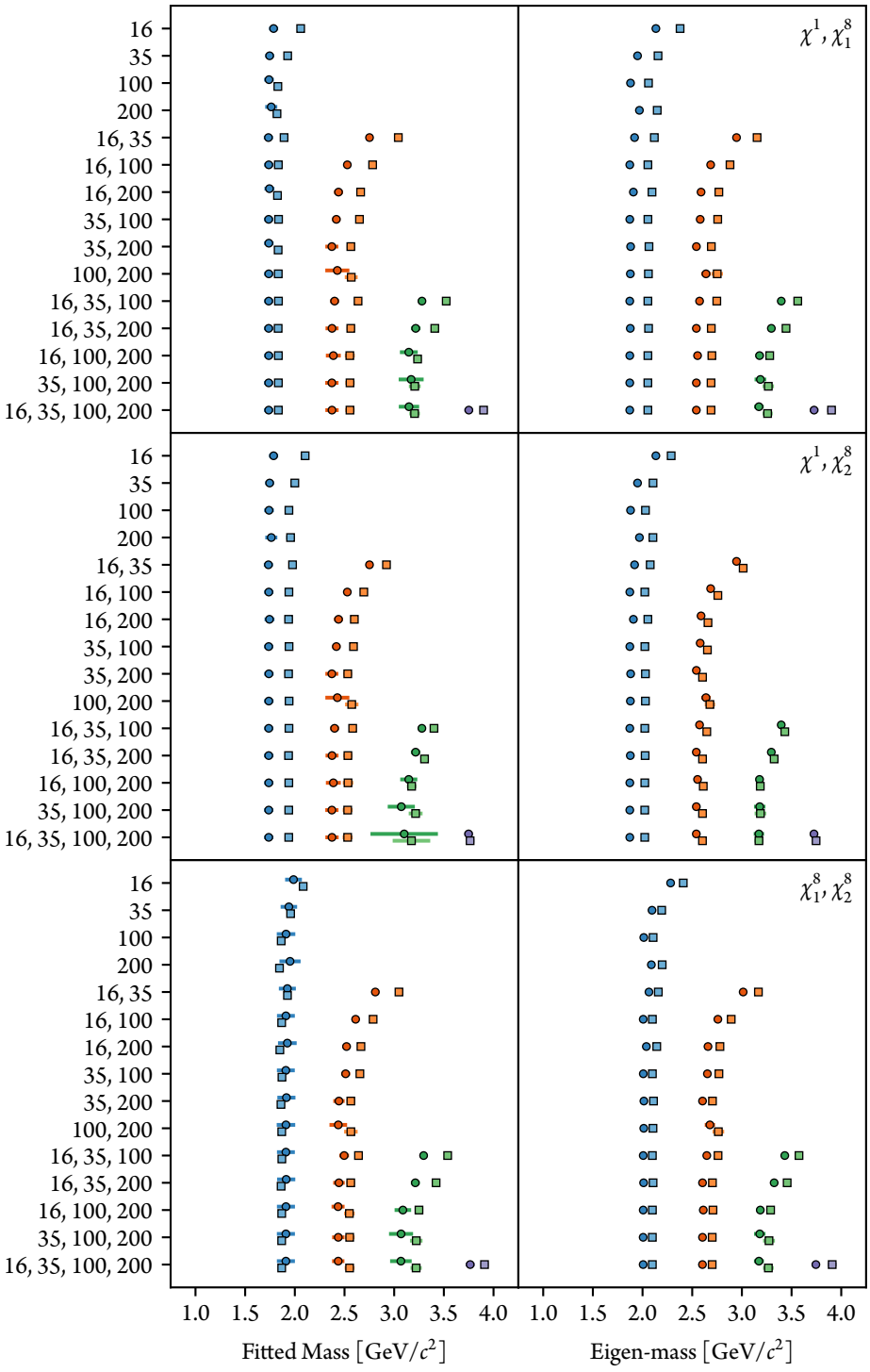
16
35
100
200
16, 35
16, 100
16, 200
35, 100
35, 200
100, 200
16, 35, 100
16, 35, 200
16, 100, 200
35, 100, 200
16, 35, 100, 200
χ^1, χ_1^8
χ^1, χ_2^8
χ_1^8, χ_2^8
1.0 1.5 2.0 2.5 3.0 3.5 4.0
Fitted Mass [GeV/c^2]
Eigen-mass [GeV/c^2]

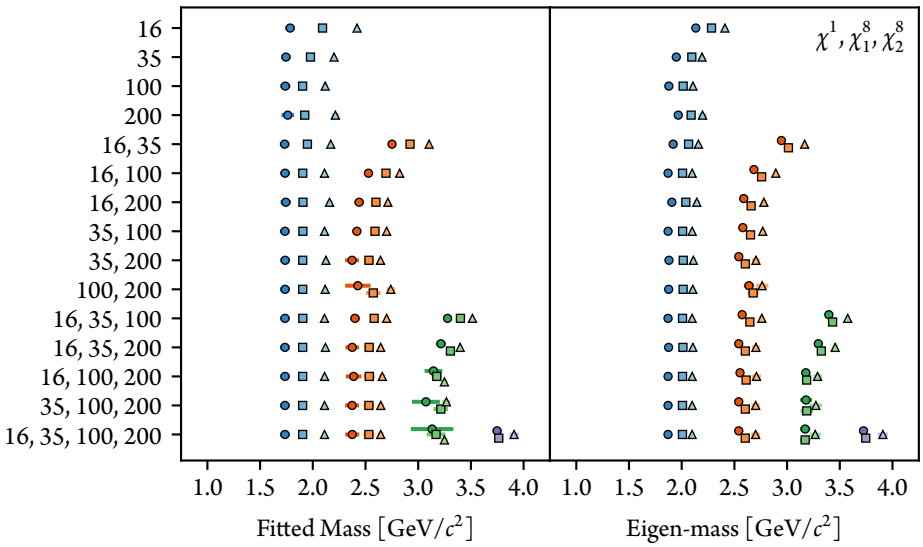

Figure B.16: Comparison of the masses extracted from fitting the projected effective mass (left) and from the eigenvalues (right) on the ensemble with $\kappa_{u,d} = 0.13727$ across all combinations of smearing levels using all three "flavoured" interpolating operators.

Figure B.17: *(facing page)* Comparison of the masses extracted from fitting the projected effective mass (left) and from the eigenvalues (right) on the ensemble with $\kappa_{u,d} = 0.13754$ across all combinations of smearing levels using a single "flavoured" interpolating operator.

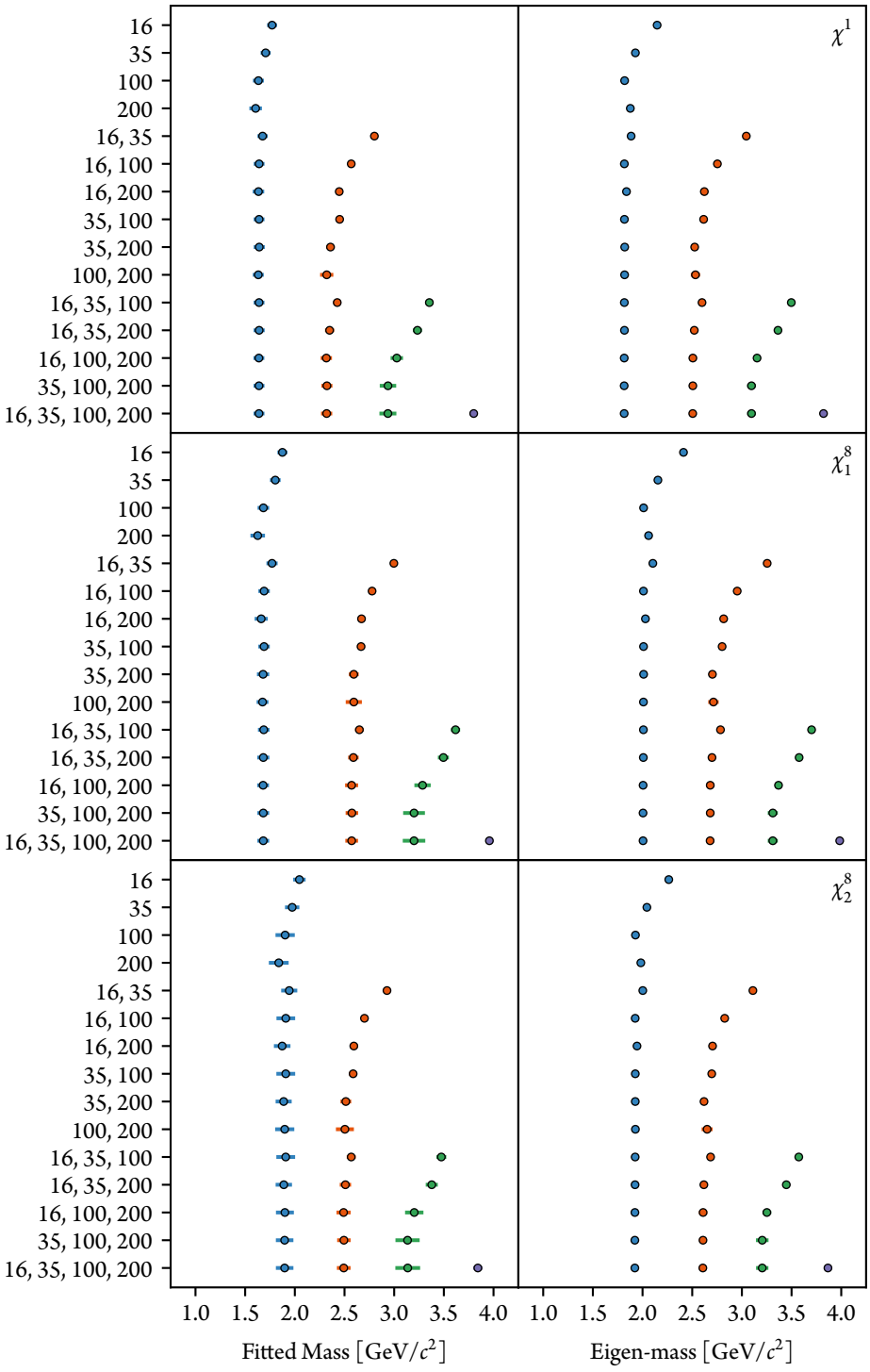
16
35
100
200
16, 35
16, 100
16, 200
35, 100
35, 200
100, 200
16, 35, 100
16, 35, 200
16, 100, 200
35, 100, 200
16, 35, 100, 200
χ^1
χ_1^8
χ_2^8
1.0
1.5
2.0
2.5
3.0
3.5
4.0
Fitted Mass [GeV/c^2]
Eigen-mass [GeV/c^2]

Figure B.18: *(facing page)* Comparison of the masses extracted from fitting the projected effective mass (left) and from the eigenvalues (right) on the ensemble with $\kappa_{u,d} = 0.13754$ across all combinations of smearing levels using two of the three "flavoured" interpolating operators.

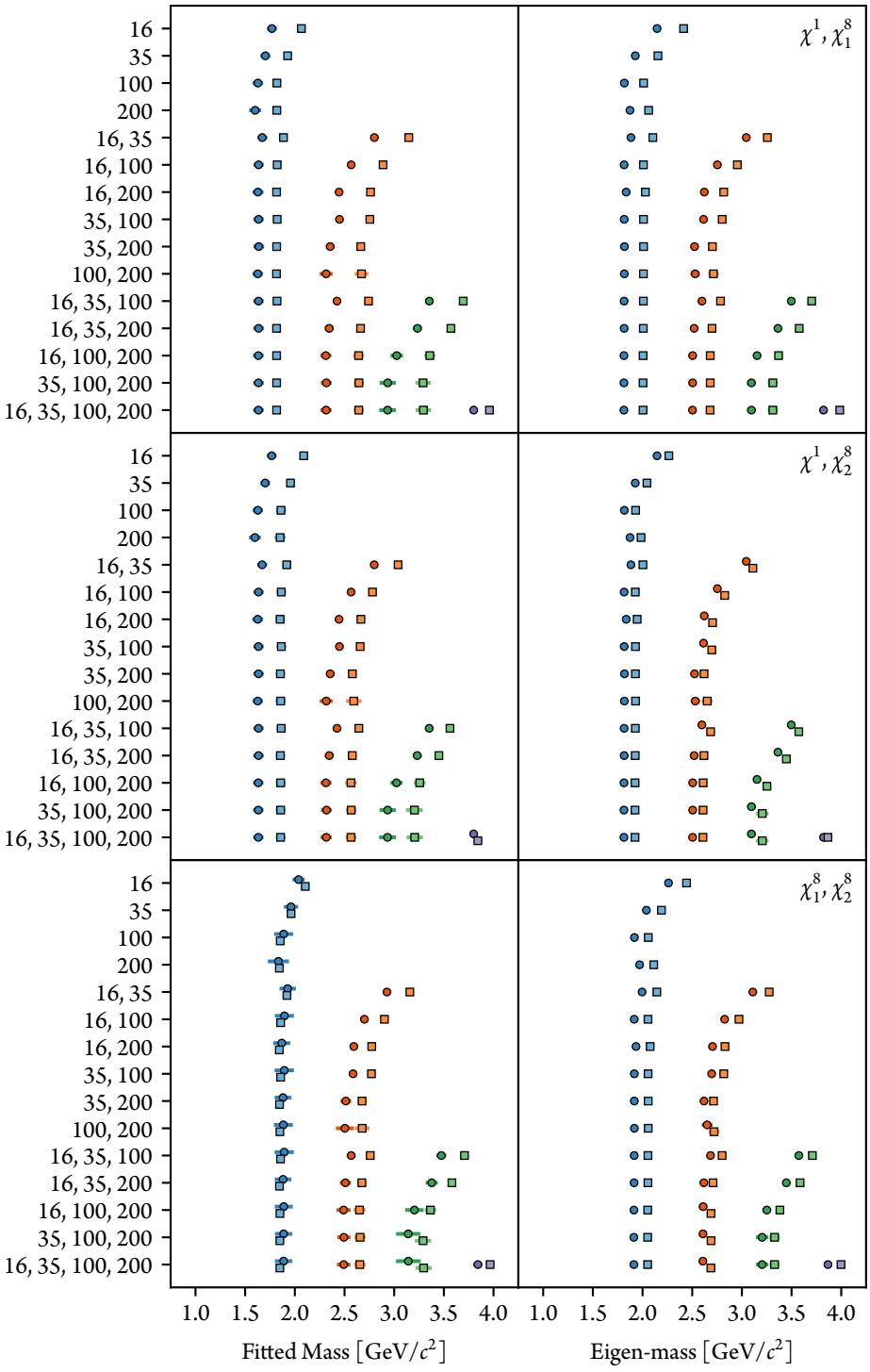
16
35
100
200
16, 35
16, 100
16, 200
35, 100
35, 200
100, 200
16, 35, 100
16, 35, 200
16, 100, 200
35, 100, 200
16, 35, 100, 200
χ^1, χ_1^8
χ^1, χ_2^8
χ_1^8, χ_2^8
1.0 1.5 2.0 2.5 3.0 3.5 4.0
Fitted Mass [GeV/c^2]
Eigen-mass [GeV/c^2]

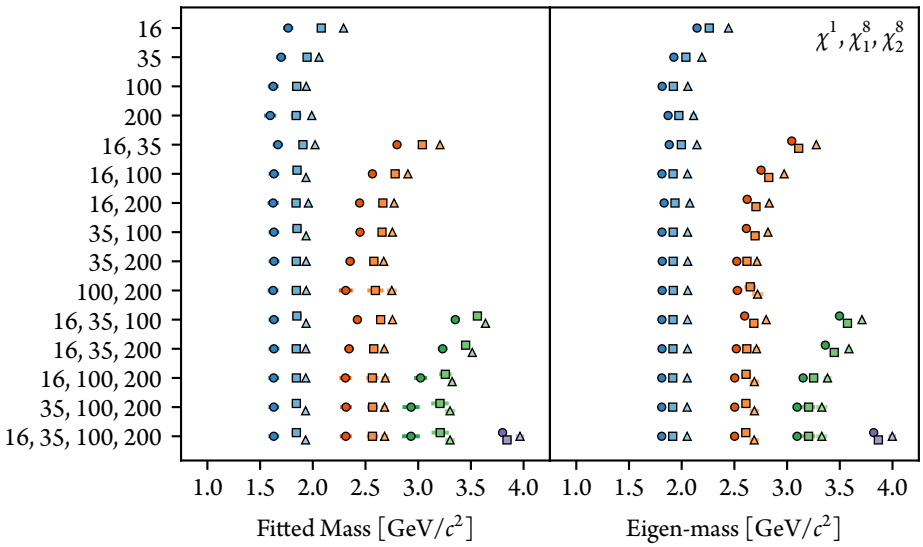

Figure B.19: Comparison of the masses extracted from fitting the projected effective mass (left) and from the eigenvalues (right) on the ensemble with $\kappa_{u,d} = 0.13754$ across all combinations of smearing levels using all three "flavoured" interpolating operators.

Figure B.20: *(facing page)* Comparison of the masses extracted from fitting the projected effective mass (left) and from the eigenvalues (right) on the ensemble with $\kappa_{u,d} = 0.13770$ across all combinations of smearing levels using a single "flavoured" interpolating operator.

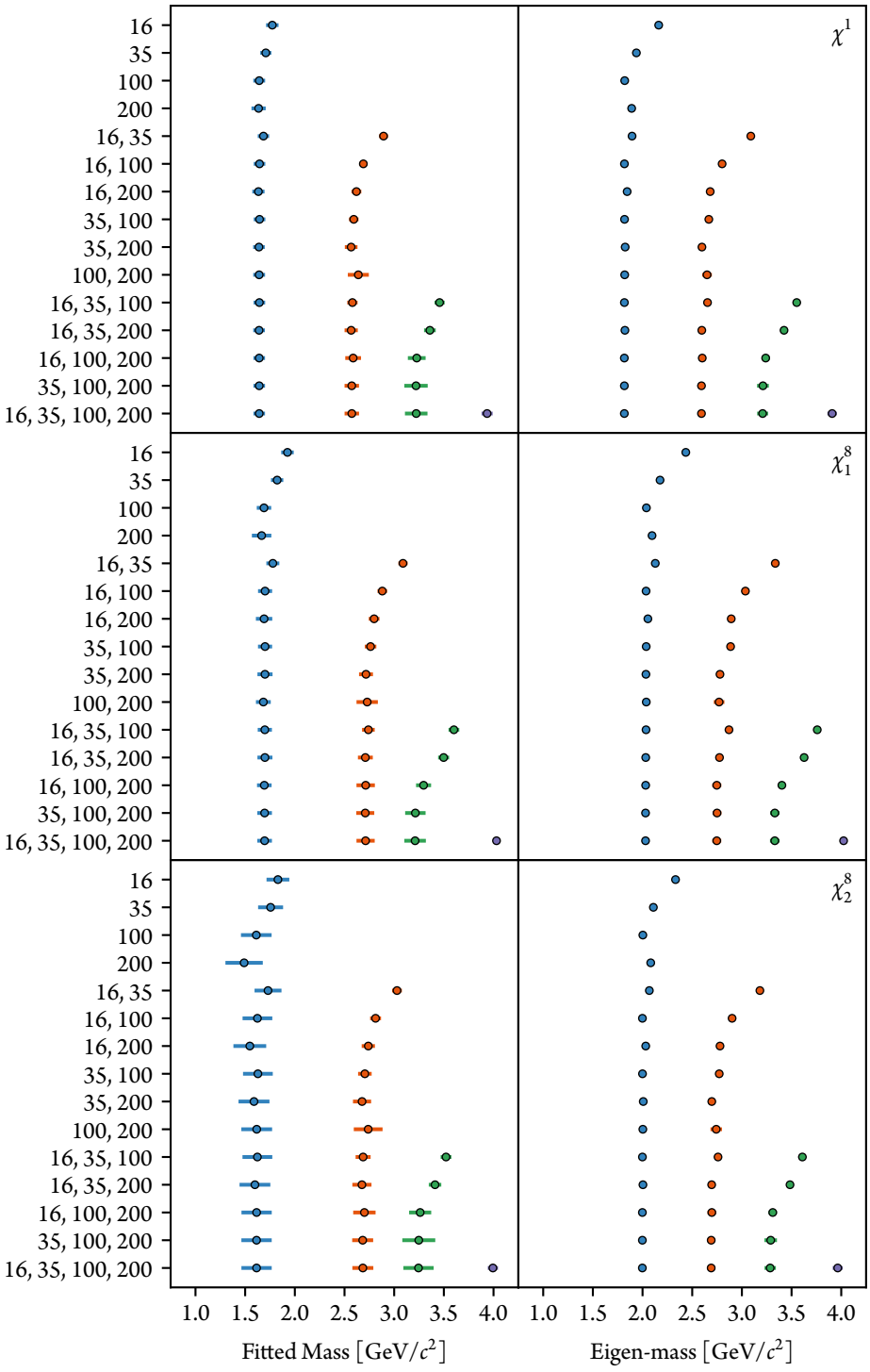
16
35
100
200
16, 35
16, 100
16, 200
35, 100
35, 200
100, 200
16, 35, 100
16, 35, 200
16, 100, 200
35, 100, 200
16, 35, 100, 200
χ^1
χ_1^8
χ_2^8
1.0 1.5 2.0 2.5 3.0 3.5 4.0
Fitted Mass [GeV/c^2]
Eigen-mass [GeV/c^2]

Figure B.21: *(facing page)* Comparison of the masses extracted from fitting the projected effective mass (left) and from the eigenvalues (right) on the ensemble with $\kappa_{u,d} = 0.13770$ across all combinations of smearing levels using two of the three "flavoured" interpolating operators.

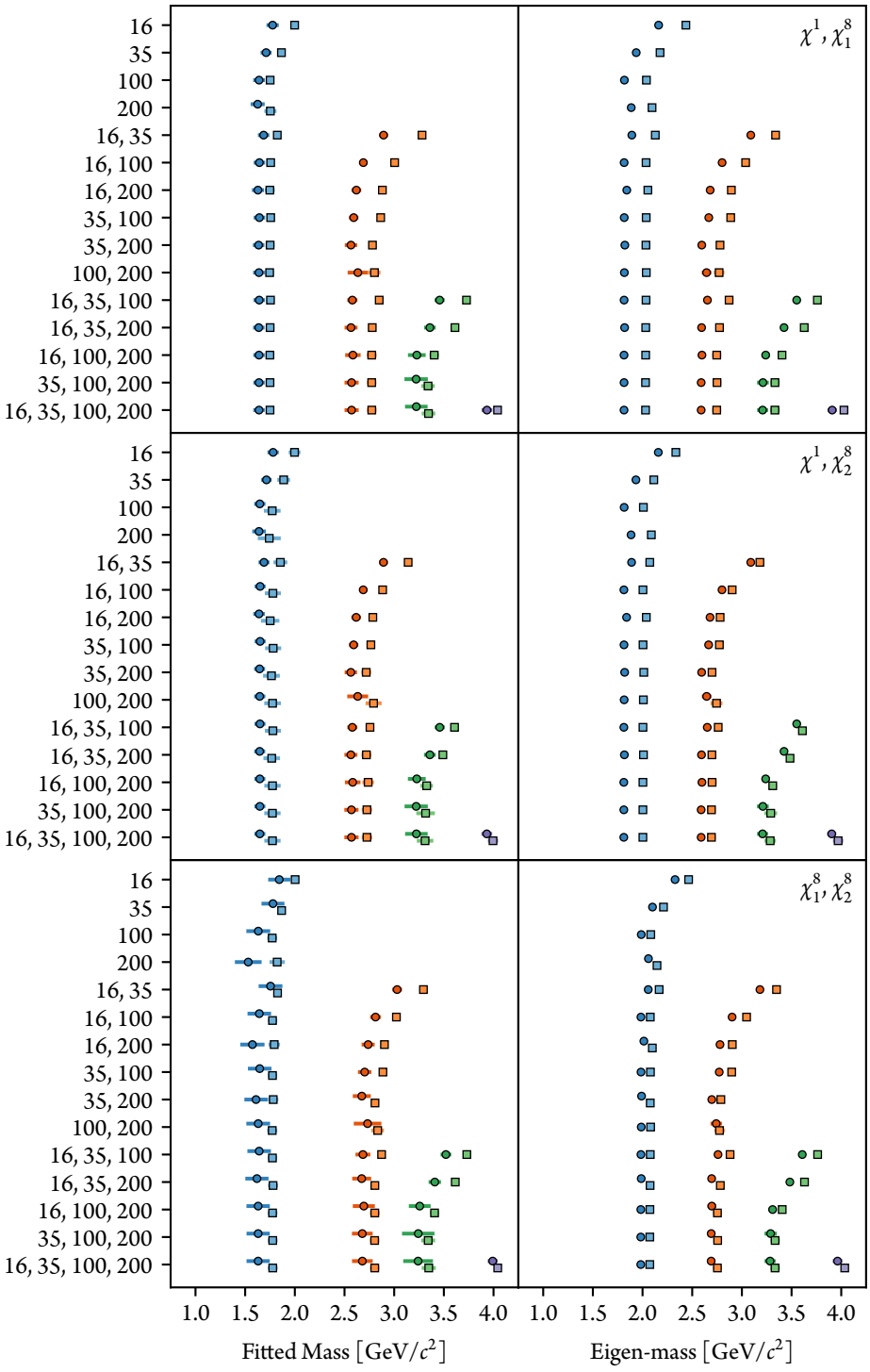
16
35
100
200
16, 35
16, 100
16, 200
35, 100
35, 200
100, 200
16, 35, 100
16, 35, 200
16, 100, 200
35, 100, 200
16, 35, 100, 200
χ^1, χ_1^8
χ^1, χ_2^8
χ_1^8, χ_2^8
1.0 1.5 2.0 2.5 3.0 3.5 4.0
Fitted Mass [GeV/c^2]
Eigen-mass [GeV/c^2]

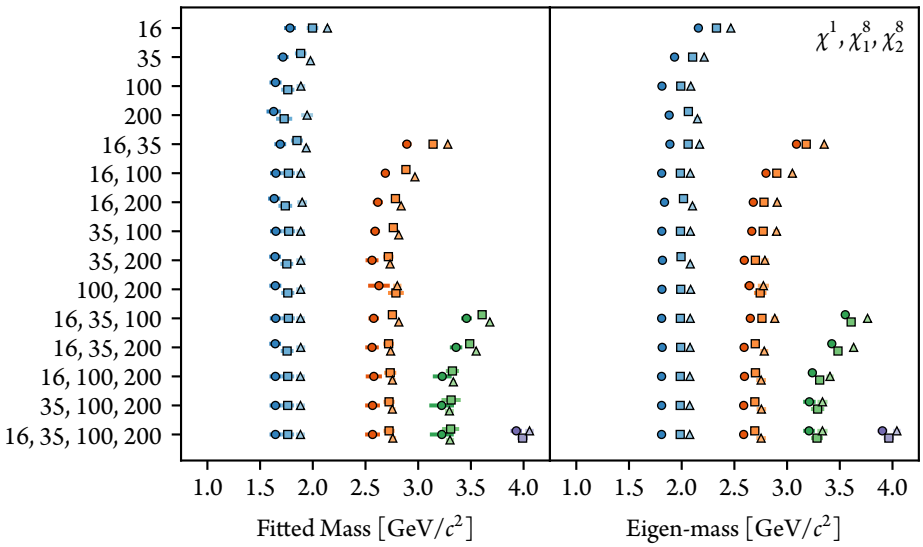

Figure B.22: Comparison of the masses extracted from fitting the projected effective mass (left) and from the eigenvalues (right) on the ensemble with $\kappa_{u,d} = 0.13770$ across all combinations of smearing levels using all three "flavoured" interpolating operators.

Figure B.23: *(facing page)* Comparison of the masses extracted from fitting the projected effective mass (left) and from the eigenvalues (right) on the ensemble with $\kappa_{u,d} = 0.13781$ across all combinations of smearing levels using a single "flavoured" interpolating operator.

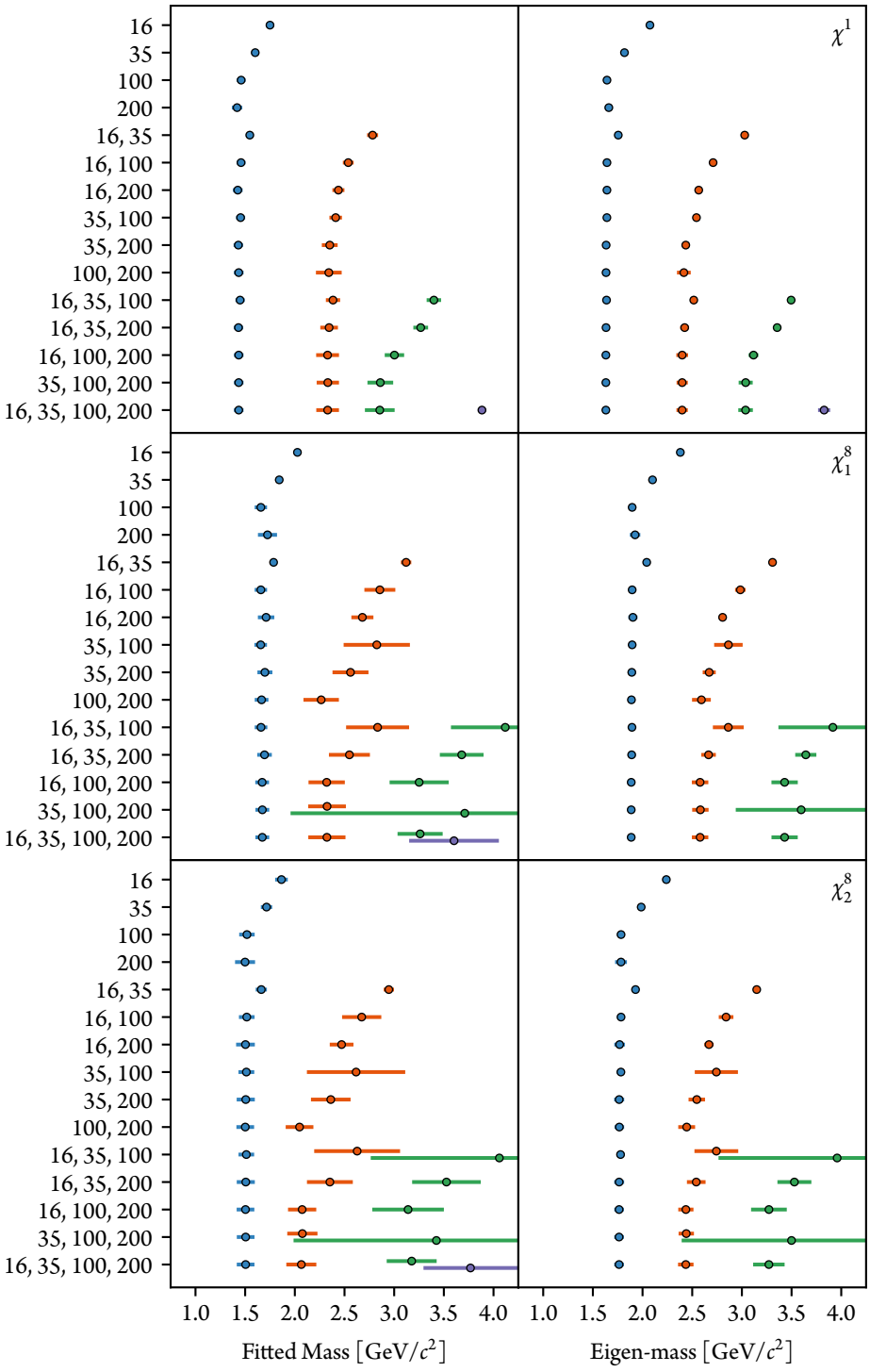
16
35
100
200
16, 35
16, 100
16, 200
35, 100
35, 200
100, 200
16, 35, 100
16, 35, 200
16, 100, 200
35, 100, 200
16, 35, 100, 200
χ^1
χ_1^8
χ_2^8
1.0
1.5
2.0
2.5
3.0
3.5
4.0
Fitted Mass [GeV/c^2]
Eigen-mass [GeV/c^2]

Figure B.24: *(facing page)* Comparison of the masses extracted from fitting the projected effective mass (left) and from the eigenvalues (right) on the ensemble with $\kappa_{u,d} = 0.13781$ across all combinations of smearing levels using two of the three "flavoured" interpolating operators.

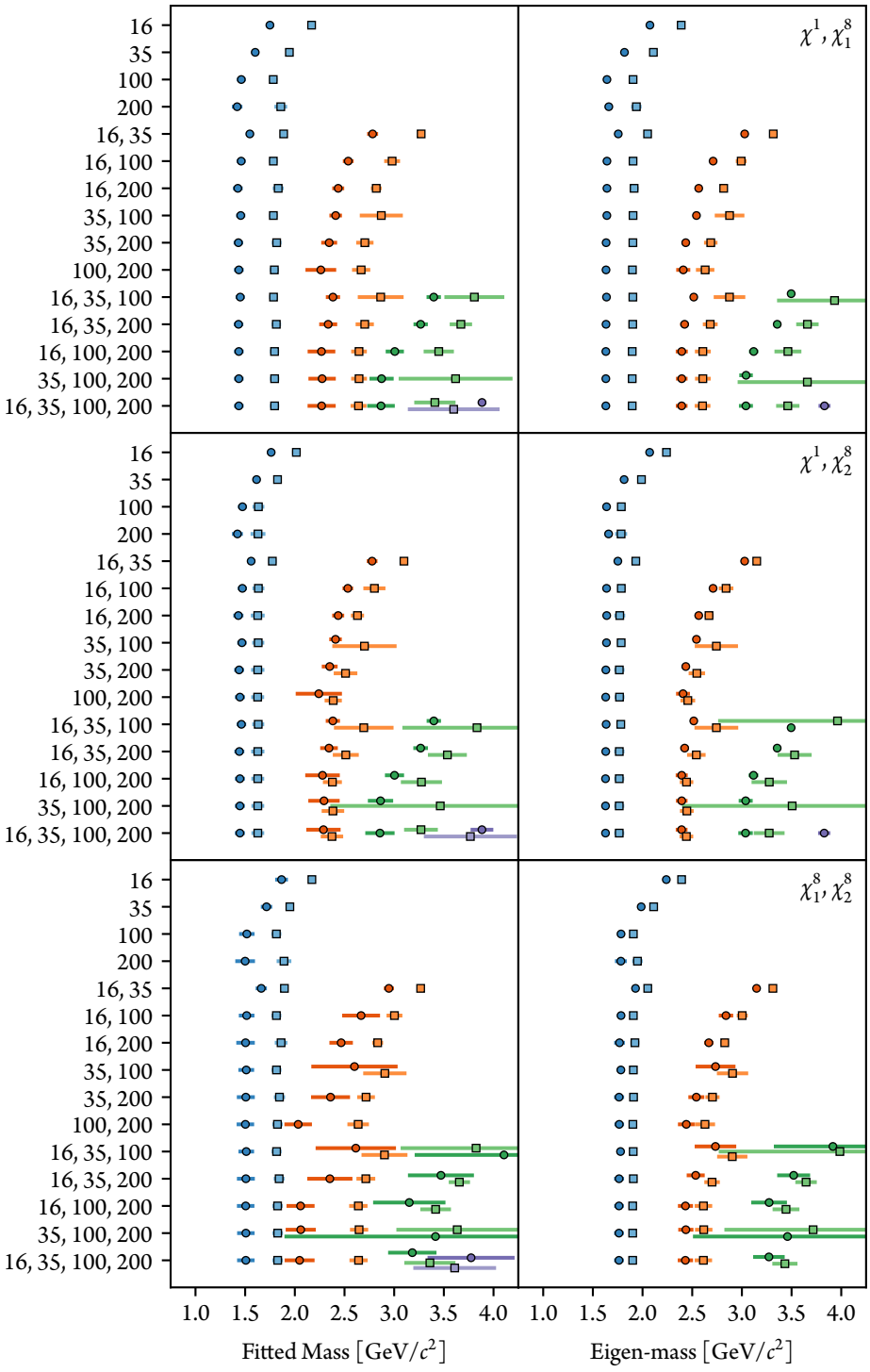
16
35
100
200
16, 35
16, 100
16, 200
35, 100
35, 200
100, 200
16, 35, 100
16, 35, 200
16, 100, 200
35, 100, 200
16, 35, 100, 200
χ^1, χ_1^8
χ^1, χ_2^8
χ_1^8, χ_2^8
1.0
1.5
2.0
2.5
3.0
3.5
4.0
Fitted Mass [GeV/c^2]
Eigen-mass [GeV/c^2]

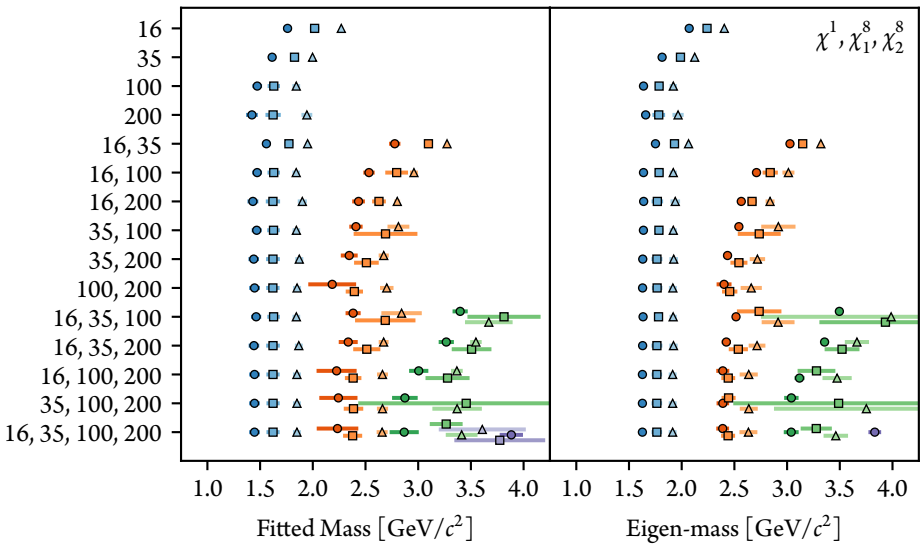

Figure B.25: Comparison of the masses extracted from fitting the projected effective mass (left) and from the eigenvalues (right) on the ensemble with $\kappa_{u,d} = 0.13781$ across all combinations of smearing levels using all three "flavoured" interpolating operators.